

**HIGH DATA RATE ATOM  
INTERFEROMETRIC GRAVIMETRY  
FOR INERTIAL NAVIGATION  
APPLICATIONS**

by

**BENJAMIN CALEB ADAMS**

A thesis submitted to  
The University of Birmingham  
for the degree of  
DOCTOR OF PHILOSOPHY



Quantum Sensing Group  
School of Physics and Astronomy  
College of Engineering and Physical Sciences  
University of Birmingham

September, 2023

UNIVERSITY OF  
BIRMINGHAM

**University of Birmingham Research Archive**

**e-theses repository**

This unpublished thesis/dissertation is copyright of the author and/or third parties. The intellectual property rights of the author or third parties in respect of this work are as defined by The Copyright Designs and Patents Act 1988 or as modified by any successor legislation.

Any use made of information contained in this thesis/dissertation must be in accordance with that legislation and must be properly acknowledged. Further distribution or reproduction in any format is prohibited without the permission of the copyright holder.

## Abstract

This thesis details the development of a high-data rate absolute gravimeter targeting future applications in inertial navigation. The technology is underpinned by performing atom interferometry with stimulated Raman transitions with laser-cooled  $^{87}\text{Rb}$ . A key highlight of this work is validating an optical single sideband laser system based on fibre-Bragg grating filters which offers a promising pathway toward portable quantum sensing. Another highlight is validating a simple MOT dynamics model in the relatively unexplored high-data rate operation mode. Typically, the system operates with 30 Hz bandwidth by launching  $1 \times 10^8$  atoms at  $0.25 \text{ ms}^{-1}$  downwards at a temperature of  $20 \text{ }\mu\text{K}$ . Atom interferometry is performed with a T time of 2.5 ms giving a preliminary accuracy of  $10 \text{ }\mu\text{g}$  and a sensitivity of  $20 \frac{\mu\text{g}}{\sqrt{\text{Hz}}}$ .

## Acknowledgements

I sincerely thank my supervisors, Prof. Kai Bongs and Dr. Yu-Hung Lien, for their expertise and support during my PhD. Specific thanks should go to Yu-Hung for his day-to-day practical supervision and to Kai for his vision and leadership. I would like to acknowledge Dr. Archie Kubba for help designing the optomechanical structure and Dr. Calum Macrae for his work developing the first iteration of the Raman laser. Additionally, thanks to David Sedlak, Sam Hedges, Jonathan Winch, Ben Stray, Adam Seedat, Jamie Vovrosh, Luuk Earl, Medhi Langlois, Farzad Hayati, Sanaz Roshanmanesh, Rustin Nourshargh, Oliver Ennis, Kevin Ridley, Carlos Alberto Niño Sandoval, Yuanlei He, Matthew Forward, Liam Bussey, Soumyodeep Dey, Andrew Hinton, Kevin Ridley, Geoffrey de Villiers, Andrew Lamb, Michael Holynski, and Teresa Palubicki for making my study enjoyable. Further thanks to Lawrence Till (Nemein) and the university workshop team for their excellent manufacturing work for this project. I also appreciate the collaborations with DSTL and Toyota Motor Europe. Lastly, I acknowledge the unwavering support of my family (Luke, Elaine and Abigail) and faith, which motivate me daily.



# Contents

<b>1</b>	<b>Motivation</b>	<b>17</b>
1.1	Gravimetry . . . . .	18
1.2	Relative Gravimeters . . . . .	21
1.3	Absolute Gravimeters . . . . .	23
1.4	Absolute Quantum Gravimeter . . . . .	24
1.4.1	State of the art . . . . .	28
1.5	Data Rate and Bandwidth . . . . .	29
1.6	Quantum Navigation . . . . .	31
1.7	Thesis Structure . . . . .	33
<b>2</b>	<b>Raman Atom Interferometry</b>	<b>35</b>
2.1	Stimulated Raman Transitions . . . . .	36
2.1.1	Three level atom in a light field . . . . .	39
2.2	Rabi Oscillations . . . . .	43
2.3	Raman Configuration . . . . .	46
2.4	Velocity Selection . . . . .	47

2.5	Inhomogeneities . . . . .	50
2.6	Light Shift . . . . .	52
2.7	Atom Interferometry . . . . .	55
2.7.1	Laser Phase . . . . .	57
2.8	Interferometer Phase . . . . .	59
2.9	Phase Noise . . . . .	60
2.9.1	Raman Laser Phase Noise . . . . .	61
2.9.2	Vibrational Noise . . . . .	64
<b>3</b>	<b>Laser Cooling and Trapping</b>	<b>67</b>
3.1	Laser Cooling . . . . .	67
3.2	Trapping . . . . .	70
3.3	Capture Velocity . . . . .	73
3.3.1	Trap Diameter . . . . .	76
3.3.2	Finite Power . . . . .	77
3.4	High Bandwidth Operation . . . . .	79
3.4.1	Intensity Dependence . . . . .	79
3.4.2	Pressure Dependence . . . . .	82
3.4.3	MOT Loading . . . . .	83
3.4.4	Cloud Expansion . . . . .	88
<b>4</b>	<b>High Bandwidth Atom Interferometry</b>	<b>90</b>
4.1	Zeeman Shift . . . . .	91

4.2	Raman Degeneracy . . . . .	91
4.3	Moving Molasses . . . . .	95
4.3.1	Launch Time . . . . .	98
4.3.2	Launch Direction . . . . .	100
4.4	Temperature . . . . .	103
4.5	Raman Optimisation . . . . .	108
4.6	Sensitivity . . . . .	112
4.7	Modelling Summary . . . . .	113
<b>5</b>	<b>Experimental Setup</b>	<b>115</b>
5.1	Apparatus . . . . .	115
5.1.1	Coil Design . . . . .	117
5.1.2	Control System . . . . .	121
5.2	Optics Delivery . . . . .	123
5.3	Static Operation . . . . .	127
5.4	Dynamic Operation . . . . .	130
5.5	Launching . . . . .	138
5.6	Temperature . . . . .	139
5.6.1	Velocimetry . . . . .	141
5.6.2	Piecewise Ramps . . . . .	142
5.6.3	Outlook . . . . .	146
5.7	Experimental Sequence . . . . .	149

<b>6</b>	<b>Raman Laser System</b>	<b>151</b>
6.1	Overview . . . . .	152
6.2	RF Generation . . . . .	155
6.3	Spectral Purity . . . . .	156
6.4	Power Performance . . . . .	161
6.5	Further Testing . . . . .	163
<b>7</b>	<b>Results</b>	<b>166</b>
7.1	State Initialisation . . . . .	166
7.2	Co-Propagating Configuration . . . . .	168
7.3	Counter-Propagating Configuration . . . . .	171
7.3.1	Breaking Raman Degeneracy . . . . .	173
7.3.2	Rabi Oscillations . . . . .	174
7.4	Interferometry . . . . .	177
7.5	Noise . . . . .	183
7.5.1	Atom Shot Noise . . . . .	184
7.5.2	Photon Shot Noise . . . . .	184
7.5.3	MOT Fluctuations . . . . .	185
7.5.4	Raman Laser Intensity Noise . . . . .	186
7.5.5	Raman Laser Polarisation . . . . .	187
7.5.6	Vibration . . . . .	187
7.6	Systematic Issues . . . . .	188

7.6.1	Magnetic Field . . . . .	189
7.6.2	Two-photon Light Shift . . . . .	190
7.6.3	Laser Alignment . . . . .	191
7.6.4	Coriolis Effect . . . . .	192
7.7	Environmental Effects . . . . .	193
7.8	Summary . . . . .	195
<b>8</b>	<b>Conclusion</b>	<b>197</b>
<b>A</b>	<b>Rubidium-87 Data</b>	<b>201</b>

## Abbreviations

**AOM** acousto-optic modulator

**CMOS** complementary metal oxide semiconductor

**DDS** direct digital synthesizer

**EDFA** erbium-doped fibre amplifier

**EOM** electro-optic modulator

**FBG** fibre-bragg grating

**MOT** magneto-optical trap

**MTS** modulation transfer spectroscopy

**PBS** polarising beam splitter

**SHG** second-harmonic generation

# List of Figures

1.1	Optical and atom interferometer comparison . . . . .	26
1.2	Single shot high bandwidth comparison . . . . .	31
1.3	Gravity map-matching illustration . . . . .	33
2.1	Stimulated Raman transitions . . . . .	36
2.2	Rabi oscillations illustration . . . . .	45
2.3	Velocity selection illustration . . . . .	49
2.4	Inhomogeneous Rabi flopping . . . . .	52
2.5	Energy level scheme of the $^{87}\text{Rb}$ $D_2$ line . . . . .	54
2.6	Raman laser intensity ratio . . . . .	55
2.7	Space-time diagram for $\frac{\pi}{2} - \pi - \frac{\pi}{2}$ interferometry sequence. . .	56
2.8	Sensitivity function . . . . .	62
2.9	Double logarithmic plot of $ \text{H}(\omega) ^2$ . . . . .	64
2.10	Double logarithmic plot of $\frac{ \text{H}_a(2\pi f) }{k_{\text{eff}}gT^2}$ . . . . .	66
3.1	1D Laser Cooling . . . . .	68

3.2	Underlying trapping mechanism of a MOT . . . . .	71
3.3	Numerical simulation of atomic trajectories . . . . .	72
3.4	Capture velocity demonstration . . . . .	74
3.5	Capture velocity dependence on laser detuning and intensity .	75
3.6	Capture velocity dependence on simulation time . . . . .	75
3.7	Capture velocity against beam diameter . . . . .	76
3.8	Finite power optimisation . . . . .	78
3.9	Beam radius optimisation . . . . .	78
3.10	Single atom trajectories at 100 Hz operation . . . . .	80
3.11	Simulating cloud dynamics . . . . .	82
3.12	Collision model . . . . .	83
3.13	Experimental MOT loading data . . . . .	85
3.14	Traditional vs dynamic MOT loading simulation . . . . .	88
3.15	3D dynamics simulation at 100 Hz . . . . .	89
3.16	3D dynamics simulation at 10 Hz . . . . .	89
4.1	Zeeman splitting of the $m_f$ states in the low field regime. . . . .	91
4.2	Modelling counter-propagating Raman spectroscopy . . . . .	93
4.3	Modelling counter-propagating Raman transitions for variable velocity . . . . .	93
4.4	Optimising Raman degeneracy for variable pulse length . . . . .	94
4.5	Launch direction effect on Raman degeneracy . . . . .	95



4.6	Maximum downward velocity simulation . . . . .	96
4.7	2D moving molasses Geometry. . . . .	97
4.8	Simulating 2D moving molasses in XY plane . . . . .	98
4.9	Velocity over time during 2D moving molasses . . . . .	99
4.10	Time to establish stable 2D moving molasses . . . . .	99
4.11	Angular launch bias single trajectories . . . . .	101
4.12	Angular launch bias variable misalignment . . . . .	101
4.13	Angular deviation due to power noise . . . . .	103
4.14	Sub-Doppler force profile . . . . .	105
4.15	Force ratio of sub-Doppler cooling model to linear approximation	105
4.16	Slowing an atom with sub-Doppler cooling force . . . . .	106
4.17	Theoretical equilibrium temperature . . . . .	108
4.18	Peak population transfer against temperature . . . . .	109
4.19	Peak population transfer variable pulse length and cloud size .	109
4.20	Optimising beam radius to maximise population transfer . . . .	111
4.21	Raman beam optimisation for variable total power . . . . .	112
5.1	CAD diagram of final assembly . . . . .	116
5.2	Magnetic field gradient profiles for variable coil separation. . .	119
5.3	Optimising magnetic field gradient uniformity. . . . .	119
5.4	Simulating trapping coil field profile . . . . .	120
5.5	PulseBlasterUSB control features. . . . .	122

5.6	Coil driver response . . . . .	122
5.7	Tapered amplifier performance . . . . .	125
5.8	Free space optics schematic diagram . . . . .	126
5.9	$^{87}\text{Rb}$ $D_2$ transition hyperfine structure . . . . .	127
5.10	Atom number for variable cooling power. . . . .	128
5.11	Effect of field gradient on atom number . . . . .	129
5.12	Effect of variable detuning and power on MOT . . . . .	130
5.13	Validating collision model . . . . .	132
5.14	High bandwidth dynamics experiment and theory . . . . .	133
5.15	Simulating steady state atom number for variable drop time . .	134
5.16	Time to load $10^8$ atoms experiment and theory . . . . .	135
5.17	Optimising sensitivity at 100 Hz . . . . .	136
5.18	Sensitivity projection for variable bandwidth . . . . .	138
5.19	Fluorescence imaging of the MOT . . . . .	140
5.20	Thermal expansion of a cloud with 2 ms of sub-Doppler cooling	140
5.21	Illustration of Raman velocimetry method . . . . .	142
5.22	Magnetic field optimisation . . . . .	143
5.23	Multi-stage sub-Doppler cooling optimisation . . . . .	144
5.24	Reconstructing power and detuning ramps . . . . .	145
5.25	Temperature evolution in multi-stage cooling . . . . .	146
5.26	AOM Characterisation. . . . .	147
5.27	Experimental sequence . . . . .	150

6.1	Fibre Bragg grating illustration . . . . .	153
6.2	Raman laser system design . . . . .	154
6.3	FBG Characterisation . . . . .	155
6.4	RF circuit for driving EOM . . . . .	156
6.5	Optical spectrum generated without filtering mixer output . . .	157
6.6	Final RF spectrum . . . . .	158
6.7	Fabre-Perot interferometer spectrums at 780nm . . . . .	159
6.8	Single-tone modulation with EOM . . . . .	160
6.9	Intermodulation products . . . . .	161
6.10	SHG Efficiency . . . . .	162
6.11	Amplitude extinction ratio . . . . .	163
6.12	Adding narrowband FBG . . . . .	164
6.13	Narrowband FBG post EDFA . . . . .	165
7.1	Depumping . . . . .	167
7.2	Co-Propagating Raman Spectroscopy (poor compensation) . .	169
7.3	Co-propagating Raman spectroscopy with a 3 $\mu$ s pulse . . . . .	170
7.4	Co-Propagating Rabi Oscillation Bias alignment . . . . .	171
7.5	Counter-propagating Raman spectroscopy scan over all three m <sub>f</sub> states . . . . .	172
7.6	Counter-propagating Raman spectroscopy for variable pulse length . . . . .	173

7.7	Counter-propagating Raman spectroscopy for variable launch velocities . . . . .	174
7.8	Raman resonance offset for variable launch speed . . . . .	174
7.9	Counter-propagating Rabi oscillations for variable total Raman power. . . . .	175
7.10	Experimental vs theoretical Rabi frequency comparison . . . .	176
7.11	Relative population transfer modelled for different cloud temperatures with comparison to experimental data. . . . .	177
7.12	Interference fringes variable T time . . . . .	178
7.13	Effect of vibration isolation . . . . .	179
7.14	Averaging multiple fringes . . . . .	181
7.15	Averaging down sensitivity . . . . .	182
7.16	Interferometer contrast . . . . .	183
7.17	MOT fluctuations . . . . .	185
7.18	Magnetic field systematic effect . . . . .	190
8.1	Single atom in freefall for variable initial velocity . . . . .	199
8.2	Simulating cloud dynamics for variable launch velocity . . . .	199
A.1	Two-photon $\sigma^+$ - $\sigma^+$ transition . . . . .	202
A.2	Two-photon $\sigma^-$ - $\sigma^-$ transition . . . . .	203
A.3	Two-photon $\pi$ - $\pi$ transition . . . . .	204

# List of Tables

1.1	Gravity signal sizes . . . . .	20
1.2	Parameters commonly used in the gravity measurement . . . . .	20
1.3	Comparison of relative gravimeters with reported specifications.	22
1.4	State-of-the-art absolute gravimeters . . . . .	27
2.1	Properties of the stimulated Raman transitions . . . . .	47
2.2	Phase shifts due to atom-light interaction . . . . .	58
4.1	Design specifications for 100 Hz operation . . . . .	114
5.1	Design specifications for anti-Helmholtz trapping coils. . . . .	121
7.1	Environmental Effects . . . . .	193
7.2	Systematic Noise Budget. . . . .	196
7.3	Systematic Error Budget. . . . .	196
A.1	Properties of $^{87}\text{Rb}$ isotope and its D <sub>2</sub> -line transition . . . . .	201

# Chapter 1

## Motivation

Many integral technologies to modern life have their origins in research institutions. While the journey from proof of principle to practical application can be challenging, numerous technologies have successfully made this transition. Recently, cold atom physics has made significant strides in this direction with the capability to measure accelerations, rotations and time with unprecedented precision [1–9]. This work describes the development of a quantum gravimeter, a device designed to measure gravitational acceleration and focuses on two key challenges for the implementation in dynamic environments [10]. Firstly, it aims to increase the measurement bandwidth to enable faster data acquisition before describing the construction of a laser system targeting field applications.

To provide a contextual background, this chapter begins by exploring gravimetry before discussing gravimeters, their current applications and the state-of-

the-art in the field. Subsequently, the cold atom gravimeter and its fundamental principles are introduced. Finally, the motivation for navigation applications is discussed, followed by an overview of this thesis.

## 1.1 Gravimetry

Gravimetry is a research area concerned with measuring gravitational acceleration and its gradient. The history of the field can be roughly traced to 350 BC when Aristotle believed the speed of a falling object should increase with weight which was later proved false. According to legend, in the 16<sup>th</sup> century Galileo performed an experiment dropping two balls of identical volume but differing mass off the Leaning Tower of Pisa to show that they fell at the same rate. Galileo's study of falling objects and the subsequent work of Newton arrived at the universal law of gravitation and a much clearer understanding of the force given by equation 1.1 [11].

$$\mathbf{F} = \frac{GmM}{r^2}\hat{\mathbf{r}}. \quad (1.1)$$

The force depends on the masses of the two objects  $m$  and  $M$ , inversely scaled by the square of their separation,  $r$ . To calculate the strength of the gravitational field from a mass  $M$ , the substitution  $F = mg$  is made. From this equation 1.2 is obtained where mass  $M$  is expressed as a spatially varying density  $\rho$ , integrated over a volume  $V$ . The gravitational strength  $g$ , at a

certain point is the magnitude of the infinite sum of all mass contributions, scaled by the square of their relative distances.

$$g = |\mathbf{g}| = \left| \frac{GM}{r^2} \hat{\mathbf{r}} \right| = \left| G \int \frac{\rho \cdot \hat{\mathbf{r}}}{r^2} dV \right|. \quad (1.2)$$

Before continuing a distinction between gravitation and gravity should be made as often these terms are used interchangeably. Gravitation refers to universal law describing the force of attraction between two bodies. Of the four fundamental forces gravitation is by far the weakest. However, for a sufficiently large mass like Earth the force between an object and Earth is significant and is called gravity. Gravity varies across the Earth. The Earth's oblate spheroid shape constitutes the largest positional change, with  $g$  changing with latitude, from  $9.78 \text{ ms}^{-2}$  at the equator to  $9.83 \text{ ms}^{-2}$  at the poles [12]. Note this variation also includes the effect of the fictitious centrifugal force due to the Earth's rotation about its own axis. This force is often not explicitly included in gravitational measurements but contributes to variations in gravity across the Earth being strongest at the equator and weakest at the poles. Table 1.1 details typical signals generated by different features. While gravity is a relatively weak force, it varies significantly over different scales and cannot be attenuated, this means with sufficiently sensitive devices gravity variations are always measurable. However, measurements are problematic as the equivalence principle means gravitational accelerations are



indistinguishable from other inertial forces meaning vibrations appear equivalent to a gravitational field. The International System of Units (SI) measures gravity in  $\text{N/kg}$  or  $\text{m/s}^2$  whereas in geophysics the Gal from the Centimetre-Gram-Seconds (CGS) unit system is adopted. 1 Gal, named in honour of Galilei, is a large quantity compared with gravity variations on Earth and so mGal and  $\mu\text{Gal}$  quantities are widely quoted. Table 1.2 compares equivalent CGS and SI units, in this work gravity is specified in  $\mu\text{Gal}$ , mGal or  $\mu\text{g}$ .

Table 1.1: Approximate magnitudes of changes in gravitational acceleration at the earth's surface from various sources, data from [13, 14].

Sources	Relative Magnitude (g)
Earth	1
Latitudinal variation	$5 \times 10^{-3}$
Mountain ranges/ocean trenches	$2 \times 10^{-4}$
Mineral anomalies	$1 \times 10^{-6}$
Elevation by 1 m	$3 \times 10^{-7}$
Solid earth tides	$3 \times 10^{-7}$
Volcanic/seismic activity	$2 \times 10^{-7}$
Sun/Moon tides	$1 \times 10^{-7}$
Mining/large constructions	$1 \times 10^{-7}$
Ocean tide loading	$1 \times 10^{-8}$
Ground water variations	$1 \times 10^{-8}$
Postglacial rebound	$1 \times 10^{-8}$
Polar motion	$8 \times 10^{-9}$
Glaciers/polar ice changes	$5 \times 10^{-9}$
Person at 1 m distance	$5 \times 10^{-10}$

Table 1.2: Parameters commonly used in the gravity measurement in equivalent CGS and SI unit systems.

Parameters	CGS	SI
Force of Attraction	$1 \times 10^5$ dynes	$1 \text{ kg ms}^{-2}$ or newton (N)
Gravitational Acceleration	1 Gal	$1 \times 10^{-2} \text{ ms}^{-2}$
	1 mGal	$1 \times 10^{-5} \text{ ms}^{-2}$
	1 $\mu\text{Gal}$	$1 \times 10^{-8} \text{ ms}^{-2}$

## 1.2 Relative Gravimeters

Gravimeters are typically categorised as absolute or relative. Relative devices only measure changes in gravity whereas absolute devices also provide accurate values for it. Consequently, the scaling for a relative device requires calibration with an absolute gravimeter. Accuracy denotes how close the measured value is to true gravitational acceleration, while precision describes the scatter associated with repeated measurements. For relative instruments how close the instrument gets to the true gravity value along with drift and stability are of primary concern. The Scintrex CG-6 represents the current state-of-the-art in portable gravimetry delivering  $50 \text{ nm s}^{-2}$  accuracy in a 10 L, 5 kg package. Table 1.3 showcases the performance of various relative gravimeters. The Scintrex is portable with good accuracy. Superconducting sphere gravimeters are very accurate and precise but have limited field utility requiring specialist cooling liquids, days of setup and high power requirements. In contrast, microelectromechanical systems or MEMS gravimeters are less accurate but do offer significantly faster measurement rates in a much more compact, low cost package. However, MEMS devices incur significant drifts which naturally is a major issue for applications.

Table 1.3: Comparison of relative gravimeters with reported specifications.

<b>Model</b> Manufacturer	<b>CG - 6</b> Scintrex	<b>Chekan Shelf</b> CSRI Elektropribor	<b>iGrav</b> GWR Instruments	<b>MEMS gravimeter</b> University of Glasgow
Principle	Fused Quartz Spring	Torsion Quartz Fibres	Superconducting Spheres	MEMS flexure spring
Sensitivity	$50 \text{ nms}^{-2}$	$700 \text{ nms}^{-2}$	$0.01 \text{ nms}^{-2}$	$100 \text{ nms}^{-2}$
Noise	-	-	$0.01 \text{ nms}^{-2}$	$400 \text{ nms}^{-2}$
Measurement rate	10 Hz	50 Hz	1 Hz	0.03 Hz
Drift	$200 \text{ nms}^{-2} / \text{day}$	$5.6 \mu\text{ms}^{-2} / \text{day}$	$0.06 \mu\text{ms}^{-2} / \text{day}$	$1.5 \mu\text{ms}^{-2} / \text{day}$
Volume	10 L	77 L	104 L	0.2 L*
Power	10 W	300 W	1.3kW	
Mass	5 kg	78 kg	37 kg	
Reference	[15, 16]	[17, 18]	[19, 20]	[21]

### 1.3 Absolute Gravimeters

Absolute gravimeters directly measure gravitational acceleration in units of meters per second squared ( $\text{ms}^{-2}$ ). While a pendulum can be used to construct an absolute gravimeter greater precision is achieved by timing freely falling objects. A widely used device based on this principle is called a corner cube reflector. This measures gravity by reflecting light off a free-falling mirror and making a comparison against a stationary one. These mirrors form the arms of an optical interferometer, the interference between the lasers is then linked to the differential acceleration of the mirrors from which gravity is extracted. The Micro-g LaCoste FG5 and the upgraded FG5-X are two commercially available absolute gravimeters of this type. These instruments are accurate to within  $31 \text{ nm s}^{-2}$  but have slow measurement rates ( $\sim 0.1 \text{ Hz}$ ) limited by the damping time of mechanical vibrations generated by the corner cube after each fall. Naturally, this low bandwidth limits mobile applications. Furthermore, these devices already operate close to their noise floor meaning large improvements are unlikely.

Comparing absolute and relative gravimeters the readings from relative gravimeters show notable instrumental drift and jumps when the instrument is moved. This means that relative devices require calibration while absolute ones are less prone to this. Therefore, an absolute gravimeter is desirable when it is hard to distinguish gravimetric data from these effects. However, relative

gravimeters can reach higher sensitivities in a more compact form factor. Recently, quantum absolute gravimeters have surpassed the performance of corner-cube absolute gravimeters. These devices use laser-cooled atoms to measure gravity rather than macroscopic masses. Quantum absolute gravimetry not only offers potential for improved compactness but measurement rates comparable to relative gravimeters. Moreover, these instruments have no moving mechanical parts, making them promising candidates for field applications.

## 1.4 Absolute Quantum Gravimeter

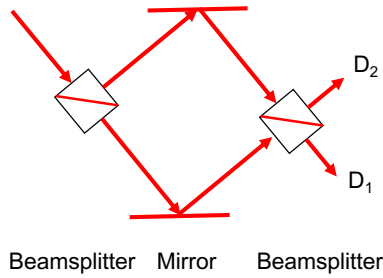
Gravity measurement with atoms offers advantages over classical methods as particles act as ideal test masses. Unlike traditional methods, atoms are immutable meaning quantum systems operate with a universal reference mass unaffected by fabrication tolerances. By utilising optical, magnetic and radio frequency interactions, atoms can be manipulated for experimental purposes to make various measurements. Atom interferometry is such an experimental technique relying on the wave-particle duality exhibited by atoms. This concept underpins quantum mechanics and describes how atoms have both wave-like and particle-like properties [22–24]. In contrast to optical interferometers in an atom interferometer, the splitting, reflection and recombining are realised by light pulses. Consequently, an atom interferometer is often likened to a Mach-Zehnder interferometer with the roles of light and matter exchanged.

A Mach-Zehnder sequence consists of two beamsplitters separated by a mirror and so analogously an atom interferometer consists of 3 pulses [22, 25]. A resonant laser pulse can drive transitions between the ground  $|g\rangle$  and excited state  $|e\rangle$  of a two level atom with the transition probability determined by the pulse length. This determines whether pulses act as a mirror or a beamsplitter. Assuming a group of atoms initialised in state  $|g\rangle$ , a pulse which puts the atoms into an equal superposition state of half  $|g\rangle$  and half  $|e\rangle$  is called a  $\pi/2$  pulse. A pulse which flips the state of the atoms is referred to as a  $\pi$  pulse in a process called population inversion. Naturally this means the Mach-Zehnder atom interferometer has a  $\frac{\pi}{2} - \pi - \frac{\pi}{2}$  pulse sequence. The initial  $\pi/2$  pulse creates an equal superposition of the ground and excited state, atoms receive a momentum impulse due to absorbing and emitting a photon due to momentum conservation. Consequently, the first pulse acts as a splitter as the excited state splits spatially from the ground state. The atoms undergo free evolution for a period  $T$  before a  $\pi$  pulse flips their state and redirects their propagation direction. The final  $\pi/2$  pulse then recombines the atomic wave packets. With zero perturbations the population distribution of the final two states is equal at the output. With perturbations, the probability of finding atoms in the excited state depends on the phase difference ( $\Delta\phi$ ) between the paths accumulated in freefall. When falling in the gravity field, the interferometer phase is given by equation 1.3a where the laser is assumed to remain on resonance and  $k_{eff}$  is the effective Raman wavevector.

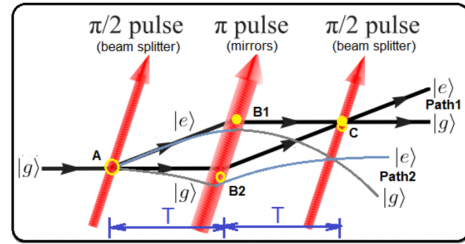
In practice the freefall induced Doppler shift causes the resonance frequency to drift such that the laser frequency must be chirped during interferometry. Consequently, the phase shift is described as  $\Delta\phi = k_{\text{eff}}gT^2 - \alpha T^2$  where  $\alpha$  is the laser chirp rate. Gravity can be determined by measuring the chirp rate cancelling it. The phase shifts associated with gravity manifest in the atomic state population (P), where the population of the excited state is given by equation 1.3b. Sensitivity is proportional to  $T^2$  and is further enhanced by measuring many atoms simultaneously, reducing the quantum shot noise limit. This working principle underpins the construction of atomic sensors with performance surpassing those of classical sensors.

$$\Delta\phi = k_{\text{eff}}gT^2. \quad (1.3a)$$

$$P = \frac{1}{2}(1 - \cos(\Delta\phi)). \quad (1.3b)$$



(a) Optical Interferometer.



(b) Atom Interferometer.

Figure 1.1: Comparison between optical and atom interferometer both in Mach-Zehnder configuration. Path 1 and path 2 (Fig. 1.1b) represent the trajectories of atom clouds with and without homogeneous gravity. Modified from [10].

Table 1.4: State-of-the-art absolute gravimeters for applications outside laboratories. \*Sensor head only

Group / Device	Principle	Bandwidth	Sensitivity	Size / Mass	References
Berlin / GAIN	$^{87}\text{Rb}$ Fountain	0.7 Hz	$96 \text{ nms}^{-2} / \sqrt{\text{Hz}}$	2010L / 160 kg	[26–28]
$\mu\text{QUANS}$ / AQG-A01	$^{87}\text{Rb}$ Drop	2 Hz	$500 \text{ nms}^{-2} / \sqrt{\text{Hz}}$	430L / 100 kg	[8, 29]
Zhejiang / CAAG	$^{87}\text{Rb}$ Drop	2 Hz	$3000 \text{ nms}^{-2} / \sqrt{\text{Hz}}$	625L / 70 kg	[30]
ONERA / GIRAFE	$^{87}\text{Rb}$ Drop	10 Hz	$8000 \text{ nms}^{-2} / \sqrt{\text{Hz}}$	16L* / N/A	[5, 31, 32]
Berkeley / MAI	$^{87}\text{Rb}$ Drop	N/A	$370 \text{ nms}^{-2} / \sqrt{\text{Hz}}$	1360L / N/A	[9]
SYRTE / CAG	$^{87}\text{Rb}$ Drop	3 Hz	$57 \text{ nms}^{-2} / \sqrt{\text{Hz}}$	2550L / N/A	[33]
Micro-g LaCoste / FG5-X	Free falling corner cube	1 Hz	$150 \text{ nms}^{-2} / \sqrt{\text{Hz}}$	1500L / 150 kg	[34]



### 1.4.1 State of the art

Since conception efforts have been made to improve atom interferometer performance while exploring different potential applications. The zero drift and unparalleled sensitivity offered makes it exciting for oil/mineral exploration, geodesy and inertial navigation to name but a few applications [35–37]. In fundamental physics atom interferometers have determined the Newtonian gravitational constant [38], the fine structure constant [39], SI unit of mass [40] and tested the weak equivalence principle [41]. Future applications might include space applications [42] such as detecting gravitational waves [43] or dark energy [44] or fundamental tests of general relativity [45]. The natural route to high sensitivity exists through long free-falling distances with [46] atomic fountains often utilised to increase interrogation time [47]. Systems typically operate with millions of atoms and interrogation times of a few 100 ms yielding sensitivities of order  $10 \text{ ng}/\sqrt{\text{Hz}}$ . The most sensitive device is a 10 m tower with a 1 s interrogation time and a per shot sensitivity of  $6.7 \times 10^{-12} \text{ g}$ . Alternatively, techniques like large momentum transfer (LMT) offer a potential route to performance improvements without increasing instrument size [48–50]. On the commercial side, projects such as iSense, QG-1 and GIF have improved compactness and portability of quantum sensors [51–53]. Moreover, in recent years various startups have been founded focusing on quantum sensing supported by a significant increase in investment (Q-CTRL, Muquans, and AOSense) [54–56]. As this thesis explores high-bandwidth

operation a brief note on this is provided. Currently, a laboratory instrument has demonstrated  $\mu\text{g}/\sqrt{\text{Hz}}$  sensitivities at 60 Hz operation. Increasing the data rate to 100 Hz with shot-noise limited detection could potentially reach a sensitivity of  $\sim 1 \times 10^{-7} \text{ g}/\sqrt{\text{Hz}}$ . The device relies heavily on recapturing atoms between cycles as reloading the magneto-optical trap (MOT) from background vapour within time constraints is impractical [57]. Overall, current research and development in quantum sensing promises disruptive technologies, with most remaining challenges being engineering-related [58].

## 1.5 Data Rate and Bandwidth

Before proceeding, a proper distinction between data rate and bandwidth is essential. As mentioned in section 1.4, in order to measure gravity, the chirp rate of the Raman laser is scanned to generate interferometric fringes. Typically, gravity extraction is achieved by taking multiple measurements or shots. The rate at which these shots are acquired represents the bandwidth of the system. For example, assume a fringe consisting of 20 points with a bandwidth of 1 Hz with gravity measured to an accuracy of  $1 \times 10^{-8} \text{ g}$ . With the given bandwidth, a single gravity measurement takes 20 s, resulting in a data rate of 0.05 Hz and a sensitivity of  $4.5 \times 10^{-8} \text{ g}/\sqrt{\text{Hz}}$ . In contrast, work has explored the possibility of extracting fringe information from a single shot. This is addressed by a technique known as phase shear readout (PSR) which creates a spatial variation in the atomic transition probability

which can be observed by imaging the atom cloud. Therefore, this technique eliminates the need for multiple shots with varying phases to achieve an interference fringe. Instead, the contrast of each shot and the interferometer phase can be inferred from the depth of modulation in the spatial fringe pattern. By extracting interference phase information from a single shot the system bandwidth would be equivalent to data rate [50]. However, the method is not widely implemented. This project aims to enhance the data rate by significantly improving the system bandwidth, targeting 100 Hz operation instead of typical bandwidths of around 1 Hz. Figure 1.2 compares the techniques showing spatial fringes obtained in a single shot at low bandwidth with multiple shots at high bandwidth. Long term, achieving successful implementation of single shot measurements at high bandwidth would be highly impactful, enabling high-data rate gravity streams although this is beyond the scope of this work.

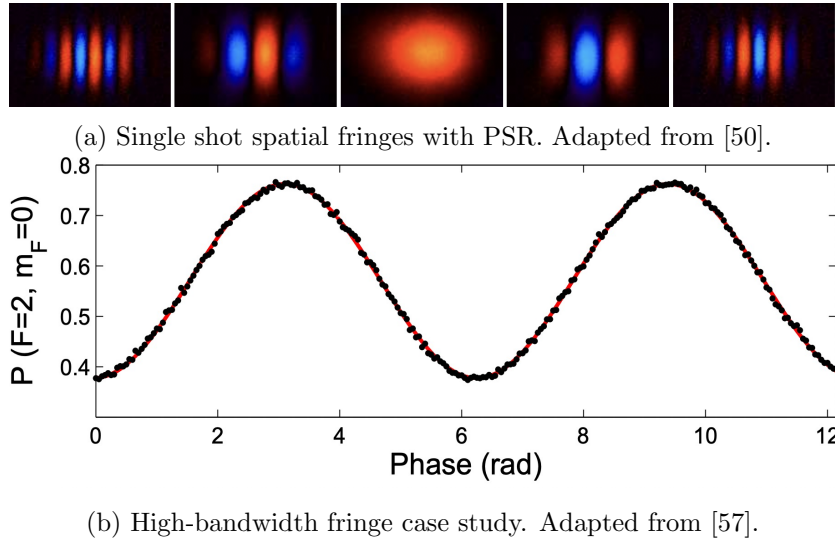


Figure 1.2: Comparison of fringes obtained in a single shot at low bandwidth versus fringes obtained through multiple shots at high bandwidth.

## 1.6 Quantum Navigation

Quantum sensing shows promise for applications in inertial navigation systems (INS) although adapting atom interferometers for dynamic environments remains challenging [59]. One crucial requirement is high-bandwidth operation which is quite rare in atom interferometers [57, 60, 61]. High-bandwidth operation is supported by some of the relative gravimeters in Table 1.3 although MEMS devices are not particularly sensitive and would incur significant drifts whereas the superconducting spheres would be impractical and slow for the application environments. These shortcomings motivate the intrinsic long-term sensitivity offered by absolute quantum gravimeters. However, similar to classical methods, cold atom inertial navigation relies

on measuring accelerations and angular rates to estimate position, velocity, and orientation. This means even a perfect quantum navigator using dead-reckoning will accumulate errors over time leading to drift [62,63]. To mitigate this, INSs are typically augmented with position fixes obtained from Global Navigation Satellite Systems (GNSS), such as GPS. Unfortunately, such systems are susceptible to jamming and spoofing [64,65]. Alternative methods based on detecting environmental features face challenges in marine applications due to the absence of distinctive surface features and the security risks of sonar usage. Quantum gravity sensing offers an alternative approach by leveraging gravitational field variations to achieve map matching and provide absolute position fixes. Gravity signals are globally present, immune to jamming or spoofing and freely accessible through gravity databases [66,67]. Quantum systems hold great potential for deployable gravity based map matching systems offering accuracy without frequent calibration [68,69]. However, experimental bandwidth limitations, influenced by atomic sample preparation time, hinder high-bandwidth operation. Typical experiments operate at  $\sim 1$  Hz bandwidth, which is insufficient for dynamic applications. To address this, a shift towards high-bandwidth operation is needed, even if it means sacrificing sensitivity. Reloading the magneto-optical trap (MOT) solely from background vapour within time constraints is impractical, highlighting the significance of recapturing atoms between cycles.

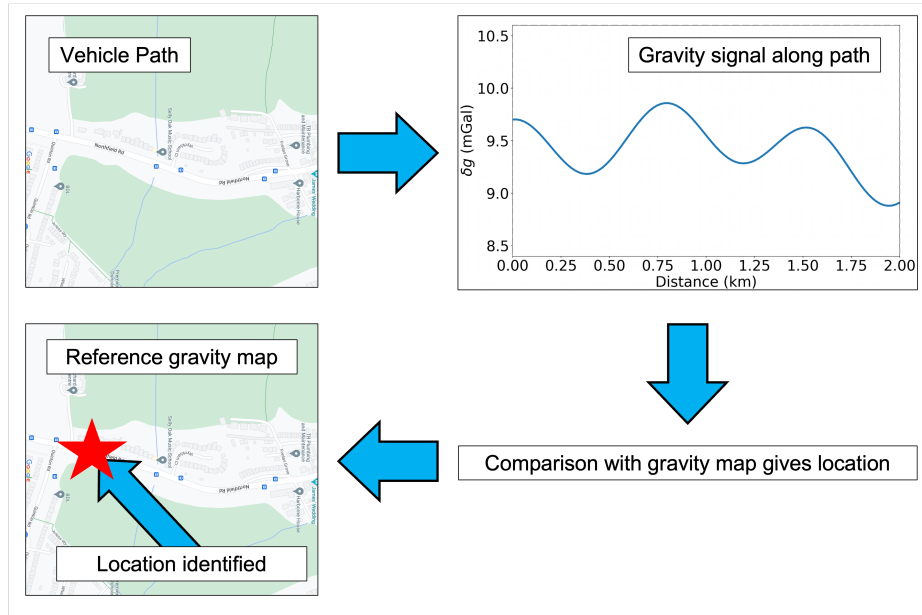


Figure 1.3: Conceptual illustration of gravity map-matching for inertial navigation.

## 1.7 Thesis Structure

**Raman Atom Interferometry:** A theoretical description of atom interferometry is presented. The sensitivity function is introduced to gauge how noise sources influence the gravity measurement.

**Laser Cooling and Trapping:** Cold-atom generation is described with simulations performed to explore trap efficiency at high-bandwidth operation.

**High Data Rate Atom Interferometry:** High-data rate interferometry is presented drawing comparisons with traditional approaches. Numerical simulations examine temperature and Raman degeneracy and how they dictate the workable parameter space. Performance limited sensitivity is then estimated

for high-bandwidth operation.

**Experimental Setup:** The opto-mechanical structure, vacuum, coil and control systems are presented. A characterisation of MOT performance is provided with an investigation into recapture dynamics. Moving molasses and sub-Doppler cooling are examined which are critical for preparing the atomic sample on millisecond timescales.

**Raman Laser System:** The frequency agile Raman laser system is presented discussing its implementation and performance with attention given to spectral purity.

**Results:** The atom interferometer realisation is presented and analysed. The sensitivity budget and accuracy of the gravimeter is explored.

**Conclusion:** The project is reviewed providing a pathway toward the next generation of quantum sensors.

## Chapter 2

# Raman Atom Interferometry

This chapter expands on 1.4 by discussing stimulated Raman transitions, which are fundamental to this work. These transitions induce momentum recoil to manipulate atomic wave-packets in the interferometer by separating, deflecting, and recombining them. The output of the interferometer is determined by the populations of the measured atomic states. The chapter begins by explaining the interaction of stimulated Raman transitions with a three-level system, using this framework to analyse a Mach-Zehnder  $\frac{\pi}{2} - \pi - \frac{\pi}{2}$  sequence. The sensitivity function is then introduced to assess the impact of different noise sources on interferometer phase noise [70–72]. This chapter follows closely the thesis of Rammeloo with additional reference to Stray and Schmidt. [73–75].



## 2.1 Stimulated Raman Transitions

Stimulated Raman transitions provide coherent manipulation of atomic states essential for atom interferometry. This process couples two long-lived states  $|a\rangle$  and  $|b\rangle$  in a two photon process. This approach is desirable for  $^{87}\text{Rb}$  as the imparted momentum can be  $\sim 10^5$  times larger than driving a single photon microwave transition between states.

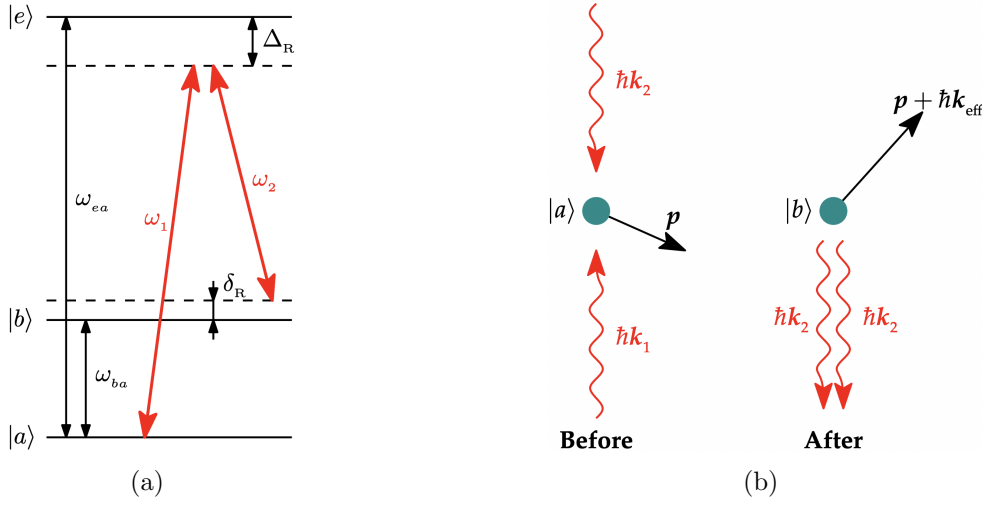


Figure 2.1: Illustration of a stimulated Raman transition coupling stable atomic states  $|a\rangle$  and  $|b\rangle$  via two light fields and an intermediate state  $|e\rangle$ . a.) Long lived states  $|a\rangle$  and  $|b\rangle$ , separated by  $\omega_{ba}$  can be coupled by a two photon stimulated Raman transition. Note diagram is not to scale as  $\omega_1, \omega_2 \gg \omega_{ba}, \delta, \Delta$ . b.) An atom absorbs a photon from one beam and undergoes stimulated emission from the virtual level  $|e\rangle$ . The atom gains momentum equal to the difference between the wavevectors  $k_{\text{eff}} = k_1 - k_2$ . This is maximised for the depicted counter-propagating configuration. Adapted from [73].

This is beneficial as interferometer sensitivity is proportional to the effective wavevector of the transition (section 2.3). Consider two hyperfine ground states with separation  $\sim$  few GHz and an excited state separated from the

ground states by  $\sim 100$  THz. Stimulated Raman transitions couple these ground states using two laser light fields with angular frequencies close to the optical transition with a shared intermediate state  $|e\rangle$ . The two transitions differ only slightly by an amount close to  $\omega_{ba}$ . The transition is driven from  $|a\rangle$  to  $|b\rangle$  by simultaneously absorbing a photon of energy  $\hbar\omega_1$  from the first light field and the stimulated emission of a photon of energy  $\hbar\omega_2$  from the second. Decoherence from spontaneous emission is limited by detuning the light fields from  $\omega_{ea}$ . The resonance condition for efficient coupling between  $|a\rangle$  and  $|b\rangle$  can be found from the energy conservation of the process depicted in figure 2.1b. Consider an atom in state  $|a\rangle$  with momentum  $p$ , absorbing a photon from the first light field imparts a momentum  $\hbar k_1$ , where  $k_1$  is the wavevector. Stimulated emission of a photon with wavevector  $k_2$  from the second light field imparts an additional momentum recoil of  $\hbar k_2$ . Overall the transition into state  $|b\rangle$  can be described by an effective wavevector  $k_{\text{eff}} \equiv k_1 - k_2$  with equation 2.1 describing the two-photon detuning ( $\delta_R$ ) from resonance.

$$\delta_R = \omega_1 - \omega_2 - \omega_{ba} + \frac{|\mathbf{p}|^2}{2m\hbar} - \frac{|\mathbf{p} + \hbar\mathbf{k}_{eff}|^2}{2m\hbar}. \quad (2.1)$$

To suppress single photon scattering frequencies  $\omega_1$  and  $\omega_2$  are detuned by a frequency  $\Delta_R$  from the virtual level  $|e\rangle$ . To enable spontaneous emission to be completely neglected,  $\Delta_R \gg \delta$ . This detuning  $\Delta_R$  is referred to as the one-photon detuning and is defined by equation 2.2.

$$\Delta_R = \omega_{\text{ea}} - \omega_1 + \frac{|\mathbf{p}|^2}{2m\hbar} - \frac{|\mathbf{p} + \hbar\mathbf{k}_1|^2}{2m\hbar}. \quad (2.2)$$

At this stage it is beneficial to identify the energy of each state.

$$\hbar\omega_a = \frac{|\mathbf{p}|^2}{2m}. \quad (2.3a)$$

$$\hbar\omega_b = \frac{|\mathbf{p} + \hbar\mathbf{k}_{eff}|^2}{2m} + \hbar\omega_{ba}. \quad (2.3b)$$

$$\hbar\omega_e = \frac{|\mathbf{p} + \hbar\mathbf{k}_1|^2}{2m} + \hbar\omega_{ea}. \quad (2.3c)$$

A semi-classical approach is then applied with the atom treated as a quantum object in a classical light field. In this basis the internal energy and external momentum are represented as the tensor product of two Hilbert spaces such that for an atom with an internal state  $|x\rangle$  and momentum  $|p_x\rangle$ , the state can be expressed as  $|x, p_x\rangle = |x\rangle \otimes |p_x\rangle$ . The atomic wavefunction is a linear combination of all states, with time varying coefficients. The square of these coefficients give the probability of the atom being in the state at a certain time. The wavefunction for the three level system for a single momentum  $\mathbf{p}$  is given by equation 2.4.

$$\begin{aligned}
|\Psi(t)\rangle = & C_{a,\mathbf{p}}(t) |a, \mathbf{p}\rangle + C_{b,\mathbf{p}+\hbar\mathbf{k}_{eff}}(t) |b, \mathbf{p} + \hbar\mathbf{k}_{eff}\rangle \\
& + C_{e,\mathbf{p}+\hbar\mathbf{k}_1}(t) |e, \mathbf{p} + \hbar\mathbf{k}_1\rangle.
\end{aligned} \tag{2.4}$$

Coefficients  $C_{x,\mathbf{p}_x}$  evolve with a fast oscillation component given by equations 2.3 but also with a slow varying coefficient giving equation 2.5.

$$C_{x,\mathbf{p}_x}(t) = c_{x,\mathbf{p}_x}(t)e^{-i\omega_x t}. \tag{2.5}$$

To determine the state evolution one must solve the time dependent Schrödinger equation for the wavefunction in equation 2.4.

$$i\hbar \frac{d}{dt} |\Psi_P(t)\rangle = \hat{\mathcal{H}} |\Psi_P(t)\rangle. \tag{2.6}$$

### 2.1.1 Three level atom in a light field

Solving the Schrödinger equation requires the Hamiltonian of the system. In this instance the Hamiltonian consists of three parts.  $\mathcal{H}_P$ , is connected to the kinetic energy of the atom via the momentum operator  $\hat{p}$ ,  $\mathcal{H}_A$  acts on the internal energy levels of the atom and  $\mathcal{H}_{int}$  is associated with the interaction between the atom and the light field, via the electric dipole operator. The total Hamiltonian is the sum of these components given by equations 2.7.

$$\hat{\mathcal{H}} = \hat{\mathcal{H}}_P + \hat{\mathcal{H}}_A + \hat{\mathcal{H}}_{int}. \tag{2.7a}$$

$$\hat{\mathcal{H}}_P = \frac{\hat{\mathbf{p}}^2}{2m}. \quad (2.7b)$$

$$\hat{\mathcal{H}}_A = \hbar\omega_e |e\rangle \langle e| + \hbar\omega_a |a\rangle \langle a| + \hbar\omega_b |b\rangle \langle b|. \quad (2.7c)$$

$$\hat{\mathcal{H}}_{\text{int}} = -\hat{\mathbf{d}} \cdot \hat{\mathbf{E}}. \quad (2.7d)$$

In the semi-classical framework the two-photon transition is represented as the sum of two classical plane waves with electric field given by equation 2.8.

$$\mathbf{E}(\mathbf{r}, t) = \mathbf{E}_1 \cos(\mathbf{k}_1 \cdot \mathbf{r} - \omega_1 t + \phi_1) + \mathbf{E}_2 \cos(\mathbf{k}_2 \cdot \mathbf{r} - \omega_2 t + \phi_2). \quad (2.8)$$

$E_1$  and  $E_2$  the amplitude and polarisation of the two laser beams.  $\phi_1$  and  $\phi_2$  are their respective phase offsets with respect to a common reference and are assumed to be constant during the interaction with the atom. Substituting equations 2.4, 2.7 and 2.8 into the Schrödinger equation (equation 2.6) results in three coupled equations.

$$\frac{dc_{a,\mathbf{p}}(t)}{dt} = -ic_{e,\mathbf{p}+\hbar\mathbf{k}_1} \Omega_1 e^{-i(\Delta t + \phi_1)}. \quad (2.9a)$$

$$\frac{dc_{b,\mathbf{p}+\hbar\mathbf{k}_{eff}}(t)}{dt} = -ic_{e,\mathbf{p}+\hbar\mathbf{k}_1} \Omega_2 e^{-i((\Delta+\delta)t + \phi_2)}. \quad (2.9b)$$

$$\frac{dc_{e,\mathbf{p}+\hbar\mathbf{k}_1}(t)}{dt} = -ic_{a,\mathbf{p}} \Omega_1^* e^{i(\Delta t + \phi_1)} - ic_{b,\mathbf{p}+\hbar\mathbf{k}_{eff}} \Omega_2^* e^{i((\Delta+\delta)t + \phi_2)}. \quad (2.9c)$$

Where the Rabi frequency is introduced and defined as

$$\Omega_1 \equiv -\frac{\langle a | \hat{\mathbf{d}} \cdot \hat{\mathbf{E}}_1 | e \rangle}{2\hbar}. \quad (2.10a)$$

$$\Omega_2 \equiv -\frac{\langle b | \hat{\mathbf{d}} \cdot \hat{\mathbf{E}}_2 | e \rangle}{2\hbar}. \quad (2.10b)$$

The Rabi frequency describes the coupling and rate of population transfer between the ground and intermediate state. As discussed previously spontaneous emission is suppressed for  $\Delta \gg |\delta|, |\Omega_1|, |\Omega_2|$ . This results in the time dependent oscillation of coefficients  $c_{a,\mathbf{p}}$  and  $c_{b,\mathbf{p}+\hbar\mathbf{k}_{\text{eff}}}$  being much less than the terms oscillating at frequency  $\Delta$ . Equation 2.9c can be integrated using adiabatic elimination neglecting the time dependence of  $c_{a,\mathbf{p}}$  and  $c_{b,\mathbf{p}+\hbar\mathbf{k}_{\text{eff}}}$  with the oscillations at frequency  $\Delta$  averaging out. This eliminates the intermediate state  $|e\rangle$  reducing the system to a coupled two-level system.

$$\frac{dc_{a,\mathbf{p}}(t)}{dt} = i\frac{|\Omega_1|^2}{\Delta}c_{a,\mathbf{p}}(t) + i\frac{\Omega_1\Omega_2^*}{\Delta}c_{b,\mathbf{p}+\hbar\mathbf{k}_{\text{eff}}}(t)e^{i(\delta t+\phi_2-\phi_1)}. \quad (2.11a)$$

$$\frac{dc_{b,\mathbf{p}+\hbar\mathbf{k}_{\text{eff}}}(t)}{dt} = i\frac{\Omega_1\Omega_2^*}{\Delta}c_{a,\mathbf{p}}(t)e^{-i(\delta t+\phi_2-\phi_1)} + i\frac{|\Omega_2|^2}{\Delta}c_{b,\mathbf{p}+\hbar\mathbf{k}_{\text{eff}}}(t). \quad (2.11b)$$

Atom light interaction changes the energy of each state in process called light shift (A.C. Stark effect). The light shift alters the Rabi frequency leading to the introduction of  $\Omega_{\text{AC}}$  given by equation 2.12.

$$\Omega_{AC} \equiv \frac{|\Omega_2|^2}{4\Delta} + \frac{|\Omega_1|^2}{4\Delta}. \quad (2.12)$$

In addition the difference of the Rabi frequencies is connected to the detuning caused by the light shifts. Practically the effects of the light shift can be eliminated by fixing the intensities of the Raman laser components.

$$\delta_{AC} \equiv \frac{|\Omega_2|^2}{4\Delta} - \frac{|\Omega_1|^2}{4\Delta}. \quad (2.13)$$

The effective Rabi frequency can also be defined describing the transition rate between the two ground states with phase term  $\phi_{eff} = \phi_1 - \phi_2$  originating from the light interaction.

$$\Omega_{eff} = \frac{\Omega_2^* \Omega_1}{2\Delta} e^{i(\phi_1 - \phi_2)}. \quad (2.14)$$

To solve the coupled rate equations (2.11) requires the basis to be switched to a rotating frame such that the Hamiltonian is time independent. This allows two level solutions to be applied and introduces a phase term rotating at a frequency  $\Omega_{AC} \pm \delta$ . The derivation introduces a generalised Rabi frequency,  $\Omega_R$  incorporating light shifts and frequency detuning.

$$\Omega_R \equiv \sqrt{\Omega_{eff}^2 + (\delta - \delta_{AC})^2}. \quad (2.15)$$

Finally the solutions for the coefficients  $c_{a,\mathbf{p}}$  and  $c_{b,\mathbf{p}+\hbar\mathbf{k}_{\text{eff}}}$  after a time  $(t_0 + \tau)$ .

$$c_{a,\mathbf{p}}(t_0 + \tau) = e^{i(\Omega_{AC}+\delta)\tau/2} \left\{ \left[ \cos\left(\frac{\Omega_R\tau}{2}\right) + i\frac{\delta_{AC}-\delta}{\Omega_R} \sin\left(\frac{\Omega_R\tau}{2}\right) \right] c_{a,\mathbf{p}}(t_0) + \left[ i\frac{\Omega_{\text{eff}}}{\Omega_R} \sin\left(\frac{\Omega_R\tau}{2}\right) e^{i(\delta t_0 + \phi_{\text{eff}})} \right] c_{b,\mathbf{p}+\hbar\mathbf{k}_{eff}}(t_0) \right\}. \quad (2.16a)$$

$$c_{b,\mathbf{p}+\hbar\mathbf{k}_{\text{eff}}}(t_0 + \tau) = e^{i(\Omega_{AC}-\delta)\tau/2} \left\{ \left[ i\frac{\Omega_{\text{eff}}}{\Omega_R} \sin\left(\frac{\Omega_R\tau}{2}\right) e^{-i(\delta t_0 + \phi_{\text{eff}})} \right] c_{a,\mathbf{p}}(t_0) + \left[ \cos\left(\frac{\Omega_R\tau}{2}\right) - i\frac{\delta_{AC}-\delta}{\Omega_R} \sin\left(\frac{\Omega_R\tau}{2}\right) \right] c_{b,\mathbf{p}+\hbar\mathbf{k}_{eff}}(t_0) \right\}. \quad (2.16b)$$

In summary, the three system level can be reduced into an effective two level system eliminating the intermediate state.  $\Omega_{\text{eff}}$  is the effective Rabi frequency of the two level system.

## 2.2 Rabi Oscillations

The populations of the two level system are obtained by computing the modulus squared of each coefficient. For an atom in the ground state at  $t_0$ , i.e  $c_{a,\mathbf{p}}(t_0) = 1$  and  $c_{b,\mathbf{p}+\hbar\mathbf{k}_{eff}}(t_0) = 0$ , the probability of detecting the atom in each of the states after a pulse of length  $\tau$  is given by equations 2.17 and 2.47 respectively.



$$P_a(\mathbf{p}, t_0 + \tau) = |c_{a,\mathbf{p}}(t_0 + \tau)|^2 = \cos^2\left(\frac{\Omega_R \tau}{2}\right) + \left|\frac{\delta_{AC} - \delta}{\Omega_R}\right|^2 \sin^2\left(\frac{\Omega_R \tau}{2}\right). \quad (2.17)$$

$$\begin{aligned} P_b(\mathbf{p} + \hbar \mathbf{k}_{eff}, t_0 + \tau) &= |c_{b,\mathbf{p} + \hbar \mathbf{k}_{eff}}(t_0 + \tau)|^2 = \\ &= \left|\frac{\Omega_{eff}}{\Omega_R}\right|^2 \sin^2\left(\frac{\Omega_R \tau}{2}\right) = \left|\frac{\Omega_{eff}}{\Omega_R}\right|^2 \frac{1 - \cos(\Omega_R \tau)}{2} \end{aligned} \quad (2.18)$$

The equations describe an oscillating population between two states at frequency  $\Omega_R$  known as Rabi oscillations. Choosing long lived states means the atomic population does not undergo radiative decay as in the traditional two level atom picture. As a result total inversion of the atomic states is possible. The light shift detuning can be nulled and grouped such that  $\delta_{tot} = \delta_{AC} - \delta$ . Figure 2.2 highlights how detuning determines the oscillation amplitude and frequency for variable  $\delta_{tot}$ . As the detuning difference  $\delta_{AC} - \delta$  tends to zero the maximum population transfer tends to 1 with the oscillation frequency tending to  $\Omega_{eff}$ .

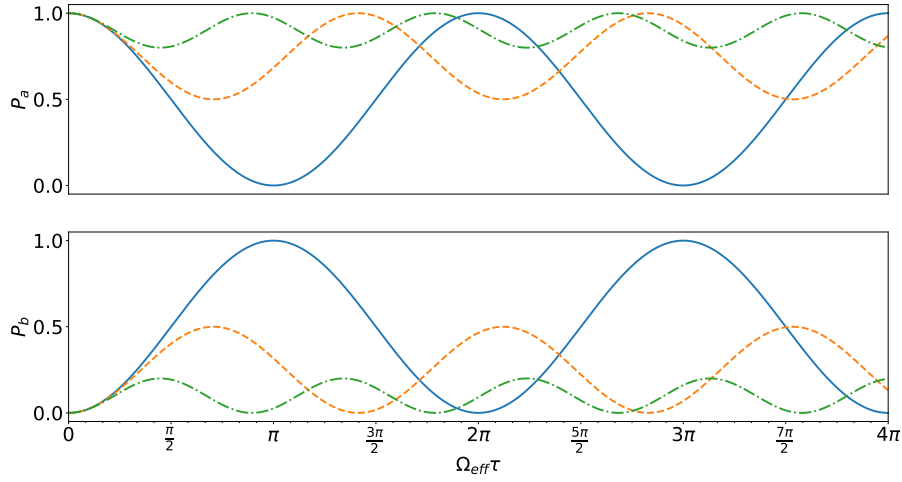


Figure 2.2: Probability for an atom to be in the ground,  $P_a$  or excited state  $P_b$  after a pulse of variable duration is applied. Rabi oscillations are plotted for variable detunings,  $\frac{\delta_{\text{tot}}}{\Omega_{\text{eff}}} = 0$  (blue solid), 1 (orange dashed), 2 (green dash dotted). Since maximum transfer results in a cleaner quantum state it is desirable to minimise  $\delta_{\text{tot}}$ .

Equation 2.19 expresses Rabi frequency in light intensity rather than electric field.  $\Gamma$  is the transition linewidth and  $I_{\text{sat}}$  is the saturation intensity computed from the coupling strength and polarisation of the transition.

$$|\Omega| = \sqrt{\frac{I}{I_{\text{sat}}}} \frac{\Gamma}{\sqrt{2}}. \quad (2.19)$$

Following this the effective Rabi frequency is expressed as in equation 2.20. This shows how the two-photon transition rate can be increased by higher light intensities or reducing the single photon detuning  $\Delta_R$ .

$$|\Omega_{\text{eff}}| = \frac{\sqrt{I_1 I_2} \Gamma^2}{4 I_{\text{sat}} \Delta_R}. \quad (2.20)$$

## 2.3 Raman Configuration

The free falling motion of the atoms creates an additional Doppler shift. The velocity dependence originates from the shift  $\mathbf{v} \cdot \mathbf{k}_{\text{eff}}$  where  $\mathbf{v}$  is the velocity vector and  $\mathbf{k}_{\text{eff}}$  is the effective wavevector. Providing other resonance conditions are fulfilled ( $\delta_{\text{tot}} = 0$ ), this shift manifests in the generalised Rabi frequency as in equation 2.21.

$$\Omega_R = \sqrt{\Omega_{\text{eff}}^2 + (\mathbf{v} \cdot \mathbf{k}_{\text{eff}})^2}. \quad (2.21)$$

Aligning the Raman beams with respect to the  $z$  axis results in a resonant velocity class,  $v_R$  for which the Doppler shift is cancelled. The Doppler shift can then be expressed as  $(v_z - v_R)|\mathbf{k}_{\text{eff}}|$ . For atoms in an atomic cloud there are two relevant velocities: the cloud's centre of mass and the atom's thermal velocity. As the Raman beams are co-axial the frequencies can be delivered from the same or opposing directions. These configurations are referred to as co-propagating and counter-propagating respectively. The effective wavevector,  $\mathbf{k}_{\text{eff}} = \mathbf{k}_1 - \mathbf{k}_2$  determines the magnitude of momentum transferred to the atom. For the co-propagating case the momentum transfer is negligible with  $\mathbf{k}_{\text{eff}} = |\mathbf{k}_1| - |\mathbf{k}_2|$  making the Doppler shift  $\mathbf{v} \cdot \mathbf{k}_{\text{eff}}$  negligible. In contrast, in the counter-propagating case  $\mathbf{k}_{\text{eff}} = |\mathbf{k}_1| + |\mathbf{k}_2|$  creates much larger momentum transfer. While this is desirable for interferometer sensitivity the shift in the Raman resonance frequency is non-negligible such that the Raman laser

frequency must be chirped during free fall.

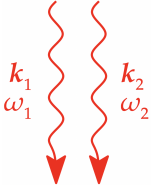
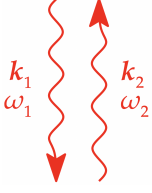
Configuration	Co-propagating	Counter-propagating
		
Momentum kick	$\hbar k_1  - \hbar k_2 $	$\hbar k_1  + \hbar k_2 $
Recoil velocity	$0.10 \mu\text{ms}^{-1}$	$12 \text{ mms}^{-1}$
Doppler shift	$k_1 \cdot v - k_2 \cdot v$	$k_1 \cdot v + k_2 \cdot v$
Velocity selection	Doppler insensitive	Doppler sensitive

Table 2.1: Properties of stimulated Raman transitions for different beam configurations.

## 2.4 Velocity Selection

Adopting the counter-propagating configuration makes fulfilling the resonance condition impossible for all atoms in an ensemble. As a result not all atoms will undergo a transition. Substituting the expression for the Doppler shift into equation 2.21 gives the generalised Rabi frequency in terms of an atom's velocity along the z axis.

$$\Omega_R(v_z) = \sqrt{\Omega_{\text{eff}}^2 + (v_z - v_R)^2 |k_{\text{eff}}|^2}. \quad (2.22)$$

An expression for the velocity dependence of the excited state population after a  $\pi$  pulse is obtained by substituting equation 2.22 into equation 2.47.

$$P_b(v_z) = \frac{\pi^2}{4} \text{sinc}^2 \left( \frac{\pi}{2} \sqrt{1 + \frac{(v_z - v_R)^2 |k_{\text{eff}}|^2}{|\Omega_{\text{eff}}|^2}} \right) \quad (2.23)$$

Atomic clouds are assumed to have a Maxwell-Boltzmann distribution of velocities  $v_z$  as in equation 2.24.  $\bar{v}_z$  is the mean velocity of the cloud along the Raman axis and  $\sigma_{v,z}$  is the 1D velocity spread around this.

$$f_v(v_z) = \frac{1}{\sqrt{2\pi}\sigma_{v,z}} \exp \left[ -\frac{(v_z - \bar{v}_z)^2}{2\sigma_{v,z}^2} \right]. \quad (2.24)$$

The distribution of atoms in the excited state  $|b\rangle$  is given by the ensemble average in equation 2.25. Figure 2.3 illustrates the portion of the cloud's velocity distribution addressed by a  $\pi$  pulse.

$$\langle P_{b,\pi} \rangle = \int_{-\infty}^{\infty} P_b(v_z) f_v(v_z) dv_z. \quad (2.25)$$

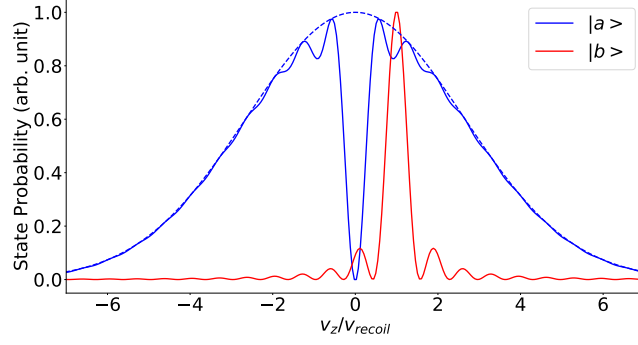


Figure 2.3: A resonant  $\pi$  pulse transfers a portion of the velocity distribution from state  $|a\rangle$  to  $|b\rangle$ . The dotted line shows the ensemble distribution before transfer. The velocity is scaled to the recoil velocity of the two-photon transition where  $v_{\text{recoil}} = \hbar|k_{\text{eff}}|/m$ . The model assumes a  $10\,\mu\text{K}$  cloud with an effective Rabi frequency of  $\Omega_{\text{eff}} = 2\pi \times 10\,\text{kHz}$ . For more efficient transfer the temperature should be reduced or the effective Rabi frequency increased.

The integral in equation 2.25 can be approximated by treating the central peak in equation 2.23 as a Gaussian with RMS spread given by  $\sim \frac{|\Omega_{\text{eff}}|}{|k_{\text{eff}}|}$ .

$$\begin{aligned} \langle P_{b,\pi} \rangle &\approx \frac{1}{\sigma_{v,z}\sqrt{2\pi}} \int_{-\infty}^{\infty} \exp\left[-\frac{(v_z - \bar{v}_z)^2}{2\sigma_{v,z}^2}\right] \exp\left[-\frac{(v_z - v_R)^2|k_{\text{eff}}|^2}{|\Omega_{\text{eff}}|^2}\right] dv_z \\ &= \frac{\sigma_{v,\pi}}{\sigma_{v,z}} \exp\left[-\frac{1}{2} \frac{|k_{\text{eff}}|^2}{|k_{\text{eff}}|^2\sigma_{v,z}^2 + |\Omega_{\text{eff}}|^2} (\bar{v}_z - v_R)^2\right]. \end{aligned} \quad (2.26)$$

$$\sigma_{v,\pi} = \frac{\sigma_{v,z}|\Omega_{\text{eff}}|}{\sqrt{|k_{\text{eff}}|^2\sigma_{v,z}^2 + |\Omega_{\text{eff}}|^2}}. \quad (2.27)$$

The highest population transfer of  $\sim \frac{\sigma_{v,\pi}}{\sigma_{v,z}}$  occurs when the Raman laser frequency is tuned to the centre of the velocity distribution ( $v_R = \bar{v}_z$ ). By measuring population transfer for variable laser detuning, temperature and

mean cloud velocity can be determined.

## 2.5 Inhomogeneities

The framework in section 2.4 neglects the effect of finite laser radius. To quantify this the probability of state transfer is averaged over an ensemble. This is a 6D integral over position and velocity but as integrals over  $z, v_x$  and  $v_y$  average to 1 it can be reduced to 3D and to 2D by switching to polar coordinates.  $P(t, \Omega(x, y), \delta(v_z))$  is the same as in equation 2.47 with  $\Omega(x, y)$  giving the Rabi frequency spatial dependence and  $\delta(v_z)$  representing the velocity dependence due to an atom's velocity component along the Raman beam axis.  $g(x, y, z)$  and  $g(v_x, v_y, v_z)$  denote Gaussian distributions for position and velocity respectively [76].

$$\Omega(x, y) = \Omega_{\text{eff}} \exp\left(-\frac{x^2 + y^2}{2(\sigma_{\text{RAMAN}}^2)}\right). \quad (2.28a)$$

$$\delta(v_z) = k_{\text{eff}} v_z. \quad (2.28b)$$

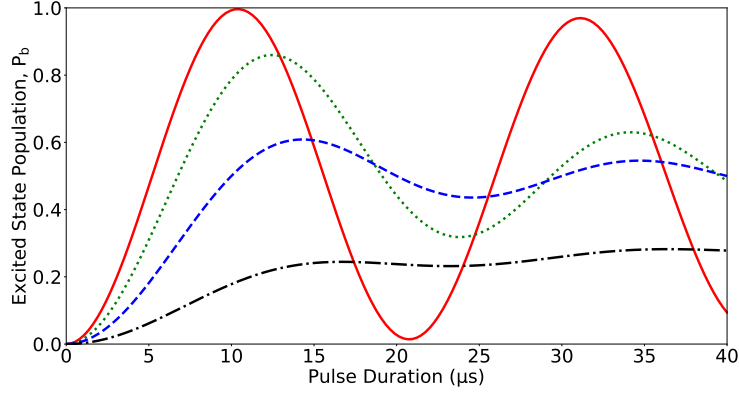
$$g_x(x, y, z) = \frac{1}{(2\pi)^{\frac{3}{2}} (\sigma_{x,\text{ensemble}})^3} \exp\left(-\frac{x^2 + y^2 + z^2}{2(\sigma_{x,\text{ensemble}})^2}\right). \quad (2.28c)$$

$$g_v(v_x, v_y, v_z) = \frac{1}{(2\pi)^{\frac{3}{2}} (\sigma_v)^3} \exp\left(-\frac{v_x^2 + v_y^2 + v_z^2}{2(\sigma_v)^2}\right). \quad (2.28d)$$

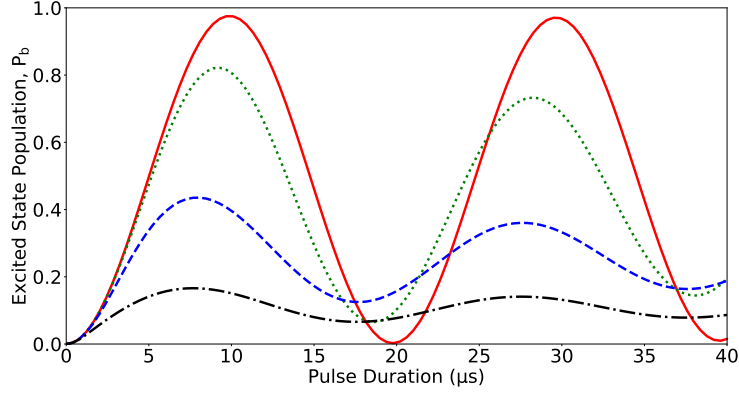
$$P_{\text{avg}} = \int_{-\infty}^{\infty} \int_{-\infty}^{\infty} P(t, \Omega(x, y), \delta(v_z)) g_x(x, y, z), g_v(v_x, v_y, v_z) d^3x d^3v. \quad (2.29)$$

Figure 2.4a compares ensemble averaged Rabi oscillations for variable cloud size. For clouds much smaller than the beam radius the transfer loss is negligible with atoms experiencing broadly the same Rabi frequency. When the cloud and beam size are comparable the spatial variation in the Rabi frequency is important. This results in atoms on the edge of the beam experiencing reduced Rabi frequencies. Consequently, the ensemble averaged Rabi cycle has reduced transfer and coherence. Note the condition for maximum transfer shifts to longer pulse durations as the average Rabi frequency is reduced. Figure 2.4b examines the effect of temperature on the cloud. In a similar manner transfer and coherence are reduced for increasing temperature. This occurs as the velocity spread increases variation in Rabi frequency washing out the Rabi oscillation. Note the condition for maximum transfer shifts to shorter pulse durations as the velocity induced Doppler shifts increase the average Rabi frequency.





(a) Spatially induced inhomogeneities exclusively.  $\sigma_{\text{cloud}}$ : (mm): 1.0 (solid red), 3.0 (green dotted), 5.0 (blue dashed), 10.0 (black dashed dot).



(b) Temperature induced inhomogeneities exclusively. Temperature ( $\mu\text{K}$ ): 0.1 (solid red), 1 (green dotted), 10 (blue dashed), 100 (black dashed dot)

Figure 2.4: Inhomogeneous Rabi flopping,  $\sigma_{\text{RAMAN}} = 5.0$  mm,  $\Omega_{\text{eff}} = 2\pi \times 50$  kHz.

## 2.6 Light Shift

When driving stimulated Raman transitions on the  $^{87}\text{Rb D}_2$  line the multi level nature of the atom becomes important. The hyperfine splitting of the excited  $5^2\text{P}_{3/2}$  level is shown in figure 2.5. In our experiment Raman transitions are driven between the two ground state energy levels,  $|5^2\text{S}_{1/2}, F = 1\rangle$

and  $|5^2S_{1/2}, F = 2\rangle$ . Naturally when driving the transition the coupling with all four excited levels becomes relevant. The light shifts for the ground and excited states can be written accounting for all interactions between the laser and atoms in equations 2.30a and 2.30b.

$$\Omega_a^{\text{AC}} = \sum_k \frac{|\Omega_{k,a,1}|^2}{4(\Delta + \Delta_k)} + \frac{|\Omega_{k,a,2}|^2}{4(\Delta + \Delta_k - \omega_{ba})}. \quad (2.30a)$$

$$\Omega_b^{\text{AC}} = \sum_k \frac{|\Omega_{k,b,1}|^2}{4(\Delta + \Delta_k + \omega_{ba})} + \frac{|\Omega_{k,b,2}|^2}{4(\Delta + \Delta_k)}. \quad (2.30b)$$

Accounting for the Clebsch-Gordon coefficients and the linear polarisation of the Raman light the above equations can be expanded

$$\Omega_a^{\text{AC}} = \frac{\Omega_1^2}{4} \left( \frac{5}{24\Delta} + \frac{1}{8(\Delta - \Delta_2)} \right) + \frac{\Omega_2^2}{4} \left( \frac{5}{24(\Delta - \omega_{ba})} + \frac{1}{8(\Delta - \Delta_2 - \omega_{ba})} \right). \quad (2.31a)$$

$$\Omega_b^{\text{AC}} = \frac{\Omega_1^2}{4} \left( \frac{1}{120(\Delta + \omega_{ba})} + \frac{1}{8(\Delta - \Delta_2 + \omega_{ba})} + \frac{1}{5(\Delta - \Delta_3 + \omega_{ba})} \right) + \frac{\Omega_2^2}{4} \left( \frac{1}{120\Delta} + \frac{1}{8(\Delta - \Delta_2)} + \frac{1}{5(\Delta - \Delta_3)} \right). \quad (2.31b)$$

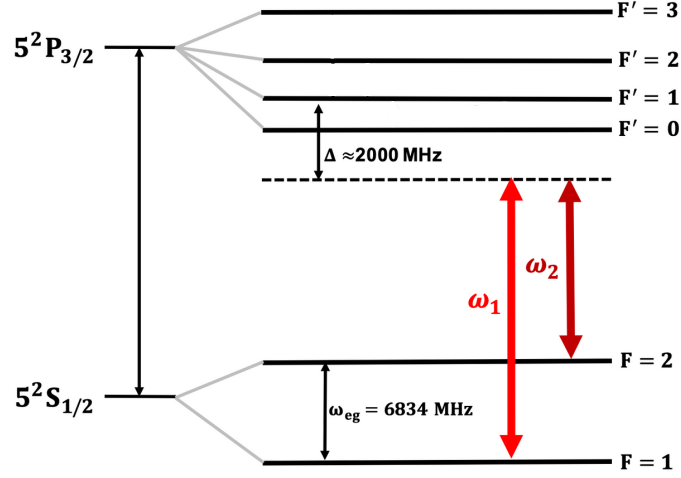


Figure 2.5: Energy level scheme of the  $^{87}\text{Rb}$  D<sub>2</sub> line with highlighted levels chosen for Raman transitions. Two-photon Raman transitions are driven between the two ground states  $|5^2\text{S}_{1/2}, F=1\rangle$  and  $|5^2\text{S}_{1/2}, F=2\rangle$  by  $\omega_1$  and  $\omega_2$ . The detuning  $\Delta$  is defined with respect to  $|5^2\text{P}_{1/2}, F'=1\rangle$ ,  $\Delta = 2\text{ GHz}$  is the typical detuning used in this work. Adapted from [77].

The light shift changes the energy of the ground hyperfine states and is often called the AC Stark effect. This leads to a Raman transition which does not exactly satisfy the resonance condition leading to an additional phase shift in the interferometer.

$$\delta\Phi = \frac{\delta_A^{\text{AC}} - \delta_D^{\text{AC}}}{\Omega_{\text{eff}}} \quad (2.32)$$

$\delta_A^{\text{AC}}$  and  $\delta_D^{\text{AC}}$  are the differential light shifts during the opening and closing pulse of the interferometer. The light shift can be cancelled selecting a careful ratio of the two laser intensities  $I_1$  and  $I_2$ . The ratio is given by equation 2.33 as a function of detuning,  $\Delta$ .

$$R = \frac{I_2}{I_1} = \frac{\left( \frac{1}{60(\Delta + \omega_{eg})} + \frac{1}{4(\Delta - \Delta_2 + \omega_{eg})} - \frac{2}{5(\Delta - \Delta_3 + \omega_{eg})} \right) - \left( \frac{5}{12\Delta} + \frac{1}{4(\Delta - \Delta_2)} \right)}{\left( \frac{5}{12(\Delta - \omega_{eg})} + \frac{1}{4(\Delta - \Delta_2 - \omega_{eg})} \right) - \left( \frac{1}{60\Delta} + \frac{1}{4(\Delta - \Delta_2)} + \frac{2}{5(\Delta - \Delta_3)} \right)}. \quad (2.33)$$

The ratio is plotted for variable  $\Delta$ , at  $\Delta = 2$  GHz the light shift vanishes for  $R \approx 2$  providing a starting point for Raman laser operation.

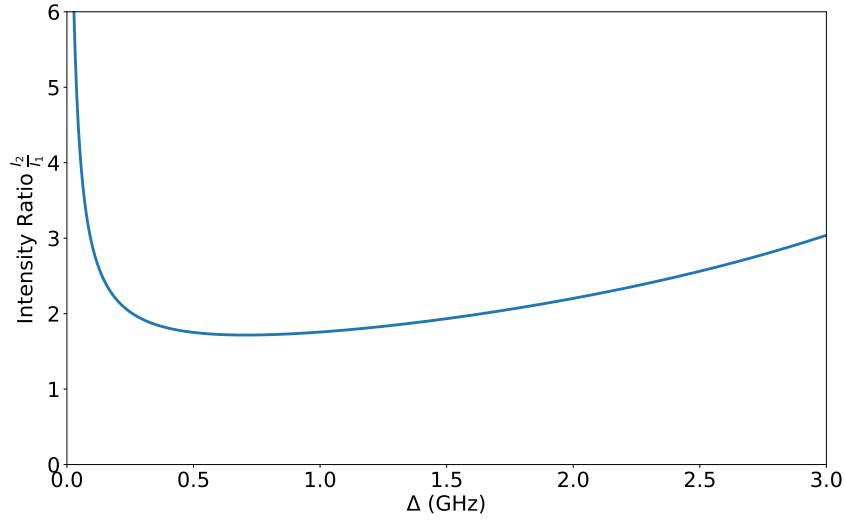


Figure 2.6: Necessary Raman laser intensity ratio for differential AC Stark shift cancellation plotted against detuning  $\Delta$ .

## 2.7 Atom Interferometry

Atoms can be manipulated using light pulses of specific durations. A  $\pi$  pulse with duration  $\tau = \frac{\pi}{\Omega_R}$  (for zero detuning) achieves maximum population inversion whereas a pulse half that length,  $\tau = \frac{\pi}{2\Omega_R}$ , creates an equal superposition of the two states ( $\pi/2$  pulse). A  $\pi$  pulse acts like a mirror, causing state inversion and changing the atom's trajectory. A  $\pi/2$  pulse acts as a

beam splitter. By using different pulses in an atom interferometer, the probability of finding an atom in the excited state at the output can be determined by equation 2.34.  $C$  is the oscillation amplitude (contrast), centred around an offset of  $P_0$ . Figure 2.7 visualises this sequence for atoms without a gravitational acceleration where the trajectories represent classical paths.

$$P_b = P_a - \frac{C}{2} \cos(\delta\phi^{\text{tot}}). \quad (2.34)$$

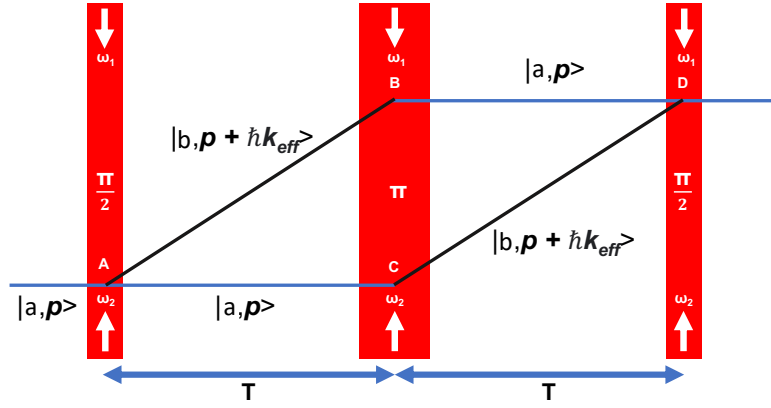


Figure 2.7: Space-time diagram for  $\frac{\pi}{2} - \pi - \frac{\pi}{2}$  interferometry sequence.

A path integral approach can be used to calculate classical paths with only those close to the classically expected trajectories surviving integration [78]. Through construction of two paths, using the classical actions via different midpoints (points B and C in Fig. 2.7), the phase shift between the two arms is computed. Phase contributions from mechanism  $x$  are denoted by  $\delta\phi^x = \delta\phi_{\text{path 1}}^x - \delta\phi_{\text{path 2}}^x$ . The total phase has contributions originating from: the propagation of the atom,  $\delta\phi^{\text{prop}}$ , the phase from the atom's internal evo-

lution,  $\delta\phi^{\text{int}}$  and the phase due to the interaction of the laser,  $\delta\phi^{\text{laser}}$ . This leads to a total interferometer phase of

$$\delta\phi^{\text{tot}} = \delta\phi^{\text{prop}} + \delta\phi^{\text{int}} + \delta\phi^{\text{laser}}. \quad (2.35)$$

Since atoms spend equal time in each energy state for both paths the phase contribution from internal evolution is zero. One can also show that the contribution of the phase due to propagation is also zero even in the presence of a gravitational field. This leaves only the phase accumulated due to the atom light interaction,  $\delta\phi^{\text{laser}}$ .

### 2.7.1 Laser Phase

To evaluate phase contributions due to atom light interaction four possible interactions are considered. For the two level case the atom acquires a phase shift when the interaction causes it to change state. The phase shifts due to these interactions are summarised in table 2.2. Additional phase shifts due to light shifts can be considered but are ignored as they can be nulled. The phase difference between two paths can be constructed for the laser interactions by considering paths ABD and ACD. Following the upper path ABD in figure 2.7 the atom changes state in the following manner  $|a\rangle \rightarrow |b\rangle \rightarrow |a\rangle \rightarrow |b\rangle$ . In the lower path (ACD) the state evolves as  $|a\rangle \rightarrow |a\rangle \rightarrow |b\rangle \rightarrow |b\rangle$ . The total accumulated phase can be calculated for each path with table 2.2.

Internal State	Momentum	Phase Shift
$ a\rangle \rightarrow  b\rangle$	$\mathbf{p} \rightarrow \mathbf{p} + \hbar \mathbf{k}_{\text{eff}}$	$+(\mathbf{k}_{\text{eff}} \mathbf{z}(t) - \omega_{\text{eff}} t - \phi_{\text{eff}})$
$ b\rangle \rightarrow  a\rangle$	$\mathbf{p} + \hbar \mathbf{k}_{\text{eff}} \rightarrow \mathbf{p}$	$-(\mathbf{k}_{\text{eff}} \mathbf{z}(t) - \omega_{\text{eff}} t - \phi_{\text{eff}})$
$ a\rangle \rightarrow  a\rangle$	$\mathbf{p} \rightarrow \mathbf{p}$	0
$ b\rangle \rightarrow  b\rangle$	$\mathbf{p} + \hbar \mathbf{k}_{\text{eff}} \rightarrow \mathbf{p} + \hbar \mathbf{k}_{\text{eff}}$	0

Table 2.2: Phase shifts due to atom-light interaction for transitions between ground and excited states. Phase shifts depend on the wavevector,  $\mathbf{k}_{\text{eff}}$ , frequency,  $\omega_{\text{eff}}$ , and phase,  $\phi_{\text{eff}}$ , of the light field. Extra phase contributions from the light shifts are neglected as they can be nulled. Table reproduced from [79].

Equations 2.36a and 2.36b denote the total phase accumulated in paths ABD and ACD respectively.

$$\begin{aligned} \phi^{\text{ABD}} &= [\mathbf{k}_{\text{eff}} \mathbf{z}_A - \phi_{\text{I}}] - [\mathbf{k}_{\text{eff}} \mathbf{z}_B - \omega_{\text{eff}} T - \phi_{\text{II}}] \\ &+ [\mathbf{k}_{\text{eff}} \mathbf{z}_D - \omega_{\text{eff}} 2T - \phi_{\text{III}}] = \mathbf{k}_{\text{eff}} (\mathbf{z}_A - \mathbf{z}_B - \mathbf{z}_D) - \omega_{\text{eff}} T - \phi_{\text{I}} + \phi_{\text{II}} - \phi_{\text{III}}. \end{aligned} \quad (2.36a)$$

$$\phi^{\text{ACD}} = 0 + [\mathbf{k}_{\text{eff}} \mathbf{z}_c - \omega_{\text{eff}} T - \phi_{\text{II}}] + 0 = \mathbf{k}_{\text{eff}} \mathbf{z}_c - \omega_{\text{eff}} T - \phi_{\text{II}}. \quad (2.36b)$$

The total phase shift from the laser interaction is the difference between these two paths given by equation 2.37. One can remove the spatially dependent term by constructing an additional parallelogram  $A_0 B_0 C_0 D_0$ . This uses the curved paths atoms take in the presence of gravity introducing  $gT^2$  and applying equations of motion (see appendix of [74]). In summary, the total phase shift in the Mach-Zehnder atom interferometry sequence originates entirely from the laser interaction. For a vertical Raman beam this produces a gravity sensitive interferometer.

$$\begin{aligned}
\delta\phi^{\text{laser}} &= \phi^{\text{ACD}} - \phi^{\text{ABD}} \\
&= k_{\text{eff}}(z_B - z_A + z_C - z_D) + \phi_I - 2\phi_{\text{II}} + \phi_{\text{III}} \\
&= k_{\text{eff}}gT^2 + \phi_I - 2\phi_{\text{II}} + \phi_{\text{III}}.
\end{aligned} \tag{2.37}$$

## 2.8 Interferometer Phase

As shown atom-light interaction provides a total phase given by equation 2.38a where equation 2.38b is the contribution of the  $n^{\text{th}}$  pulse.

$$\Delta\phi = \phi_{\text{P1}} - 2\phi_{\text{P2}} + \phi_{\text{P3}}. \tag{2.38a}$$

$$\phi_{\text{Pn}} = k_{\text{eff}}z(t) - \omega_{\text{n,eff}}t - \phi_{\text{n,eff}}. \tag{2.38b}$$

For a falling cloud the resonant frequency varies over time due to the Doppler shift. Chirping the frequency of one of the beams will keep the transition resonant. The frequency of  $\omega_1$  has a time dependence introduced, becoming  $\omega_1(t) = \omega_1 + 2\pi\alpha t$ , where  $\alpha$  is the chirp rate. This results in the interferometer phase becoming equation 2.39.

$$\Delta\phi = (k_{\text{eff}}g - 2\pi\alpha)T^2 + \phi_I - 2\phi_{\text{II}} + \phi_{\text{III}}. \tag{2.39}$$

Assuming no systematic effects phase components from the light cancel,  $\phi_I - 2\phi_{\text{II}} + \phi_{\text{III}} = 0$  giving equation 2.40.



$$\Delta\phi = (k_{\text{eff}}g - 2\pi\alpha)T^2. \quad (2.40)$$

When  $k_{\text{eff}}g = 2\pi\alpha$ , the phase shift is cancelled for all  $T$ . Local gravity is then determined by identifying the stationary point where fringes of variable  $T$  have the same local minima.

## 2.9 Phase Noise

The pulse based nature of atom interferometry is advantageous as atoms interact with the Raman beams for only short periods  $\tau$  within a time of approximately  $2T$ . Consequently, the contribution of phase noise to an interferometer is highly frequency-dependent. Phase noise at frequencies much greater than  $\frac{1}{\tau}$  average out within one pulse. Similarly, low frequencies have little contribution too, as the change in phase is minimal if the fluctuation period is large compared with  $2T$ . For intermediate frequencies the phase relation of the atoms to the light field that is established by the first  $\frac{\pi}{2}$  will be affected and any noise will create an unwanted offset to  $\phi_B$  and  $\phi_C$  that cannot be compensated with post-correction. To understand this band pass behaviour of the interferometer the transfer function for Raman laser phase noise must be derived. This provides the mathematical basis for noise analysis [75, 80–82].

### 2.9.1 Raman Laser Phase Noise

If an infinitesimal step in Raman laser phase  $\delta\phi$  happens at time  $t$  during the interferometer sequence a resulting change in transition probability  $\delta P(\delta\phi, t)$  will occur. We then define the sensitivity function  $g_s$  as in equation 2.41.

$$g_s(t) = 2 \lim_{\delta\phi \rightarrow 0} \frac{\delta P(\delta\phi, t)}{\delta\phi}. \quad (2.41)$$

Consider operating the atom interferometer at mid-fringe for maximum sensitivity to phase fluctuations giving an interferometer phase of  $\Phi = \frac{\pi}{2}$ . With a small phase jump  $\delta\phi$ , the transition probability is:

$$P(\delta\phi, t) = \frac{1 - \cos(\frac{\pi}{2} \pm \delta\Phi(\delta\phi, t))}{2} \approx \frac{1 \pm \delta\Phi(\delta\phi, t)}{2}. \quad (2.42)$$

After substituting the above equation into the sensitivity function, the sensitivity function becomes equation 2.43.

$$g_s(t) = \lim_{\delta\phi \rightarrow 0} \frac{\delta\Phi(\delta\phi, t)}{\delta\phi}. \quad (2.43)$$

The sensitivity function for the complete interferometer sequence is given as in equation 2.44 and plotted in figure 2.8.

$$g_s(t) = \begin{cases} \sin(\Omega_R(t + T)) & -T - 2\tau < t < -T - \tau \\ -1 & -T - \tau < t < -\tau \\ \sin(\Omega_R(t + T)) & -\tau < t < \tau \\ 1 & \tau < t < T + \tau \\ \sin(\Omega_R(t - T)) & T + \tau < t < T + 2\tau \\ 0 & \text{else} \end{cases} \quad (2.44)$$

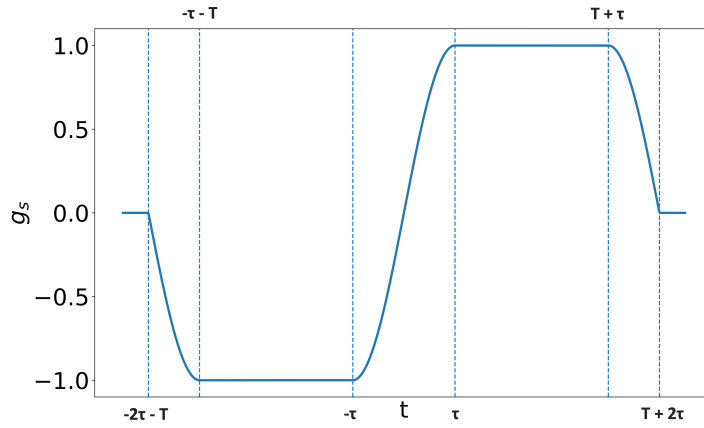


Figure 2.8: Sensitivity function  $g_s(t)$  as a function of the instant phase jump of the Raman laser.

We can now compute the effect of any phase evolution  $\phi(t)$  on total interferometer phase  $\Phi$  via this sensitivity function.

$$\delta\Phi = \int g_s(t) d\phi(t) = \int g_s(t) \frac{d\phi(t)}{dt} dt. \quad (2.45)$$

However, in practice, it is much easier to measure the phase noise in the frequency domain. Let  $S_\omega$  and  $S_\phi$  be the power spectral densities (PSD) of the phase noise of the Raman laser, expressed in terms of frequency and phase. The variance of the corresponding interferometry phase noise is then written as:

$$\begin{aligned}\sigma_\phi^2 &= \int_0^{+\infty} |G(\omega)|^2 S_\omega d\omega \\ &= \int_0^{+\infty} |\omega G(\omega)|^2 S_\phi d\omega = \int_0^{+\infty} |H(\omega)|^2 S_\phi d\omega.\end{aligned}\tag{2.46}$$

where  $G(\omega)$  is the Fourier transform of the sensitivity function  $g_s(t)$ .  $H(\omega)$  is defined as a weighting function, which is expressed as:

$$\begin{aligned}H(\omega) &= \int_{-\infty}^{+\infty} e^{-i\omega t} g(t) dt \\ &= \frac{4i\omega\Omega_r}{\omega^2 - \Omega_R^2} \sin\left(\frac{\omega(T+2\tau)}{2}\right) \left(\cos\left(\frac{\omega(T+2\tau)}{2}\right) + \frac{\Omega_r}{\omega} \sin\left(\frac{\omega T}{2}\right)\right).\end{aligned}\tag{2.47}$$

This function acts as a band pass filter with oscillating behaviour of period  $T + 2\tau$ . By tuning  $T$  and  $\tau$  the interferometer's transfer function can be tuned to reduce the impact of Raman laser phase noise on overall precision. For example, going to short  $T$  decreases the sensitivity to low-frequency noise at the expense of overall precision. The transfer function exhibits low-pass filtering at high frequencies with a cut-off frequency,  $f_c = \sqrt{3}\Omega_R/6\pi = \sqrt{3}/(12\tau)$ . Longer Raman pulses reduce the contribution of phase noise at high frequencies but are highly velocity selective reducing atom participation in the interferometer and thus signal-to-noise ratio. Naturally, a compromise be-

tween atom number, cloud temperature, laser power and Raman laser phase noise is desirable.

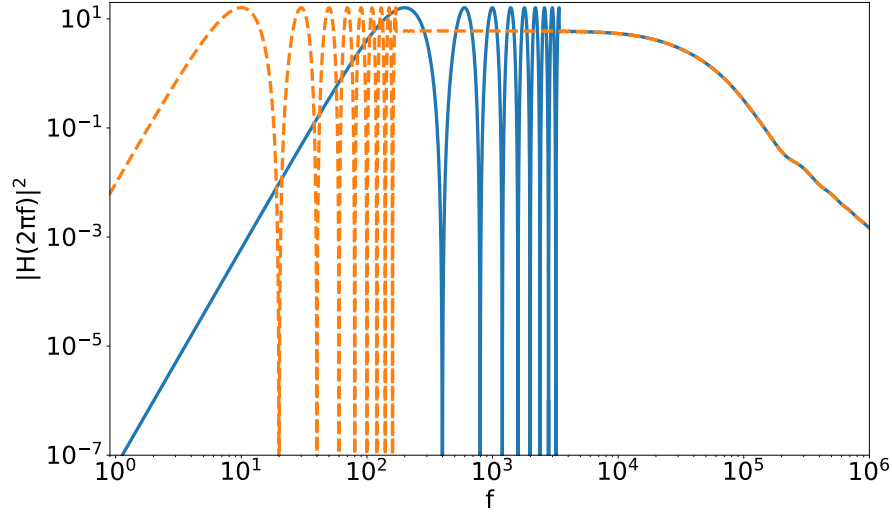


Figure 2.9: Double logarithmic plot of  $|H(\omega)|^2$  for  $\tau = 5 \mu\text{s}$ ,  $T$ : 2.5 ms (blue solid), 50 ms (orange dashed). Averaging is performed after 8 oscillations due to highly oscillatory behaviour.

### 2.9.2 Vibrational Noise

Raman atom optics are generated with a retro reflection geometry. Therefore, any mechanical noise on the optical components prior to entering the chamber is common to all Raman beams. Consequently, the phase difference between the Raman beams is defined by mirror position. To calculate the sensitivity function caused by mirror vibrations, an infinitesimal displacement  $\delta z$  on the bottom mirror is considered, resulting in a change in the phase of the beam on the back reflection path.

$$\delta\phi = 2k_i\delta z \approx k_{\text{eff}}\delta z. \quad (2.48)$$

We can therefore replace the power spectral density of phase fluctuations  $S_\phi$  by the power spectral density induced by vibrations as

$$S_\phi(\omega) = |k_{\text{eff}}|^2 S_z(\omega) = \frac{|k_{\text{eff}}|^2 S_a(\omega)}{\omega^4}. \quad (2.49)$$

The corresponding interferometry phase noise can be evaluated by

$$(\sigma_\Phi^{\text{rms}})^2 = \int_0^\infty |H_a(\omega)|^2 S_a d\omega. \quad (2.50)$$

with the resulting acceleration noise transfer function

$$|H_a(\omega)|^2 = \frac{|H_\phi(\omega)|^2 \cdot |k_{\text{eff}}|^2}{\omega^4}. \quad (2.51)$$

$$\sigma_\Phi^{\text{rms}} = \sqrt{\int_0^\infty |H_\phi(\omega)|^2 \frac{k_{\text{eff}}^2}{\omega^4} S_a(\omega) d\omega}. \quad (2.52)$$

As can be observed from figure 2.10 this transfer function behaves like a low-pass filter with the interferometer phase most sensitive to frequency vibrations below 10 Hz. Note also the increased sensitivity to vibrational noise for larger T time.

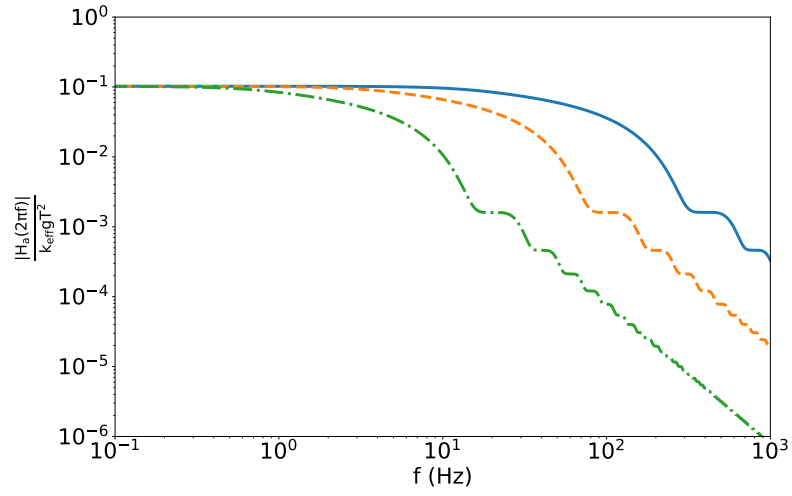


Figure 2.10: Double logarithmic plot of  $\left| \frac{H_a(2\pi f)}{k_{\text{eff}} g T^2} \right|$ ,  $\tau = 5 \mu\text{s}$  and  $\lambda = 780.2 \text{ nm}$ . Function is calculated for  $T$ : 2.5 ms (blue solid), 10.0 ms (orange dashed) and 50.0 ms (green dashdot). A moving averaging is performed on the data to smooth out anti-resonance features.

## Chapter 3

# Laser Cooling and Trapping

Atom interferometry relies on creating a dense atomic sample known as a magneto-optical trap (MOT). Generating a MOT has two important components: optical molasses cooling, which reduces the velocity spread of the atom cloud and trapping, which uses the Zeeman effect to confine the atoms spatially [83–88]. This chapter presents a short background on MOT theory which is then applied to help understand operation in a high-bandwidth context.

### 3.1 Laser Cooling

When an atom absorbs a photon, it will recoil in the opposite direction due to momentum conservation. This principle of laser cooling is illustrated in Figure 3.1, for an atom travelling toward the right beam with velocity  $v_z$



this laser is seen as Doppler shifted onto resonance. Consequently, the atom experiences greater photon scattering from this beam and is slowed down. For travelling in the opposite sense the atom is also slowed. This concept extends to 3D slowing atoms travelling in any direction.

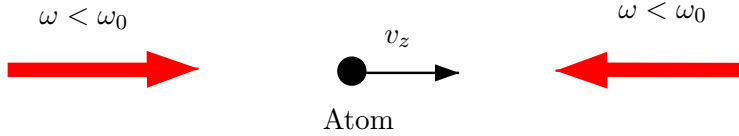


Figure 3.1: Two counter-propagating laser beams of frequency  $\omega$  less than the atomic resonance frequency  $\omega_0$  illustrating 1D optical molasses.

The scattering rate, described by equation (3.1), is highly influenced by the detuning of the light from resonance [89]. This equation can be divided into two terms, where the force equals the momentum impulse from a single photon multiplied by the scattering rate. The parameters involved are  $\Gamma$ , the natural linewidth of the transition,  $s$ , the saturation parameter and  $\delta$ , the detuning from resonance.

$$F_{\text{scatt}} = \hbar k \left( \frac{\Gamma}{2} \frac{s}{1 + s + (\frac{2\delta}{\Gamma})^2} \right). \quad (3.1)$$

In the low velocity limit ( $k v \ll \Gamma$ ) the force imbalance between the beams can be expressed as in equation 3.2, where  $v$  is the atomic velocity.

$$\begin{aligned}
 F_{\text{molasses}} &= F_{\text{scatt}}(\omega - \omega_0 - kv) - F_{\text{scatt}}(\omega - \omega_0 + kv) \\
 &\simeq F_{\text{scatt}}(\omega - \omega_0) - kv \frac{\partial F}{\partial \omega} - \left[ F_{\text{scatt}}(\omega - \omega_0) + kv \frac{\partial F}{\partial \omega} \right] \\
 &\simeq -2 \frac{\partial F}{\partial \omega}
 \end{aligned} \tag{3.2}$$

The optical molasses force can then be expressed as

$$F_{\text{molasses}} = -\alpha v. \tag{3.3a}$$

$$\alpha = 2k \frac{\partial F}{\partial \omega} = -8\hbar k^2 s \frac{\frac{\delta}{\Gamma}}{[1 + (\frac{2\delta}{\Gamma})^2]^2}. \tag{3.3b}$$

Equation (3.3a) shows that the light force always opposes atomic motion, damping it. This effect is thus called optical molasses. Cooling reduces the velocity spread of an ensemble, while slowing decreases its mean velocity without compression. However, cooling has a limit due to fluctuations caused by spontaneously-emitted photons and also due to the statistics associated with photon absorption. This induces random walks in velocity space and imposes a temperature constraint known as the Doppler cooling limit ( $T_D$ ).

$$k_B T_D = \frac{\hbar \Gamma}{2}. \tag{3.4}$$

The Doppler limit is determined by the natural linewidth of the cooling transition. For the  $^{87}\text{Rb}$   $D_2$  line,  $T_D = 140 \mu\text{K}$ . However, early experiments achieved lower temperatures, revealing that the two-level model of

the atom was insufficient. Seminal work demonstrated sub-Doppler cooling processes enabled by the spatially varying light shift of the atom [90]. For  $^{87}\text{Rb}$ , the recoil limit is  $T_r = 360 \text{ nK}$ , with temperatures as low as  $2 \text{ }\mu\text{K}$  being achieved [91, 92]. While optical molasses cools atoms, it does not trap them. To accomplish trapping, the force in equation 3.2 needs spatial dependence.

## 3.2 Trapping

To trap atoms a magnetic field gradient is applied over the region where cooling beams overlap. This is generated with anti-Helmholtz coils for which the current in each coil travels in the opposite sense. This relies on the Zeeman effect which shifts the  $m = \pm 1$  sublevels of the atom proportional to its distance from the trap centre. By using  $\sigma^+ - \sigma^-$  polarisations for the beams a trap can be created. This can be illustrated by considering an atom at  $z > 0$  such that the  $\Delta M_J = -1$  transition is closer to resonance (fig. 3.2). The selection rules result in preferential absorption of photons exciting the  $\sigma^-$  transition which generates a restoring force on the atom towards  $z = 0$ . Similarly one can see that for an atom at  $z < 0$  a similar restoring force is generated. Extending this configuration to 3D creates an atomic cloud at the magnetic null.

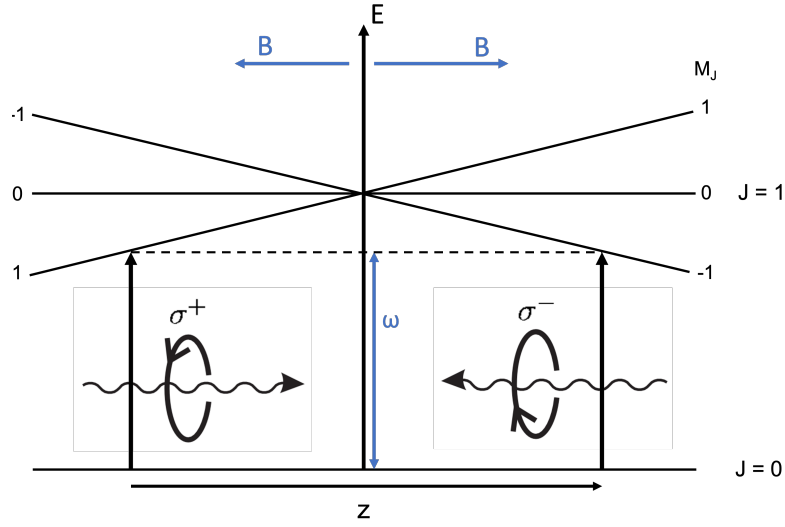


Figure 3.2: Underlying trapping mechanism of a MOT shown for a  $J = 0 \rightarrow J = 1$  transition. The Zeeman splitting of the sub-levels is spatially dependent. Counter-propagating beams of circularly-polarised light coupled with the selection rules create spatial confinement.

The Zeeman effect is incorporated into equation 3.2 giving the detuning spatial dependence.

$$\delta_{\pm} = \delta \mp \vec{k} \cdot \vec{v} \pm \mu' B / \hbar. \quad (3.5)$$

$\mu' = (g_e M_e - g_g M_g) \mu_B$  is the effective magnetic moment for the transition and  $\delta = \omega - \omega_0$ . The  $\pm$  subscript accounts for the different detunings of the right and left directed beams in figure 3.1 with the dot product included for completeness in 3D. Considering only small Doppler and Zeeman shifts the expression for the MOT restoring force is expanded to obtain equation 3.6a,  $A = \frac{dB}{dz}$  and is the magnetic field gradient.

$$F_{\text{MOT}} = -2 \frac{\partial F}{\partial \omega} (kv + \beta z) = -\alpha v - \frac{\alpha \beta}{k} z. \quad (3.6a)$$

$$\beta = \frac{\mu'}{\hbar} A. \quad (3.6b)$$

The functional form of equation 3.6a is identical to a damped simple harmonic oscillator and so atoms undergo oscillations (under-damped motion) or travel smoothly toward the MOT centre (over-damped motion). Fig. 3.3 demonstrates the MOT restoring force acting on individual  $^{87}\text{Rb}$  atoms with different initial velocities. For clarity, this work concerns the  $^{87}\text{Rb}$   $D_2$  ( $5^2S_{1/2} \rightarrow 5^2P_{3/2}$ ) transition for which  $\Gamma = 2\pi \times 6.065(9)$  MHz and  $\lambda = 780.241$  nm.

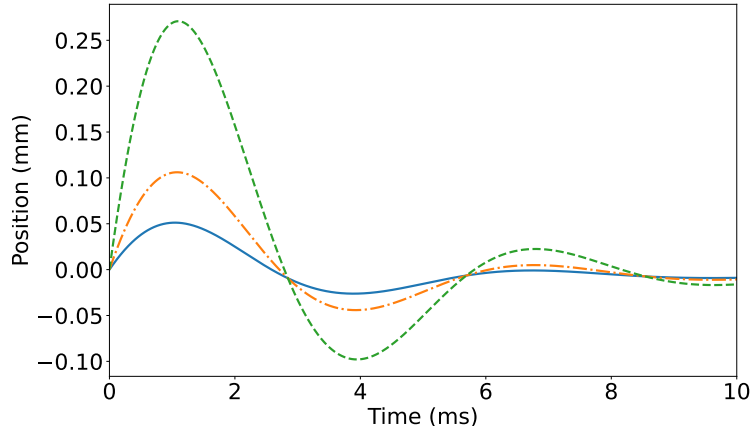


Figure 3.3: Numerical simulation of atomic trajectories for  $^{87}\text{Rb}$  atoms in a magneto-optical trap for variable initial velocities illustrating under-damped motion occurring for  $s = 1$ ,  $\Delta = -3$ ,  $A = 16$  G/cm. Initial velocity  $v_0$  ( $\text{ms}^{-1}$ ): 0.5 (green dashed), 0.2 (orange dash-dotted), 0.1 (blue solid).

The simplified low velocity model was useful for understanding cooling and trapping, but had limitations for simulation purposes. To overcome these the unapproximated force was numerically integrated. By substituting the

detunings for  $\delta_{\pm}$  (equation 3.5), the complete force equation is shown in equation 3.7.

$$F_{\text{MOT}} = F_{\text{scatt}}(\delta_+) - F_{\text{scatt}}(\delta_-) = \hbar k \frac{\Gamma}{2} \left[ \frac{s}{1 + s + (\frac{2\delta_+}{\Gamma})^2} - \frac{s}{1 + s + (\frac{2\delta_-}{\Gamma})^2} \right]. \quad (3.7)$$

### 3.3 Capture Velocity

Capture velocity ( $C_v$ ) is an important parameter determining atom number in Eq. (3.14) [93,94]. Consider an atom starting at the trap edge and incrementing its initial velocity from  $0 \text{ ms}^{-1}$  until trapping criteria are no longer satisfied (final position  $|x_f| < 0.1 \text{ mm}$  from the trap centre and final speed  $|v_f| < \sigma_{v \text{ Doppler}}$ ). The atom can also never leave the trap radius during a simulation. The highest velocity for which these conditions are met is the capture velocity. Atoms with velocities less than the capture velocity become part of the MOT whereas those with greater velocities remain uncaptured as part of the background vapour pressure. Fig. 3.4b replicates work for  $^{23}\text{Na}$  providing confidence in modelling with  $^{87}\text{Rb}$  [85,95]. A crude estimate for  $C_v$  is obtained considering the work done in slowing an atom as in Eq. (3.8):

$$C_v \simeq \sqrt{\frac{4F_{\text{max}}\sigma_r}{m}}. \quad (3.8)$$

where  $m$  is the particle mass,  $\sigma_r$  is the trap radius and  $F_{\max}$  is the maximum scattering force ( $\hbar k \Gamma / 2$ ). Choosing appropriate values for the  $^{87}\text{Rb}$   $D_2$  line with  $\sigma_r = 5 \text{ mm}$  gives  $C_v \approx 50 \text{ ms}^{-1}$ . This approach assumes a constant maximum scattering force whereas in reality it carries velocity dependence. Assuming  $\Delta = -3$  in the range of  $0 - 30 \text{ ms}^{-1}$  the mean force is  $\sim F_{\max}/3$ . Accounting for this makes  $C_v \sim 30 \text{ ms}^{-1}$ . Figure 3.5 highlights the effect of power and detuning on capture velocity, additional power shifts the peak to greater detunings compensating for the larger Doppler shifts experienced by faster atoms enabling them to be captured.

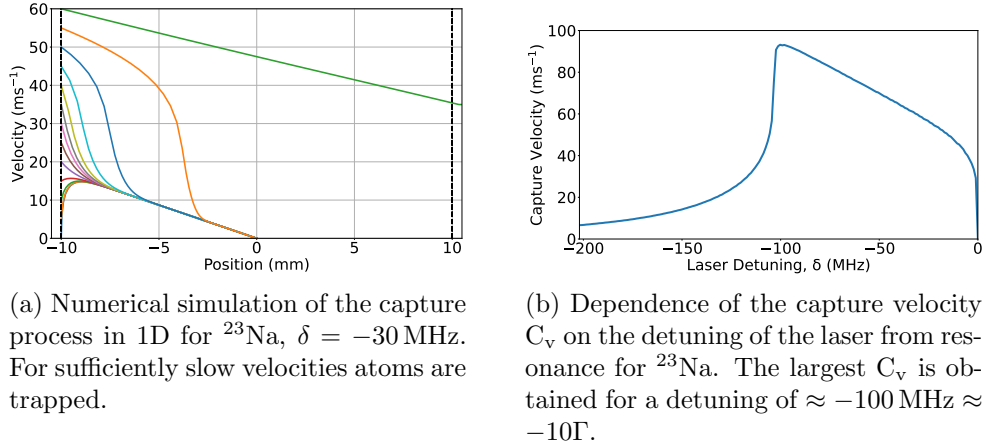


Figure 3.4: Atoms move toward the MOT centre for variable initial velocities,  $s = 10$  [95].

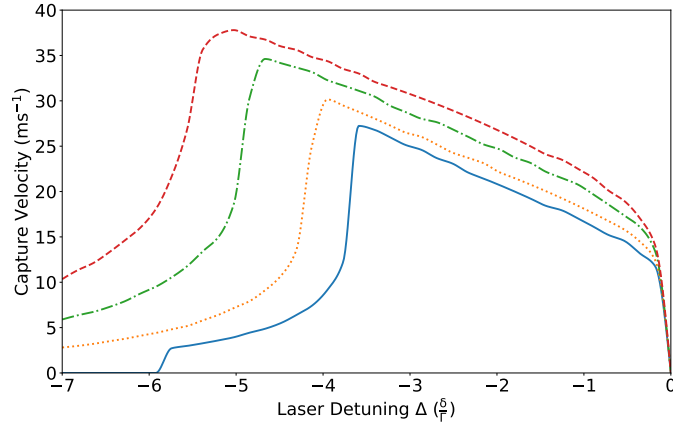


Figure 3.5: Capture velocity dependence on laser detuning and intensity for  $^{87}\text{Rb}$ .  $A = 16 \text{ G/cm}$ ,  $\sigma_r = 5 \text{ mm}$ ,  $s$ : 1 (blue solid), 2 (orange dotted), 5 (green dash-dot), 10 (red dashed). Simulation time = 100 ms.

Fig. 3.6 shows  $C_v$  detuning scans for variable simulation time. As the simulation time increases there is more time to slow higher velocity atoms meaning the peak shifts to greater detunings. Eventually the peak value remains fixed for increasing simulation time with the drop off in  $C_v$  becoming less extreme.

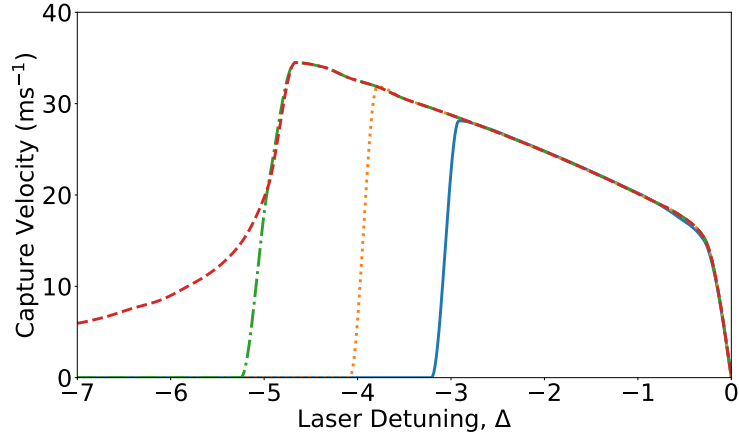


Figure 3.6: Dependence of capture velocity on simulation time for  $^{87}\text{Rb}$ .  $A = 16 \text{ G/cm}$ ,  $\sigma_r = 5 \text{ mm}$ ,  $s = 5$ , Simulation time (ms) 3 (blue solid), 5 (orange dotted), 10 (green dash-dot), 30 (red dashed).



### 3.3.1 Trap Diameter

Capture velocity scales with trap radius and so we explore scalings at low and high beam diameter [96, 97]. For  $d < 2$  mm  $C_v \propto d$  implying the MOT atom number scales  $N \propto d^6$ . For  $d > 3$  mm,  $C_v \propto d^{0.4}$  implying  $N \propto d^{3.6}$ . As identified in figure 3.7 the 1D capture velocity simulation successfully reproduces these scalings. By finding the intersection between the fits for the low and high regimes one can determine the diameter at which the transition between regimes occurs. For the two detuning values ( $\Delta = -2, -3$ ) simulated in [98] the simulation agrees well (within 0.1 mm).

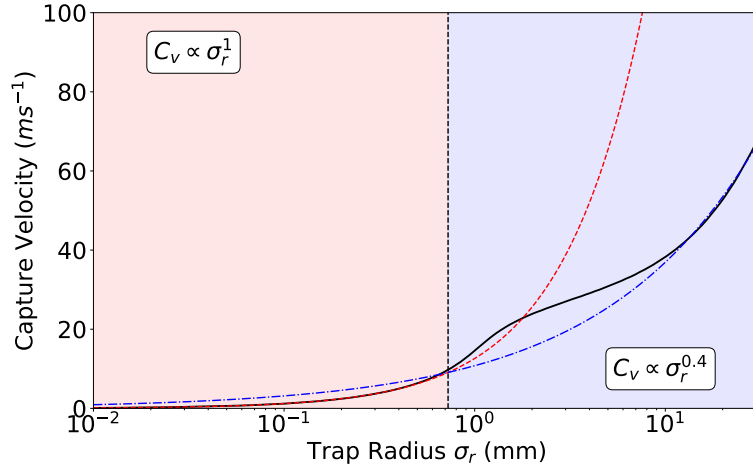


Figure 3.7: Capture velocity against beam diameter for  $^{87}\text{Rb}$  comparing simulation result (black) with predicted scalings at low ( $\propto \sigma_r$ , blue dot-dashed) and high ( $\propto \sigma_r^{0.4}$ , red dashed) trap radii. Transition between two regimes occurs at  $\sigma_r \sim 0.8$  mm (vertical black dotted line).

### 3.3.2 Finite Power

Atom number scales rapidly with trap size, but for finite power maximising beam radius is undesirable due to insufficient light intensity for atom capture. Therefore, for a fixed cooling power and beam radius,  $\sigma_r$  a certain saturation parameter,  $s$  is defined [97]. Using this framework, atom number is optimised for a fixed cooling power of 180 mW (figure 3.8). To quantify atom number the capture velocity simulation is run with fixed total power for variable beam radii. Dynamics are simulated for 3 ms to reflect high-bandwidth operation. For large beam radii the laser power is insufficient causing atom number to drop to zero. The analysis extends to variable power, showing a rapid increase in atom number ( $< 10$  mW) benefiting from the  $N \propto d^6$  scaling. These simulations inform beam size and power criteria for target atom numbers. For high capture velocity, an optimal parameter regime is found to be  $\Delta \sim -3$ ,  $A \sim 16$  G/cm and a Gaussian beam radius ( $1/e^2$ ) of 10 mm which can support the target intensity,  $s = 5 \sim 10$  mW/cm<sup>2</sup>.

$$P_{\text{SINGLE BEAM}} = \frac{P_{\text{TOTAL}}}{6}. \quad (3.9a)$$

$$I_{\text{SINGLE BEAM}} = \frac{P_{\text{SINGLE BEAM}}}{\pi \sigma_r^2} \quad (3.9b)$$

$$s = \frac{I_{\text{SINGLE BEAM}}}{I_{\text{SAT}}} \quad (3.9c)$$

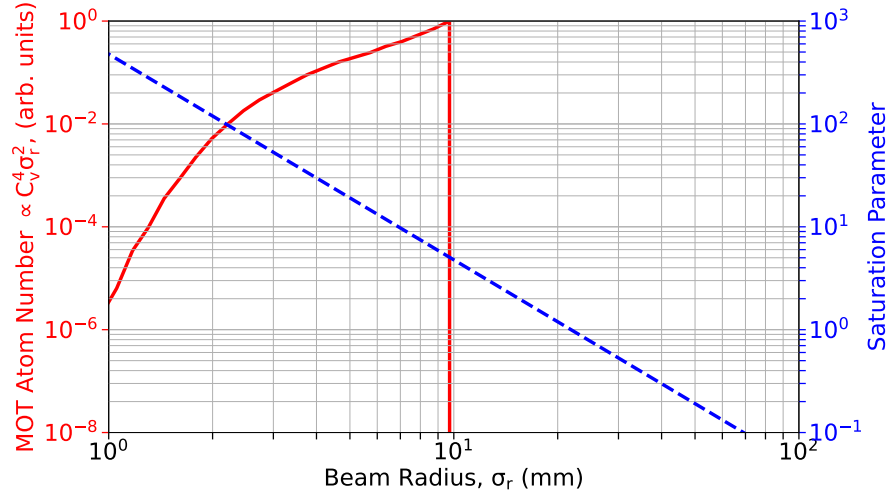


Figure 3.8: Finite power optimisation,  $P_{\text{TOTAL}} = 180$  mW,  $I_{\text{SAT}} = 2\text{mW}/\text{cm}^2$ ,  $A = 16$  G/cm,  $\Delta = -3$ .

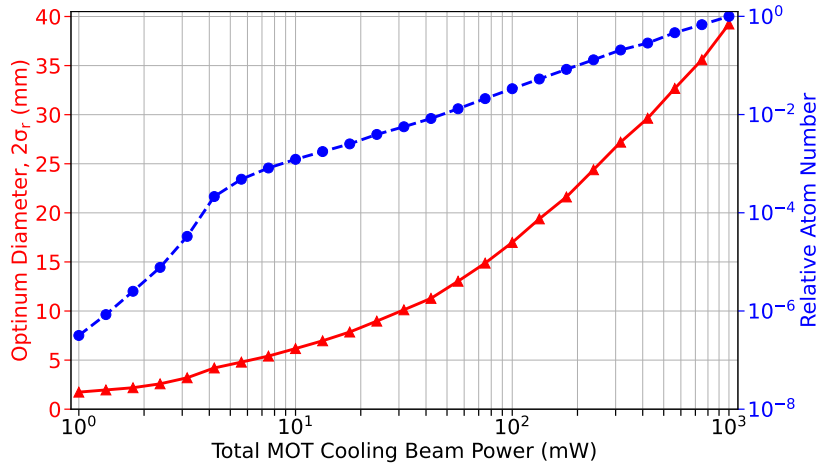


Figure 3.9: Beam radius optimisation for variable  $P_{\text{TOTAL}}$ ,  $I_{\text{SAT}} = 2\text{mW}/\text{cm}^2$ ,  $A = 16$  G/cm,  $\Delta = -3$ .

### 3.4 High Bandwidth Operation

*The contents of this section form part of a PRA paper submission*

*“Magneto-optical trap performance for high-bandwidth applications”*

For modelling purposes, the simulation cycle is divided into two distinct phases: the drop phase and the recapture phase. In applications with lower bandwidth requirements, the loading time for a magneto-optical trap (MOT) is less strict. Therefore, after dropping atoms loading from the background vapour is employed. The timescale for this loading process depends on pressure and typically takes a few hundred milliseconds. Consequently, efficient recapture of atoms between cycles becomes crucial for high bandwidth operation. Although the recapture efficiency is not 100%, the atom number does not decay to zero as atoms are also loaded from the background vapour during recapture. Two main factors hinder recapture: the finite restoring force of the MOT and collisions between atoms in the MOT and the background vapour.

#### 3.4.1 Intensity Dependence

During freefall atoms move primarily along the vertical and so trajectories are modelled in 1D. For high bandwidth applications the drop time ( $T_d$ ) will be  $\sim 5$  ms leading to an atom falling  $\frac{1}{2}gT_d^2 = 0.13$  mm. Given a typical trap radius of  $\sim 5$  mm an atom will not fall far from the trap centre. However,

despite this short distance the recapture time is still finite and limited by the restoring force towards the MOT centre. Fig. 3.10 shows a numerical simulation of single atom trajectories over multiple cycles highlighting that for insufficient power the restoring force will be too weak and the atom will not be recaptured, this can be seen in the loss of periodicity for the  $s = 1$  trajectory.

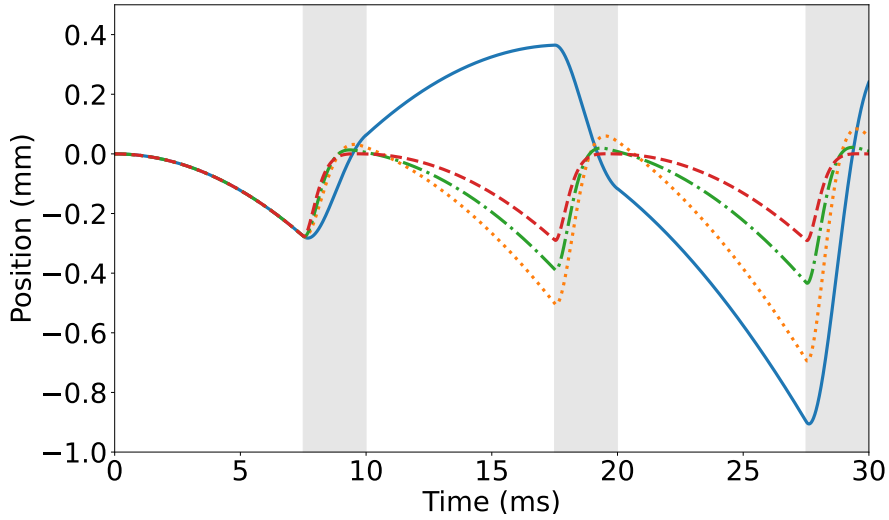


Figure 3.10: Numerical simulation of single atom trajectories in a 100 Hz HBW  $^{87}\text{Rb}$  MOT for variable saturation parameter.  $S = 1$  (blue solid), 3 (yellow dotted), 5 (green dash-dotted) and 10 (red dashed).  $\Delta = -3$ , duty cycle = 0.75,  $A = 16$  G/cm. The white and grey regions correspond to the free fall and the recapture phases respectively.

The dynamics of an atomic cloud are explored by simulating 1000 atoms with numerical trajectories similar to those in Fig. 3.10. Initial atomic positions and velocities are normally distributed with  $\sigma_{\text{MOT}}$  and  $\sigma_v$  respectively.  $\sigma_{\text{MOT}}$  is the cloud radius and  $\sigma_v = \sqrt{k_B T_{\text{MOT}}/m}$  is the cloud's velocity spread where,  $T_{\text{MOT}}$  is the cloud temperature and  $m$  is the mass of a single atom.

Atoms are considered trapped if their final position is  $|x_f| < 0.1$  mm from the trap centre with a final speed  $|v_f| < \sigma_{v \text{ Doppler}}$ , where  $\sigma_{v \text{ Doppler}} = 0.12 \text{ ms}^{-1}$  is the Doppler velocity [85]. The fraction of atoms satisfying the capture criteria at the end of the cycle is the restored fraction,  $P_{\text{restored}}$ . Unless stated, bandwidth is fixed at 100 Hz giving a cycle length of 10 ms. Increasing duty cycle increases the drop time and reduces the recapture time. When the recapture time is  $< 3$  ms, there is insufficient time to restore atoms to the MOT centre and recapture efficiency declines. The restored fraction tends to a finite value for short recapture times ( $\sim 0.05$ ). This results from the spatial extent of the MOT with respect to the capture region. For short recapture times, a fraction of atoms have not left the capture criteria region and are considered recaptured. The simple model assumes a Gaussian intensity profile in a 1D trap. Higher temperatures and longer drop times displace atoms from the intense trapping region, weakening restoring forces. Therefore, low temperature is crucial for cold-atom experiments, aiding recapture and bandwidth.

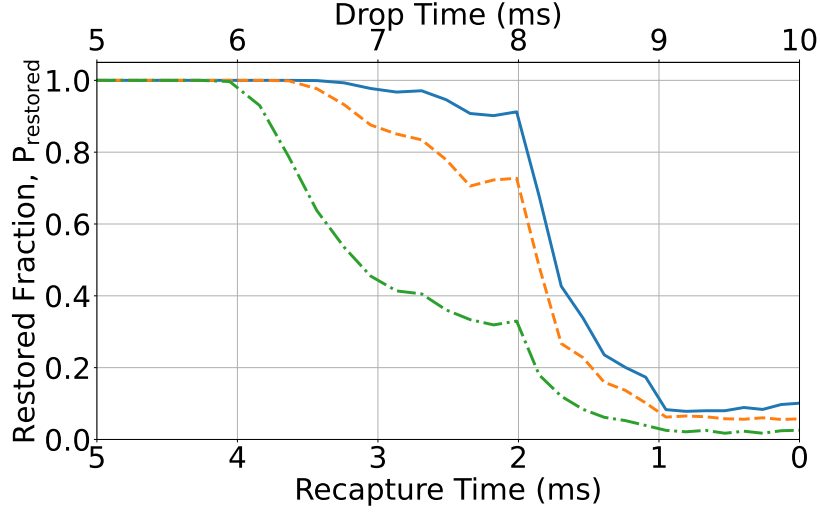


Figure 3.11: Simulating restored atom fraction for a cloud of  $^{87}\text{Rb}$  atoms in a 100 Hz MOT for variable duty cycle and cloud temperature.  $T_{\text{MOT}}$ : 10  $\mu\text{K}$  (blue solid), 100  $\mu\text{K}$  (orange dashed), 1000  $\mu\text{K}$  (green dash-dot).

### 3.4.2 Pressure Dependence

During an operational cycle, atoms in the cloud can also be lost through collisions with atoms in the background vapour. The probability of this not occurring for an atom during a cycle is given by  $P_{\text{no collision}}$  in Eq. (3.10).  $\tau$  is the mean free collision time and  $T_{\text{cycle}}$  is the time for a complete cycle (drop and recapture) as atoms can be lost from background collisions throughout an entire cycle.

$$P_{\text{no collision}} = e^{-\frac{T_{\text{cycle}}}{\tau}}. \quad (3.10)$$

For recapture times  $> 3$  ms, restoration losses are typically negligible ( $P_{\text{restored}} = 1$ ) and so Eq. (3.10) effectively represents the recaptured atom fraction for

a single shot. Unless stated, MOT parameters are:  $s = 3$ ,  $\Delta = -3$ ,  $A = 14$  G/cm,  $T_{\text{MOT}} = 300$   $\mu\text{K}$ ,  $\sigma_{\text{MOT}} = 0.5$  mm,  $4\sigma_r = 20$  mm ( $1/e^2$ ) diameter, Vapour Pressure =  $2.9 \times 10^{-7}$  mbar,  $R = 4.5 \times 10^9 \text{ s}^{-1}$ ,  $L = 16.0 \text{ s}^{-1}$ ,  $\sigma_0 = 1 \times 10^{-13} \text{ cm}^2$ ,  $C_v = 21 \text{ ms}^{-1}$ . Fig. 3.12 shows the results of computing  $P_{\text{no collision}}$  and the mean free time over the  $10^{-9} - 10^{-6}$  mbar range. For pressures approaching  $10^{-6}$  mbar, the collision timescale is comparable to the cycle time, reducing the recaptured fraction significantly. Note, modelling only considers background collisions with  $^{87}\text{Rb}$  atoms and assumes the absence of other species.

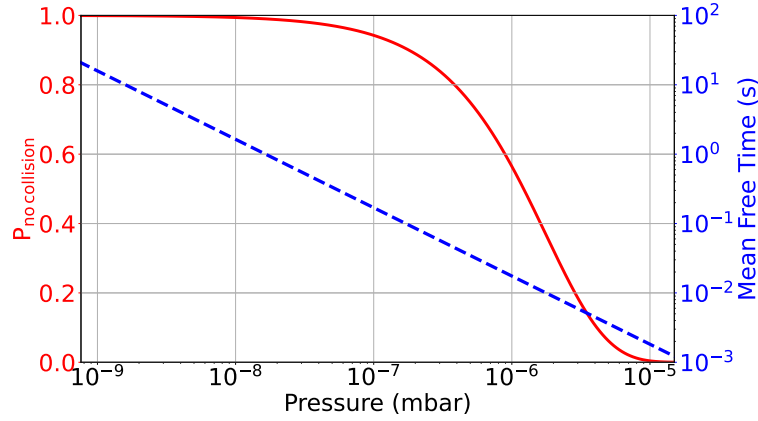


Figure 3.12:  $P_{\text{no collision}}$  (red solid) and mean free time (blue dashed) for variable pressure for  $T_{\text{cycle}} = 10$  ms [99].

### 3.4.3 MOT Loading

The rate of change of atoms in the MOT is given by the balance between loading and loss of atoms, integrating this gives the number of atoms after loading for a period of time,  $t$  in Eq. (3.13a).  $R$  and  $L$  are the loading and



loss rate of the MOT and are given by Eqs. (3.13b) and (3.13c) respectively. The  $C_v^4$  dependence of loading rate originates from the Reif model described in [100]. This model assumes any atom slower than the capture velocity entering the trap volume will be trapped. The captured atomic flux is derived by calculating the number of particles entering the trap region with velocity less than the capture velocity.

$$dN = nf(v)d^3v \cdot v\cos(\theta)dAdt. \quad (3.11)$$

$n$  is the background particle density,  $f(v)$  is the Maxwell–Boltzmann distribution (eq. 3.12),  $v$  is the particle velocity, and  $v \cdot \cos(\theta)$  is the component of the velocity perpendicular to area element  $dA$ . The captured flux is determined by integrating equation 3.11  $v$  from  $0 \rightarrow C_v$ .

$$f(v) = \left( \frac{mv^2}{2k_B T} \right) e^{-\frac{mv^2}{(2k_B T)}}. \quad (3.12)$$

Under normal operating conditions where  $C_v$  is very small compared to the average thermal speed of the background particles, one can approximate  $e^{-\frac{mv^2}{2k_B T}} \approx 1$ . This considerably simplifies the calculation, and the integral gives equation 3.13b.

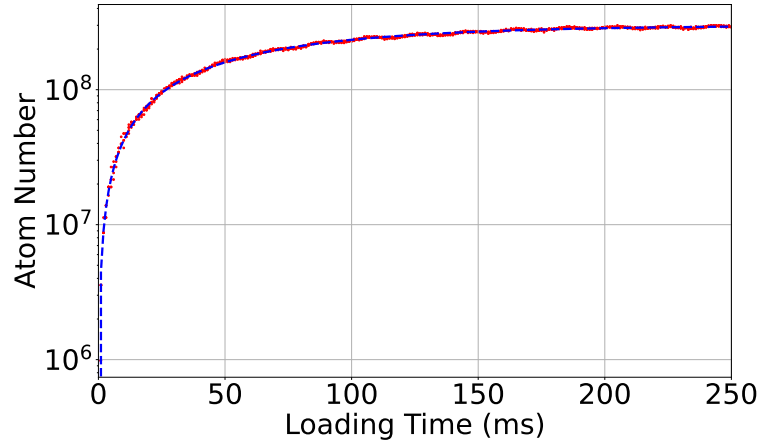


Figure 3.13: Experimental MOT loading data. The following parameters are extracted,  $R = 4.5 \times 10^9 \text{ s}^{-1}$ ,  $L = 16.0 \text{ s}^{-1}$  and a  $^{87}\text{Rb}$  vapour pressure of  $2.9 \times 10^{-7} \text{ mbar}$ .

$A$  is the trap surface area ( $4\pi\sigma_r^2$ ) where  $\sigma_r$  is the trap radius.  $C_v$  is the capture velocity,  $n_b$  is the number density of particles in the background vapour,  $\sigma_0$  is the collision cross section and  $v_{th}$  is the average thermal velocity of the background gas. The number density of the particles is calculated from the ideal gas equation  $n_b = \frac{P}{kT}$  with the vapour pressure obtained from the model in [89].

$$N(t) = \frac{R}{L}(1 - e^{-Lt}). \quad (3.13a)$$

$$R = \frac{2AC_v^4 n_b}{\pi^2 v_{th}^3}. \quad (3.13b)$$

$$L = \frac{1}{\tau} = n_b \sigma_0 v_{th} \quad (3.13c)$$

The rate equation sometimes includes an additional loss for inelastic collisions

between atoms in the MOT. This changes the loss rate to  $L \rightarrow L + \beta \bar{n}$ , where  $\bar{n}$  is the mean cloud density and  $\beta$  is a constant characterising this mechanism. This implies that two-body collisions can be neglected if  $\beta \bar{n} \ll L$ .  $\beta \sim 1 \times 10^{-11} \text{ cm}^3 \text{ s}^{-1}$  has been reported for a laser detuning of  $\delta = -\Gamma$  and an intensity of  $s \approx 10$ , which are fairly typical operating parameters [101]. Assuming a MOT with  $10^8$  atoms with a radius of 1 mm gives a number density of  $\bar{n} \sim 1 \times 10^{10} \text{ cm}^{-3}$ . The typical pressure ( $L \sim 1 - 10 \text{ s}^{-1}$ ) is about 1-2 orders of magnitude higher than the two-body loss term. Hence, neglecting the two-body loss term in the model is justified. For 100 Hz operation the MOT loading time is only a few ms. Even for relatively high pressures in the low  $10^{-7}$  mbar range the loading rate is a few  $10^9/\text{ms}$ . This means at most  $\sim 10^7$  atoms can be loaded from the background vapour after a few ms; a small fraction of the steady state population reached in the experimental data in Fig. 3.13. This highlights how efficient recapture of atoms between cycles is essential for high bandwidth operation. In this regime MOT composition is recapture dominated with a small contribution from background loading. Consider a high bandwidth MOT containing  $10^8$  atoms with a recapture period of  $\sim 1$  ms. Assuming recapture is 90% efficient with a MOT loading rate of  $R \sim 10^{10} \text{ s}^{-1}$  the atom number will remain steady. By considering losses from the finite restoration time and collisions independently, an iterative equation is formed describing the shot to shot atom number.

$$N_{i+1} = N_i P_{\text{no collision}} P_{\text{restored}} + \frac{R}{L} (1 - e^{-LT_{\text{Reload}}}). \quad (3.14)$$

$N_i$  denotes the atom number in the  $i^{\text{th}}$  cycle. The first term describes the contribution from recaptured atoms with  $P_{\text{no collision}} P_{\text{restored}}$  representing the constant shot to shot recapture fraction. The second term describes background loading and is the MOT loading equation with terms as defined in Eq. (3.13a). The time for loading and recapture is given by  $T_{\text{reload}}$ . Iterating until  $N_{i+1} = N_i$  gives the operational steady state atom number for the MOT. For higher pressure the loading rate is larger and so more atoms are loaded from the background but fewer atoms are recaptured due to more background collisions and vice versa for lower pressure. Steady state corresponds to the point at which the number of atoms lost due to inefficient recapture is perfectly balanced by the atoms loaded from the background vapour. In Fig. 3.14 the behaviour of a traditional MOT is simulated and contrasted with a high bandwidth MOT with a duty cycle of 0.65. In this configuration there are about 20% the number of atoms when compared with a MOT fully loaded from background vapour. Even with relatively high pressure ( $2 \times 10^{-7}$  mbar), without recapture it would take 10x longer to load this many atoms. This limits bandwidth to at most 30 Hz showing the importance of recapture in maximising bandwidth.

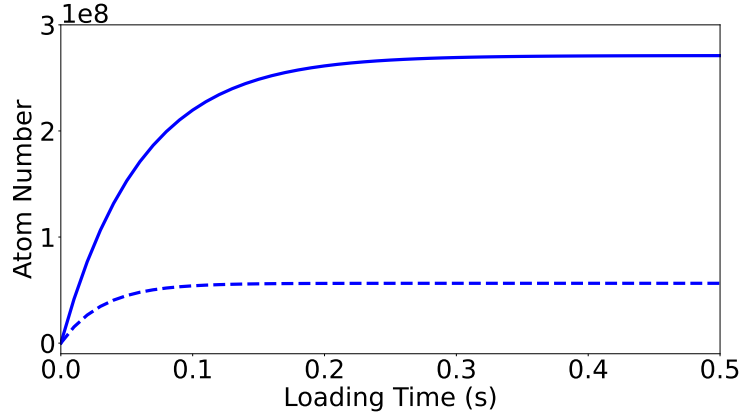


Figure 3.14: Traditional non-dynamic MOT loading (solid), 100 Hz high bandwidth MOT loading simulation at a duty cycle of 0.65 (dashed).

#### 3.4.4 Cloud Expansion

During the measurement period the atomic cloud undergoes free expansion as described by equation 3.15 [102].

$$\sigma_f = \sqrt{\sigma_0^2 + \frac{k_B T}{m} T_{\text{ex}}^2} \quad (3.15)$$

In this equation,  $\sigma_0$  represents the initial radius of the cloud,  $\sigma_f$  is the final radius,  $T$  is the cloud temperature,  $m$  is the mass of a  $^{87}\text{Rb}$  atom and  $T_{\text{ex}}$  corresponds to the free expansion time, which is equivalent to the interrogation time ( $T_i$ ). In a traditional cycle with  $\sigma_0 = 1 \text{ mm}$ ,  $T = 10 \mu\text{K}$  and  $T_{\text{ex}} \sim 150 \text{ ms}$  the cloud expands to  $\sim 5 \text{ mm}$ . In this case, recapture fails as the cloud expands beyond the trapping beams. However, at high bandwidth, the cloud does not have enough time to expand significantly relative to the trap size. Assuming efficient sub-Doppler cooling, for a free expansion

time  $T_{\text{ex}} \sim 10$  ms, the final cloud radius is only 1.05 mm. This justifies 1D modelling, as transverse motion becomes relatively less important. However, for illustration simulations were performed in 3D, considering the Gaussian intensity profiles of the laser beams.

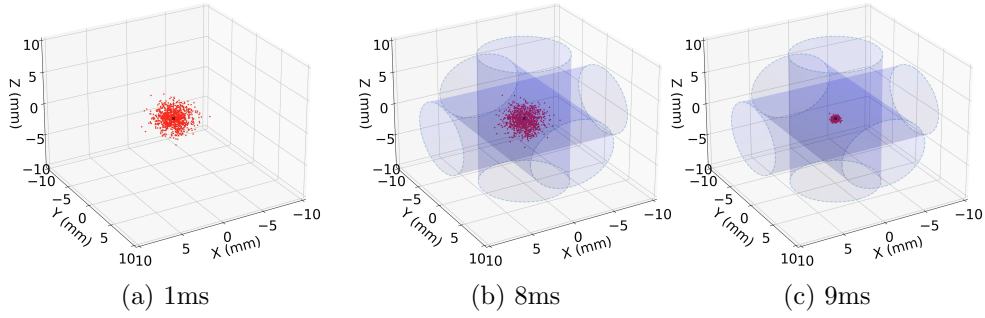


Figure 3.15: 3D dynamics simulation of 1000 atoms for a 100 Hz cycle with a duty cycle of 0.8, trap is switched on at 8 ms.

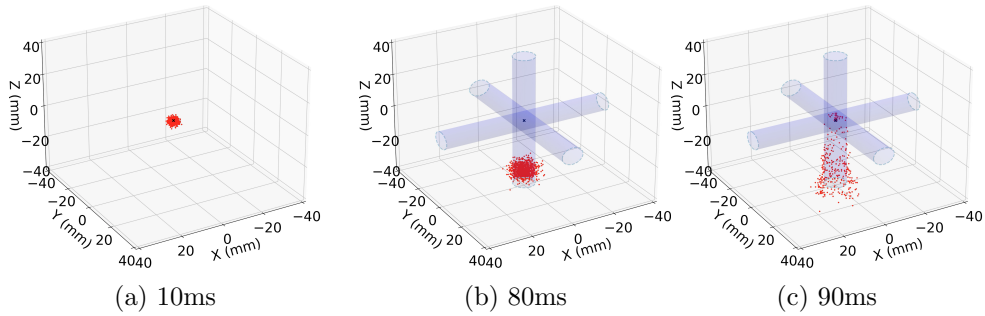


Figure 3.16: 3D dynamics simulation of 1000 atoms for a 10 Hz cycle with a duty cycle of 0.8. Trap is switched on at 80.0 ms, the vast majority of atoms fall outside of trap and cannot be recaptured.

## Chapter 4

# High Bandwidth Atom Interferometry

High-bandwidth atom interferometry is a relatively unexplored parameter space so simulations are performed to identify target parameters and highlight differences with the traditional approach. To ensure well controlled interferometry is performed sufficient separation between optical transitions is required. To consider this magnetic degeneracy due to the Zeeman shift is considered before examining Raman degeneracy associated with cloud temperature and the counter-propagating Raman transition. The chapter then discusses further Raman optimisations and summarises with sensor design specifications.

## 4.1 Zeeman Shift

For zero applied magnetic field hyperfine ground-states have degenerate sub-level structure. These sublevels are called  $m_F$  states and can be separated by applying a magnetic field. For low-fields the energy shift or Zeeman splitting is given by equation 4.1 where  $g_F$  is the Landé g-factor.

$$\Delta E_{|F, m_F\rangle} = \mu_B g_F m_F B_z \quad (4.1)$$

$^{87}\text{Rb}$  has two ground states  $F = 1$  and  $2$  the splitting of each being given by the  $m_F$  number multiplied by  $-0.69\text{MHz G}^{-1}$  and  $0.69\text{MHz G}^{-1}$  respectively [89].

The effect of this splitting is depicted in figure 4.1.

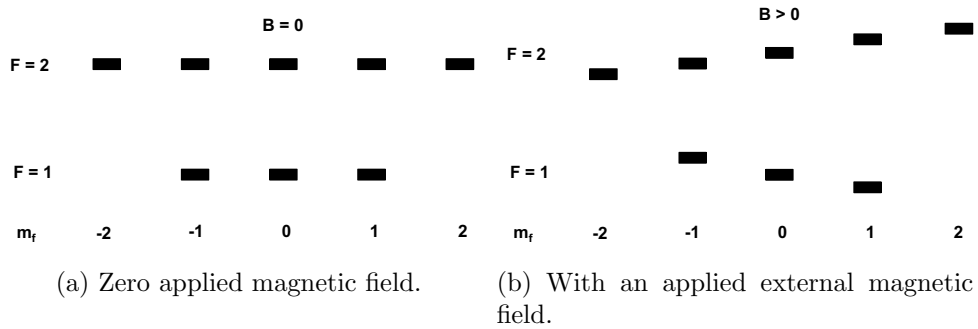


Figure 4.1: Zeeman splitting of the  $m_F$  states in the low field regime.

## 4.2 Raman Degeneracy

The Raman transition requires a bias field for the light polarisation to be defined with respect to the atoms. This is an essential part of the experiment as it enables only the  $|F = 1, m_F = 0\rangle \leftrightarrow |F = 2, m_F = 0\rangle$  transition to



be driven. This transition is chosen for its first order insensitivity to magnetic fields. Without such a bias field transitions will overlap and degrade the interferometer signal. Consequently, the energy spacing of the states must be sufficiently larger than the velocity width of the transitions. In addition, operating in the Doppler-sensitive configuration with a retro-reflecting mirror leads to another degeneracy issue. This occurs due to the Raman resonance condition being satisfied for opposite wave vectors. To resolve this atoms are given an initial velocity causing the two transitions to separate. For low-bandwidth experiments there is enough free-falling time to acquire sufficient velocity for the peaks to separate ( $\sim 20$  ms). However, for high-bandwidth operation this significant dead time limits bandwidth, degrades recapture and increases cloud size. Therefore, moving molasses is adopted to launch the cloud in a few ms. To ensure atomic transitions are not overlapped Raman spectroscopy is usually performed by scanning the Raman laser frequency. This is modelled using equation 2.26 for the transition profile. Three doublet peak pairs are generated with separation given by the bias field strength (equation 4.1) and the doublet separation given by the cloud velocity. Figure 4.2 highlights the large bias needed ( $\sim 4$  G) to sufficiently separate the  $m_F$  states for typical launch velocity, cloud temperature and Rabi frequency. The transitions have Gaussian profiles with width given by equation 4.2. In addition to sufficient bias strength the launch velocity must be large enough to split the doublet peaks. The model is simulated about the central  $m_F = 0$

state suggesting a velocity kick  $\geq 0.2 \text{ ms}^{-1}$  is required.

$$\sigma_{v,\pi,z} = \sqrt{\frac{|\mathbf{k}_{\text{eff}}|^2 \sigma_{v,z}^2 + |\Omega_{\text{eff}}|^2}{|\mathbf{k}_{\text{eff}}|^2}}, \text{ FWHM} = 2\sqrt{2\ln(2)}\sigma_{v,\pi,z}. \quad (4.2)$$

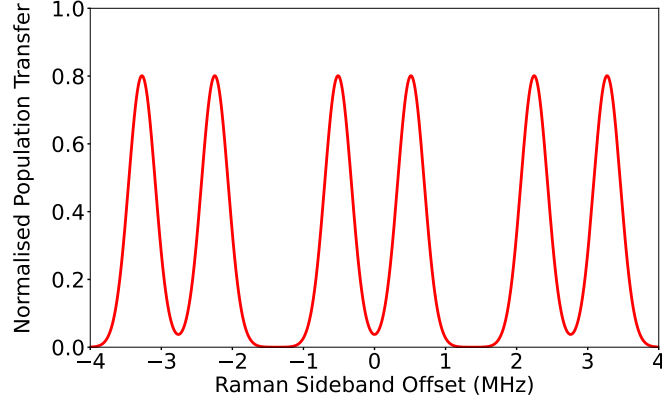


Figure 4.2: Modelling counter-propagating Raman spectroscopy scan, Bias field strength 4G,  $V_{\text{MOM}} = 0.2 \text{ ms}^{-1}$ ,  $\Omega_{\text{eff}} = 2\pi \times 150 \text{ kHz}$ ,  $T = 20 \text{ }\mu\text{K}$ .

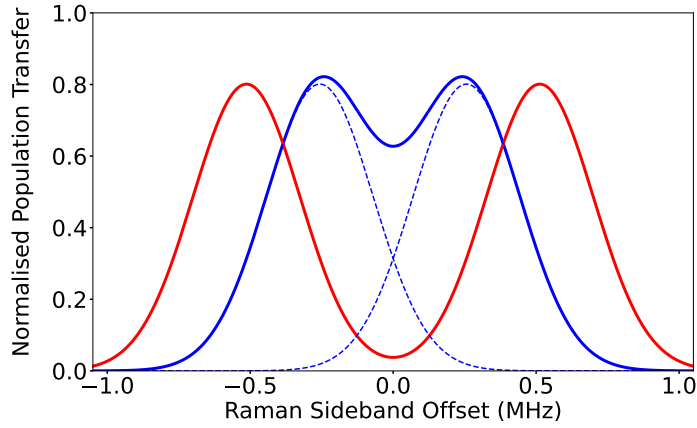


Figure 4.3: Modelling counter-propagating Raman transitions for variable velocity:  $0.1 \text{ ms}^{-1}$  (blue),  $0.2 \text{ ms}^{-1}$  (red). Blue dotted line highlights individual transitions.  $\Omega_{\text{eff}} = 2\pi \times 150 \text{ kHz}$ ,  $T = 20 \text{ }\mu\text{K}$ .

To achieve sufficient peak separation, the launch velocity needs to generate a

Doppler shift matching the transition's full width at half maximum (FWHM), which depends on cloud temperature and Rabi frequency. Figure 4.4 illustrates this optimisation. Higher Rabi frequencies allow for shorter pulses and greater population transfer. However, they also result in a wider Raman transition, requiring a larger velocity kick. The model assumes uncorrelated launch velocity and cloud temperature, but in reality, correlations may exist. Additionally, it assumes that all atoms are in the  $m_f = 0$  state, with no potential overlap with  $m_f = \pm 1$  states.

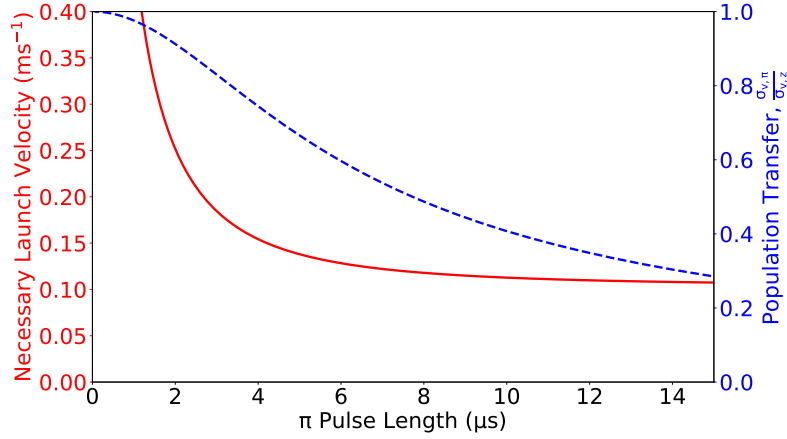


Figure 4.4: Optimising Raman degeneracy for a  $20\text{ }\mu\text{K}$  cloud. Necessary velocity (red solid) to achieve sufficient peak separation and the corresponding population transfer (blue dashed).

Lastly, a downward launch is preferred to avoid applying a pulse to a stationary cloud. This approach means separation increases throughout the interferometer. In contrast, an upward launch can create overlapping peaks as velocity decreases after the initial pulse. Figure 4.5 illustrates this considering Raman spectroscopy at the first and last interferometer pulses for both

launch directions.

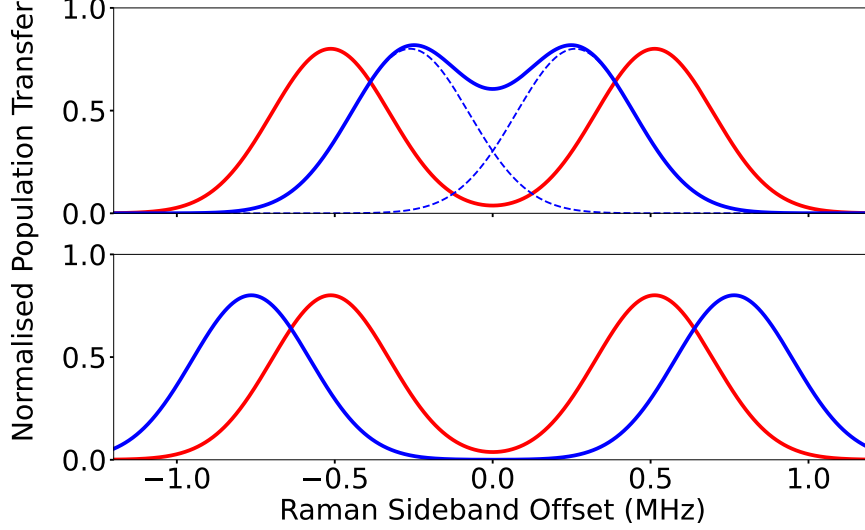


Figure 4.5: Effect of launch direction on Raman degeneracy during interferometry. Simulating  $T = 5$  ms with an initial speed of  $0.2 \text{ ms}^{-1}$ . Spectrum shown at first  $\pi/2$  pulse (red) and final  $\pi/2$  pulse (blue). Upper plot (launching upwards) and lower plot (launching downwards),  $\Omega_{\text{eff}} = 2\pi \times 150 \text{ kHz}$ ,  $T = 20 \mu\text{K}$ .

### 4.3 Moving Molasses

As highlighted breaking Raman degeneracy is reliant on the atoms receiving a velocity kick. The launch velocity is a balance between sufficient frequency separation between peaks while maintaining recapture efficiency and low temperature. Figure 4.6 shows the maximum downward velocity kick that can be applied to a single atom and still achieve recapture for variable recapture times. Increasing the velocity kick will eventually cause the atom to leave the trap and no longer be recaptured. For recapture times of  $1.5 - 2$  ms atoms

with velocities up to  $\sim 0.6 \text{ ms}^{-1}$  can be recaptured for a 5 mm trap radius. Larger beams mean larger kicks can be applied at the expense of a significant power increase.

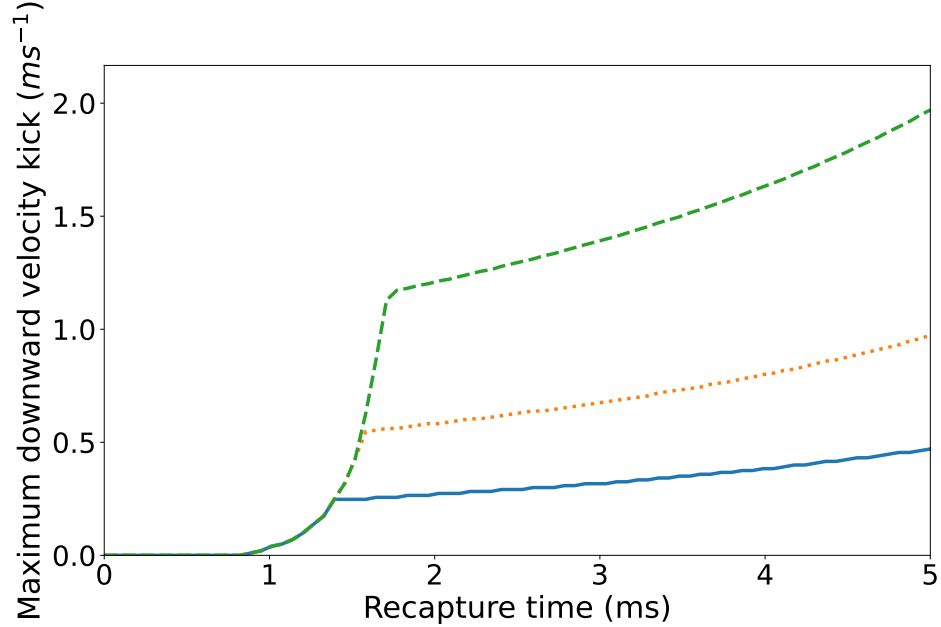


Figure 4.6: Numerical simulation of the maximum downward velocity kick that can be given to a single atom and still achieve recapture for a 100 Hz cycle. The fixed 10ms cycle is split into drop and recapture varying the recapture time. The simulation is performed for various beam radii: 2 mm (solid blue), 5 mm (dotted orange), 10 mm (dashed green).  $s = 10$ ,  $\Delta = -3$ ,  $A = 16 \text{ G/cm}$ .

Before continuing a review of moving molasses is necessary. This technique cools atoms in a reference frame in motion relative to the lab so that they all travel with similar velocities. To achieve this the frequencies of the upward and downward beam are slightly blue and red detuned respectively relative to  $\nu$ . As a result a slow atom is more resonant with the upward than downward beam and is launched vertically. As the atom is launched its velocity

increases becoming more resonant with the downward beam. At a certain velocity the atom resonates equally with both beams and moving molasses is established. The concept is extended to 2D in figure 4.7 cooling in X and Y directions and launching vertically. The angle of the beams means the dot product in the Doppler shift must be considered along with the projection of the force from each laser onto the x and y axes [103,104].

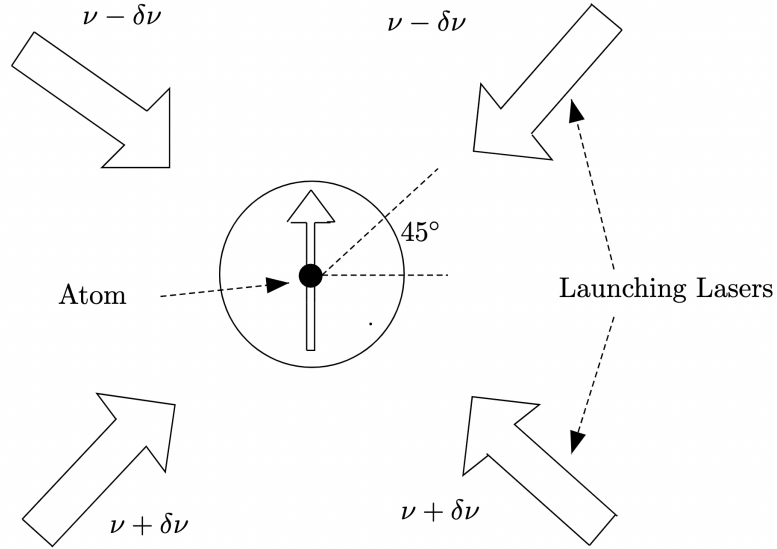


Figure 4.7: 2D moving molasses Geometry.

Figure 4.8 shows an atom trajectory in 2D moving molasses. The final stable molasses velocity ( $v_{MM}$ ) agrees with the predicted value in equation 4.3. For downward launching, the detuning ( $\delta\nu$ ) is negative, with red and blue detuned upward and downward beams, respectively.

$$v_{\text{MM}} = \sqrt{2}\lambda\delta\nu. \quad (4.3)$$

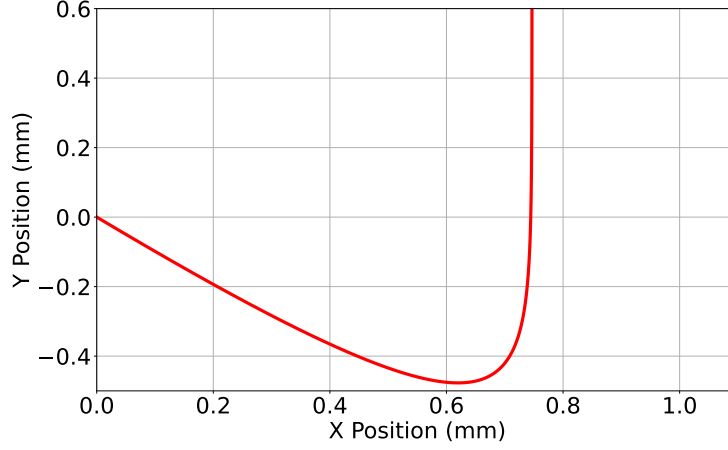


Figure 4.8: Simulation of 2D moving molasses for a  $^{87}\text{Rb}$  atom with initial velocity vector  $[2.5, -2.5] \text{ ms}^{-1}$  for  $s = 5$ ,  $\Delta = -3$ . The simulation is run for 3 ms during which stable molasses is achieved, the final vertical velocity is  $0.5 \text{ ms}^{-1}$ .

#### 4.3.1 Launch Time

To support high-data rate operation atoms must be launched within  $\sim 1\text{-}2$  ms. For this the scattering rate must be maximised which is achieved by high power and small detuning. To explore this the time to reach stable molasses is simulated for variable saturation and detuning; stable molasses is defined as reaching 97% of the target molasses velocity ( $v_{\text{MM}}$ ).

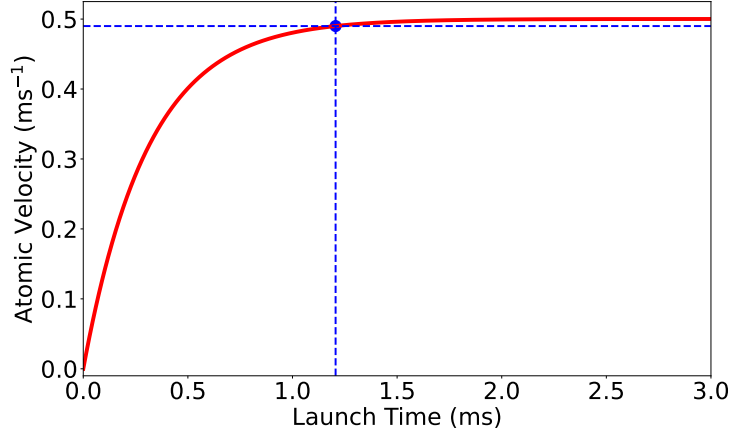


Figure 4.9: 2D moving molasses simulated for a  $^{87}\text{Rb}$  atom initially at rest,  $s = 5$ ,  $\Delta = -3$ . During the 3 ms simulation stable molasses is achieved in 1.2 ms. The blue point and dashed lines indicate  $0.97v_{\text{MM}}$  which arbitrarily defines stable molasses.

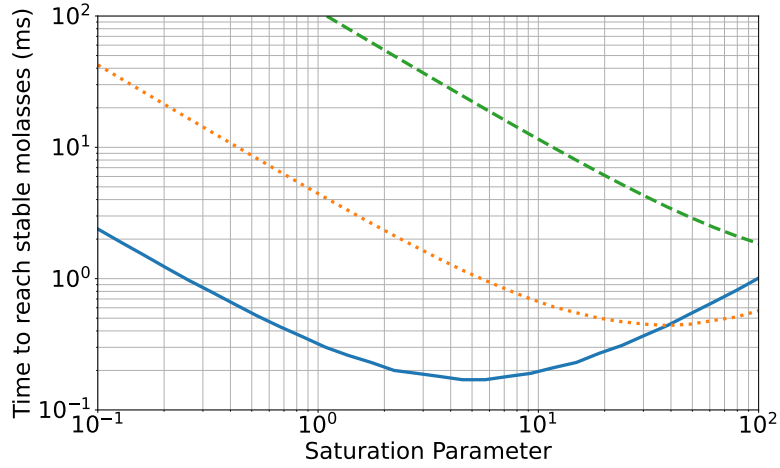


Figure 4.10: Time to establish stable 2D moving molasses for variable saturation ( $s$ ) and detuning. Final velocity achieved is  $0.5 \text{ ms}^{-1}$ , detuning ( $\Delta$ ): -1 (solid blue), -3 (dotted yellow), -9 (dashed green).

However, while molasses is established sub-Doppler cooling is performed reducing the cloud temperature to the  $\sim \mu\text{K}$  level. The cooling conditions compete with those for efficient launching as sub-Doppler cooling is enabled



at low power  $s \ll 1$  and off-resonant detuning  $\Delta \sim -10$ . Consequently, a compromise is reached by ramping laser intensity and frequency enabling favourable conditions for moving molasses initially before transitioning to those suitable for cooling. Note for  $s \gg 1$  power broadening starts to occur increasing the time to reach stable molasses.

### 4.3.2 Launch Direction

Another key consideration is launch direction. If the atoms are not launched vertically then the interaction with the Raman beam will become more inhomogeneous. At worst if the atoms are launched very far off axis then this could also influence recapture. To explore the influence of alignment on single atom trajectories the upper right beam in figure 4.7 is tilted such that the angle with respect to the horizontal becomes  $45^\circ \pm \theta_{\text{misalign}}$ . As a result of this the final velocity reached will no longer be consistent with  $v_{\text{MM}}$ , for example for  $\theta_{\text{misalign}} = 1.0^\circ$  the upper right beam is closer to the vertical and so the vertical force component is overcompensated and the horizontal force component is unbalanced. This reduces the final vertical velocity below expectation and creates motion in the positive  $x$  direction. The converse analysis is true for  $-1.0^\circ$ . Figure 4.11 illustrates this description. To explore this further the angular bias with respect to the vertical is computed for variable beam misalignment.

The alignment precision of our system should be  $\sim 0.2^\circ$  making the bias on the moving molasses around  $\sim 1^\circ$  based on the model in figure 4.12.

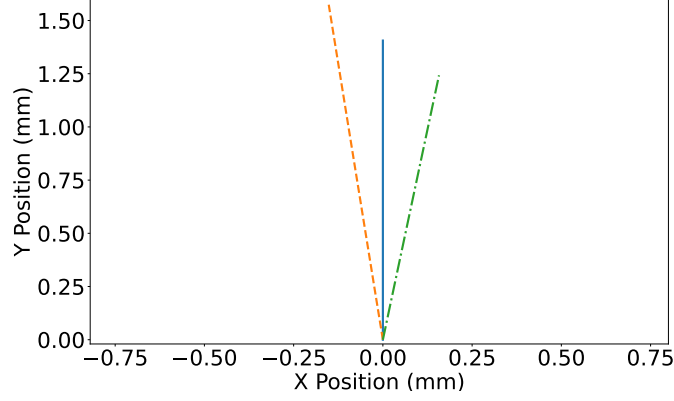


Figure 4.11: Atomic launch bias for variable misalignment angle for 3 ms of moving molasses,  $\theta_{\text{misalign}}^\circ$ :  $0.0^\circ$  (solid blue),  $-1.0^\circ$  (dashed orange),  $1.0^\circ$  (dashed dotted green). Only in the central  $0.0^\circ$  case is the final velocity consistent with  $v_{\text{MM}} = 0.5 \text{ ms}^{-1}$ .

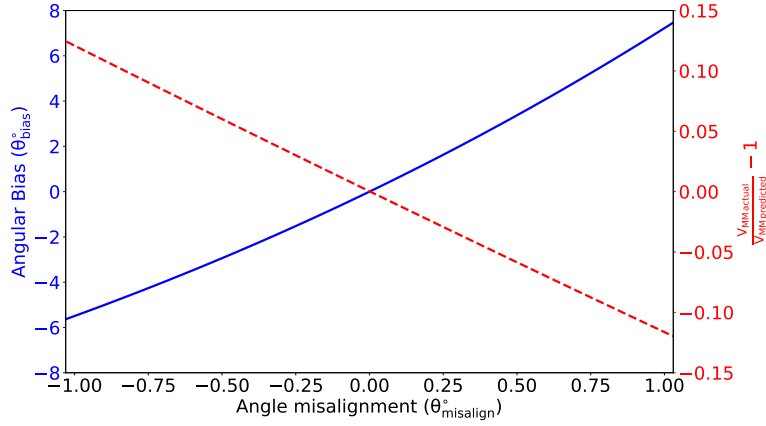


Figure 4.12: Angular launch bias for variable misalignment of upper right beam in moving molasses configuration (blue solid). Percentage change in launch velocity with respect to expected  $v_{\text{MM}}$  for variable misalignment. The target launch velocity is  $0.5 \text{ ms}^{-1}$  with  $s = 10$ ,  $\Delta = -3$ .

The effect of power noise is explored by simulating moving molasses with a cloud of atoms and computing the spread of the vertical velocity component

at the end of launch. Power instability is defined as

$$\sigma_{s,\text{tot}} = \sqrt{\sigma_{s,\text{upper left}}^2 + \sigma_{s,\text{upper right}}^2 + \sigma_{s,\text{bottom left}}^2 + \sigma_{s,\text{bottom right}}^2}. \quad (4.4)$$

Where  $\sigma_{s,\text{tot}}$  is the total power deviation and as an example  $\sigma_{s,\text{upper left}}$  corresponds to the power deviation on the upper left beam in figure 4.7. For modelling purposes the Gaussian noise on each beam is considered equal. Consequently, we define  $\sigma_{s,\text{beam}}$  to be the deviation for an individual beam which implies  $\sigma_{s,\text{tot}} = 2\sigma_{s,\text{beam}}$ . Power noise will introduce variance in the vertical and horizontal velocity components. The angular deviation or spread of the launch bias angles is computed for variable  $\sigma_{s,\text{tot}}$ . Based on the simulation in figure 4.13 and assuming a fairly typical  $\sigma_{s,\text{tot}} = 0.05$  gives an angular deviation of  $\approx 2^\circ$ . For an interferometer time of  $2T = 10\text{ ms}$  the typical total horizontal displacement at the final pulse with respect to first will be  $\sim 0.2\text{ mm}$  which is relatively negligible compared with typical Raman beam radii. Assuming a Raman beam radius of  $5\text{ mm}$  this implies an atom will be significantly off-axis for  $T \sim 150\text{ ms}$ . Consequently, power instability and misalignment should not significantly effect launching at high-data rate operation.

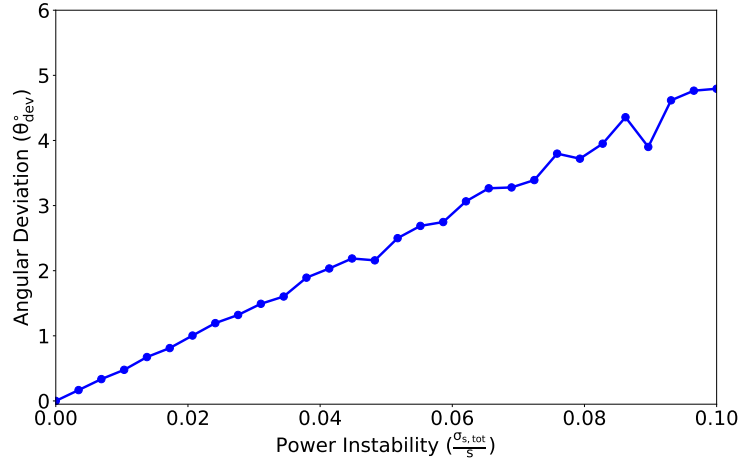


Figure 4.13: Numerical simulation of angular deviation of 500 atoms after 3 ms of moving molasses for variable power noise. Simulation time step is  $10 \mu\text{s}$  modelling the noise on the 100 kHz timescale exclusively. The target launch velocity of  $0.5 \text{ ms}^{-1}$  is achieved within the simulation time,  $s = 10$ ,  $\Delta = -3$ .

## 4.4 Temperature

The temperature of an atomic cloud is determined by two competing processes: cooling forces compressing the momentum distribution and spontaneous scattering forces causing momentum diffusion. When these processes balance each other, the cloud reaches its equilibrium temperature. In the very low velocity regime [105] ( $kv \ll \Gamma$ ), the sub-Doppler cooling force described by Eq. (4.5) becomes prominent. This force arises due to polarisation gradient cooling. The sub-Doppler cooling mechanism in a MOT is traditionally explained based on a Sisyphus effect induced by a spatial modulation of the light shifts of the atomic Zeeman ground sublevels. However, the MOT is generated with  $\sigma^+ - \sigma^-$  polarisation and so this picture is not entirely ac-

curate. The mechanism in this case originates in a slightly different manner, the explanation of which is much more complex and beyond the scope of this work. However, at a macro level, both mechanisms exhibit similar features. The full  $\sigma^+ - \sigma^-$  model presented in [90] is adopted since the linear approximation only applies for  $< 0.01 \frac{\Gamma}{K} = 0.05 \text{ ms}^{-1}$ . For a typical cloud of around  $200 \text{ } \mu\text{K}$ , the velocity is  $0.15 \text{ ms}^{-1}$ , corresponding to  $0.03 \frac{\Gamma}{K}$ . Using the model in Eq. (4.5) would result in overinflated cooling forces for many atoms.

$$F = \left( \frac{120}{17} \frac{\delta\Gamma}{\delta^2 + \Gamma^2/4} \hbar k_L^2 \right) v. \quad (4.5)$$

The force calculation beyond the small velocity range is not covered here in detail, but by solving a set of simultaneous equations the force can be determined. For a more thorough understanding of the model, refer to [90]. The full force profile is showcased in Fig. 4.14, with the inset indicating where the low velocity approximation breaks down and the full model becomes necessary. Fig. 4.15 emphasises the importance of using the full model by plotting the ratio of the full model to the small velocity approximation. It demonstrates the limited range in which the sub-Doppler force operates and its relative strength compared to the Doppler force. Another notable observation is that in Doppler cooling, the capture range is independent of intensity, whereas for the sub-Doppler mechanism, it increases with intensity.

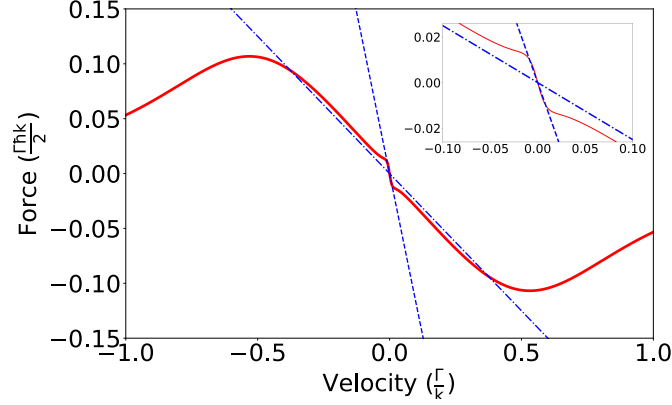


Figure 4.14: Force profile of sub-Doppler cooling in the  $\sigma^+ - \sigma^-$  configuration. The signature slope near  $v = 0$  is associated with polarisation gradient cooling. Full model (red solid line), sub-Doppler linear approximation (blue dashed line) and Doppler linear approximation (blue dashed-dot line).

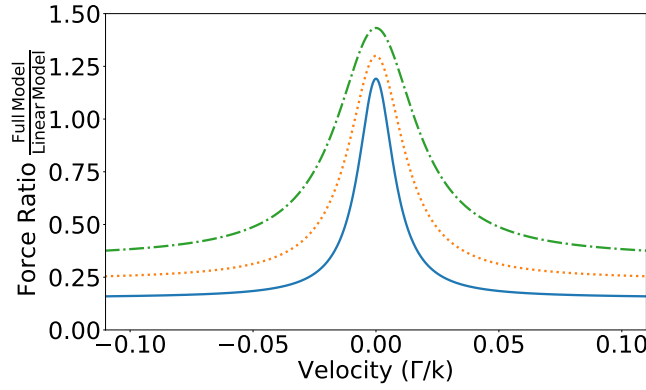


Figure 4.15: Ratio of force from full sub-Doppler cooling model to linear approximation for variable light intensity.  $\delta = -0.5 \Gamma$ ,  $\Omega$ :  $0.2 \Gamma$  (blue solid),  $0.25 \Gamma$  (orange dashed),  $0.3 \Gamma$  (green dashed dot).

A criteria of  $2v_{\text{rec}} \simeq 1 \text{ } \mu\text{K}$  is adopted for completed cooling, using this, the time required to slow down a  $^{87}\text{Rb}$  atom for different detuning and intensities is simulated. In figure 4.16, the cooling mechanism is shown to be rapid, acting on  $100 \text{ } \mu\text{s}$  timescales, although this timescale dramatically increases for off-resonant detuning. In reality, there is also a need to suppress spontaneous

scattering, as otherwise the temperature will be limited.

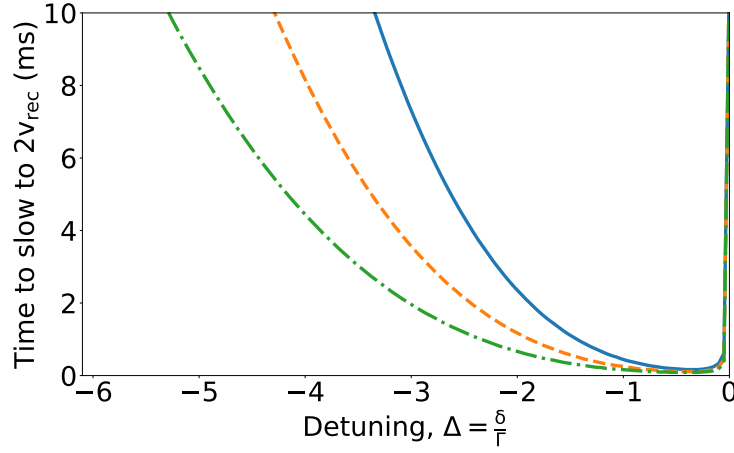


Figure 4.16: Time to slow a  $^{87}\text{Rb}$  atom from  $v_0 = 0.15 \text{ ms}^{-1}$  for variable detuning and light intensity  $\Omega (\Gamma)$ : 0.2 (blue solid), 0.25 (orange dashed), 0.3 (green dashdot).

To provide some temperature modelling the momentum diffusion coefficient  $D_p$  is introduced. Expressions for this coefficient in the  $\sigma^+ - \sigma^-$  configuration are given by equations 4.6a - 4.6d. Equation 4.6d is included to avoid confusion regarding different saturation parameter definitions and to make the detuning dependence explicit. The first term of equation 4.6a corresponds to the fluctuations of the momentum carried away by fluorescence photons. The second term  $D_2$  corresponds to the fluctuations of the difference between the number of photons absorbed in each wave. Increasing the detuning causes both of these terms to decrease, which encourages sweeping the laser frequency away from resonance to achieve lower temperatures. The equilibrium temperature for a cloud of atoms undergoing polarisation gradient cooling is determined by equation 4.7.

$$D_p = D_1 + D_2. \quad (4.6a)$$

$$D_1 = \frac{18}{170} \hbar^2 k^2 \Gamma s_0. \quad (4.6b)$$

$$D_2 = \left[ \frac{36}{17} \frac{1}{1 + (4\delta^2/5\Gamma^2)} \right] \hbar^2 k^2 \Gamma s_0. \quad (4.6c)$$

$$s_0 = \frac{\Omega^2/2}{\delta^2 + (\Gamma^2/4)} \quad (4.6d)$$

$$k_B T = \frac{D_p}{\alpha} = \frac{\hbar \Omega^2}{|\delta|} \left[ \frac{29}{300} + \frac{254}{75} \frac{\Gamma^2/4}{\delta^2 + (\Gamma^2/4)} \right]. \quad (4.7)$$

Figure (4.17) plots the equilibrium temperature using the given equation, for variable laser power and detuning. The plot demonstrates how reducing light intensity and detuning can effectively cool a cloud. Notably, at sufficiently low power levels, the cooling limit approaches the one-photon recoil energy. This behaviour arises from the use of a semi-classical formalism, indicating the need for a more advanced quantum mechanical treatment to address this issue. However, it is worth mentioning that sub-recoil temperatures can be achieved through alternative cooling techniques [106, 107].



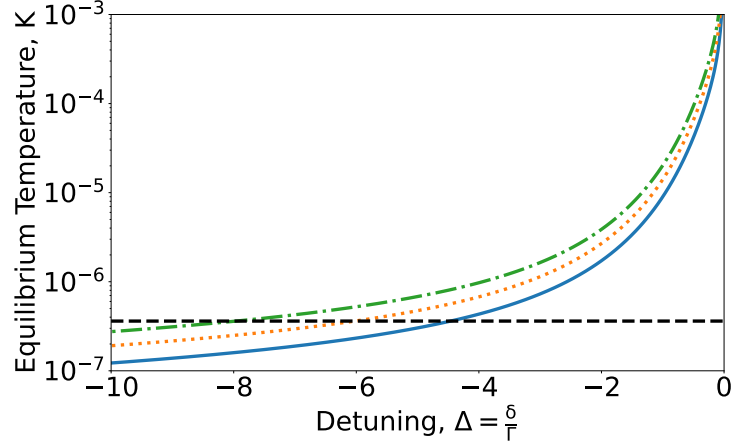


Figure 4.17: Theoretical equilibrium temperature for variable saturation and detuning in the  $\sigma^+ - \sigma^-$  configuration. The dotted line represents the recoil temperature.  $\Omega$ :  $0.2 \Gamma$  (blue solid),  $0.25 \Gamma$  (orange dashed),  $0.3 \Gamma$  (green dashed dot).

## 4.5 Raman Optimisation

Temperature and spatial factors play a crucial role in determining population transfer efficiency. By applying the framework described in section 2.5 the peak population for different cloud temperatures and Rabi frequencies is computed. When the Rabi frequency is higher, the Raman pulse interacts with a broader range of atoms, resulting in substantial transfer even at higher temperatures. Conversely, to achieve efficient transfer with lower power Raman beams,  $\sim \mu\text{K}$  cloud temperatures are required. Figure 4.19 visually presents the conclusion using a contour plot, showing population transfer as a function of pulse length and beam to cloud ratio. Increasing cloud temperature limits the accessible region of high pulse efficiency to short pulses (beam to cloud

ratio  $> 3-5$ ). Furthermore, this analysis assumes sufficient power to achieve arbitrarily short pulses. In reality power is constrained by the performance of optical components. To explore this power optimisation problem the Rabi frequencies must be expressed in practical parameters.

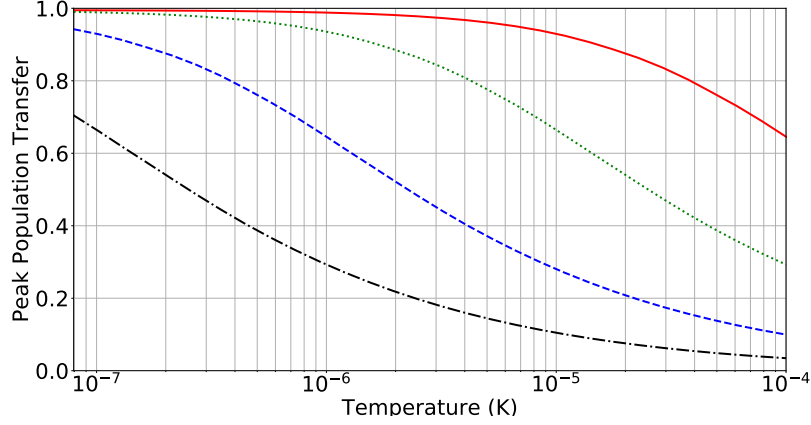


Figure 4.18: Peak population transfer against temperature for variable Rabi frequencies,  $\sigma_{\text{cloud}} = 1$  mm,  $\sigma_{\text{RAMAN}} = 5$  mm. ( $\frac{\Omega_{\text{eff}}}{2\pi}$  kHz): 300 (solid red), 100 (green dotted), 30 (blue dashed), 10 (black dashed dot).

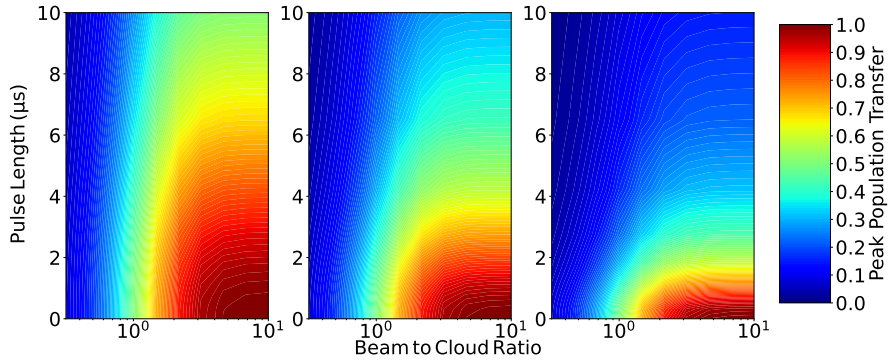


Figure 4.19: Peak population transfer as a function of pulse length and beam to cloud ratio. Temperature (left to right): 5, 20, 100  $\mu\text{K}$ .

The Rabi frequencies are expressed using the Wigner-Eckart theorem (equation 4.8).

$$\Omega_{1,2} = \frac{E_{1,2}}{2\hbar} DG_{1,2} = \sqrt{\frac{I_{1,2}}{2c\epsilon_0\hbar^2}} DG_{1,2}. \quad (4.8)$$

Here  $I_{1,2}$  are the intensities of the corresponding Raman beams,  $c$  is the speed of light,  $\epsilon_0$  is the electric constant,  $D$  the transition dipole matrix element and  $G_{1,2}$  is a geometric factor for the specific transition. This leads to an expression for the effective two-photon Rabi frequency.

$$\Omega_{\text{eff}} = \frac{D^2}{c\epsilon_0\hbar^2} \frac{\sqrt{I_1 I_2}}{\Delta_R} \left| \sum_i G_1 G_2 \right|. \quad (4.9)$$

If the Raman beams have equal polarisations then the sum of the geometric factors for the D<sub>2</sub>-line transition can be written as

$$\left| \sum_i G_1 G_2 \right| = \frac{\sqrt{4 - m_F^2}}{12}. \quad (4.10)$$

Equations 4.9 and 4.10 make it possible to calculate the effective Rabi frequency of the coupling between the  $|F = 1, m_F\rangle = 0$  and  $|F = 2, m_F\rangle = 0$  states when the Raman laser beam intensities and detuning are known. Taking a typical detuning of  $\Delta_R = 2\pi \times 2.0 \text{ GHz}$  and assuming  $I_1 = I_2 = 50 \text{ mWcm}^{-2}$  gives  $\Omega_{\text{eff}} \approx 2\pi \times 45 \text{ kHz}$ .

$$I_{1,2} = \frac{P_{1,2}}{2\pi\sigma_{\text{RAMAN}}^2}. \quad (4.11)$$

To apply these models the total power of the Raman beam is fixed and the

beam radius is varied changing the intensity. To convert power into Rabi frequency the total power is assumed to be equally distributed between both Raman frequencies. Figure 4.20 shows the results of this optimisation for a fixed total power of 250mW, the typical operating power of our Raman laser. For  $\sigma_{\text{RAMAN}} < 1 \text{ mm}$  the beam radius is less than the cloud radius but the Rabi frequency is very spatially inhomogeneous over the cloud and so the transfer is poor. For  $\sigma_{\text{RAMAN}} \gg \sigma_{\text{CLOUD}}$  the Rabi frequency becomes too small for fixed power and the transfer is diminished implying an optimum beam radius of 3-4 mm.

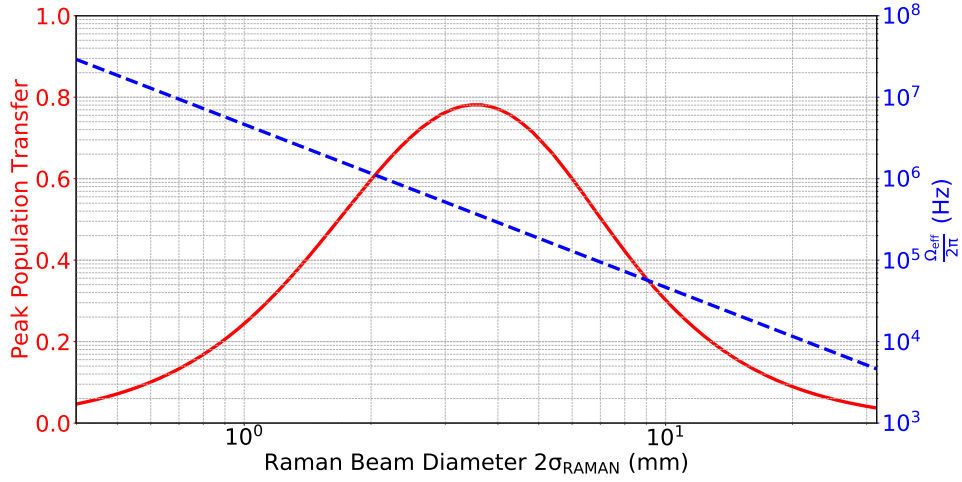


Figure 4.20: Optimising beam radius to maximise population transfer,  $\Delta_R = 2 \text{ GHz}$ ,  $T = 20 \mu\text{K}$ ,  $\sigma_{\text{cloud}} = 1 \text{ mm}$ . A fixed total Raman power of 250mW, peak population transfer (red solid),  $\frac{\Omega_{\text{eff}}}{2\pi}$  (blue dashed).

Figure 4.21 shows performance for variable total power. 1W is about double the absolute upper limit of the Raman laser system limited by the EDFA and frequency doubling crystal. For operating at higher Raman power a sufficient

Rabi frequency can be maintained for larger beams shifting peak performance to larger radii.

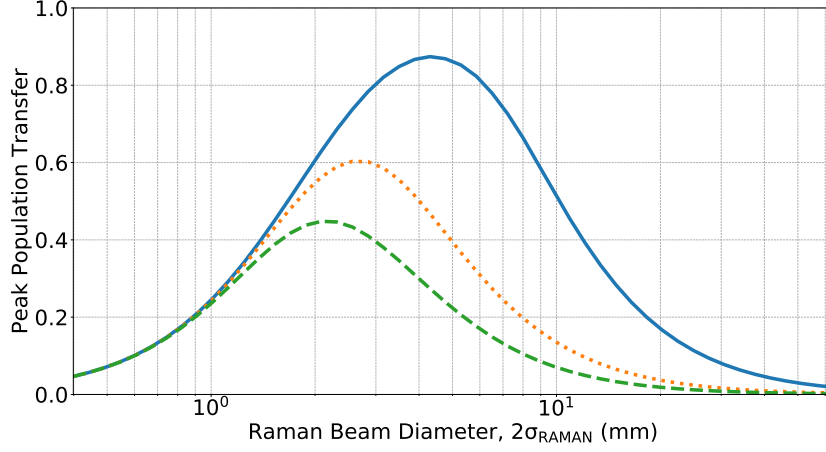


Figure 4.21: Raman beam optimisation for variable total power, 500 mW (blue solid), 100 mW (orange dotted) and 50 mW (green dashed) for  $\Delta = 2$  GHz,  $T = 20$   $\mu$ K,  $\sigma_{\text{cloud}} = 1$  mm.

Overall, using a small, intense Raman beam with a diameter of around 5 mm is preferred to offset higher cloud temperatures and enable optimum atom participation in the interferometer. However, for longer  $T$  times, more Raman power is required to sustain a larger beam and population transfer during the interferometer.

## 4.6 Sensitivity

Before proceeding, we introduce interferometer measurement sensitivity to make performance projections. Sensitivity is given by  $\frac{\delta\phi}{\phi}$ , where  $\delta\phi$  denotes phase noise and  $\phi$  is the phase signal accumulated over the interrogation

period. The noise on a single measurement  $\delta\phi_s$  is limited by quantum projection noise  $N_Q = \sqrt{N_{AI}}$  and  $\delta\phi_s = \eta\delta\phi_Q = \eta\frac{N_Q}{N_{AI}} = \frac{\eta}{\sqrt{N_{AI}}}$ , where  $N_{AI}$  denotes the number of atoms participating in the interferometer with  $\eta \geq 1$  accounting for excessive detection noise.  $F = \frac{1}{(T_i + T_p)}$  defines the operating bandwidth where  $T_i = T_{\text{drop}}$  is the interrogation (drop) time and  $T_p$  is the sensor preparation time incorporating reloading, cooling and detection. Using these definitions sensitivity can be expressed as in Eq. (4.12).

$$S = \frac{4\eta}{k_{eg}\sqrt{N_{AI}}\sqrt{F}T_i^2} \approx 2.5 \times 10^{-8} \frac{\eta}{\sqrt{N_{AI}}} \frac{\sqrt{F^3}}{(1 - FT_p)^2}. \quad (4.12)$$

For optimal sensitivity the duty cycle must be optimised to balance recapture and interrogation periods. Assuming a certain bandwidth, duty cycle and shot noise limited detection the only unknown in Eq. (4.12) is atoms participating in the interferometer,  $N_{AI}$ . To acquire this the recapture simulation is run for the chosen duty cycle and MOT parameters to obtain the recapture efficiency. The MOT number is then computed using Eq. (3.14).  $N_{AI}$  is then computed based on the conservative assumption that  $N_{AI} = 0.01N_{\text{MOT}}$ .

## 4.7 Modelling Summary

Numerical models have proved extremely useful in this project and illuminated potential areas for further development. For example, a complete simulation could be developed to encompass the dynamics of launching, cooling

and recapture. Additionally, 3D dynamics, different detection methods or the simulation of different noise sources could be pursued. Table 4.1 summarises the finalised design parameters extracted from the modelling.

Table 4.1: Design specifications for 100 Hz operation based on numerical modelling.

Parameter	Target	Notes
Cooling Power	$\sim 200$ mW	Assuming $s = 5$ , total for 6 beams
Cooling Detuning	-18 MHz	Assuming $\Delta = -3$
Cooling Diameter	2 cm	Assuming $\sim 200$ mW
Field Gradient	16 G/cm	-
Raman Pulse Length	$\tau_\pi = 3$ $\mu$ s	$\Omega_{\text{eff}} = 2\pi \times 150$ kHz
Raman Power	$\sim 100$ mW	$\Delta_R = -2$ GHz, $\sigma_{\text{RAMAN}} = 3$ mm
Interrogation Time	5 ms	Interrogation time = $2T = 2 \times 2.5$ ms
Recapture Time	2 ms	-
Additional Time	3 ms	Launching, cooling and state preparation
Cloud Temperature	$\sim 20$ $\mu$ K	-
Noise Factor ( $\eta$ )	$< 10$	Preferable to be $< 5$
Sensitivity (S)	$1 \times 10^{-6} \frac{\text{g}}{\sqrt{\text{Hz}}}$	Assumes $\eta = 10$

## Chapter 5

# Experimental Setup

### 5.1 Apparatus

In this chapter the design blueprint for the system is outlined. The system has a “ferris wheel” style construction which must accommodate 8 laser beams. The two vertical beams provide the necessary Raman atom optics with the remaining 6 beams providing light for 3D optical molasses. The two beams through the centre of the “wheel” are connected to coil holders. The entire opto-mechanical structure is built around a  $30 \times 30 \times 100$  mm 780 nm AR-coated glass cell or science chamber which provides various construction flexibilities. The rubidium vapour pressure is supplied by an ampoule as depicted in figure 5.1. The system was prepared by performing a baking process before gently heating the ampoule to increase the vapour pressure to  $2 \times 10^{-7}$  mbar. Controlling pressure with the ampoule proved difficult and



so a switch to a dispenser was made after 1 year of operation. This enabled greater pressure control while sacrificing source longevity.

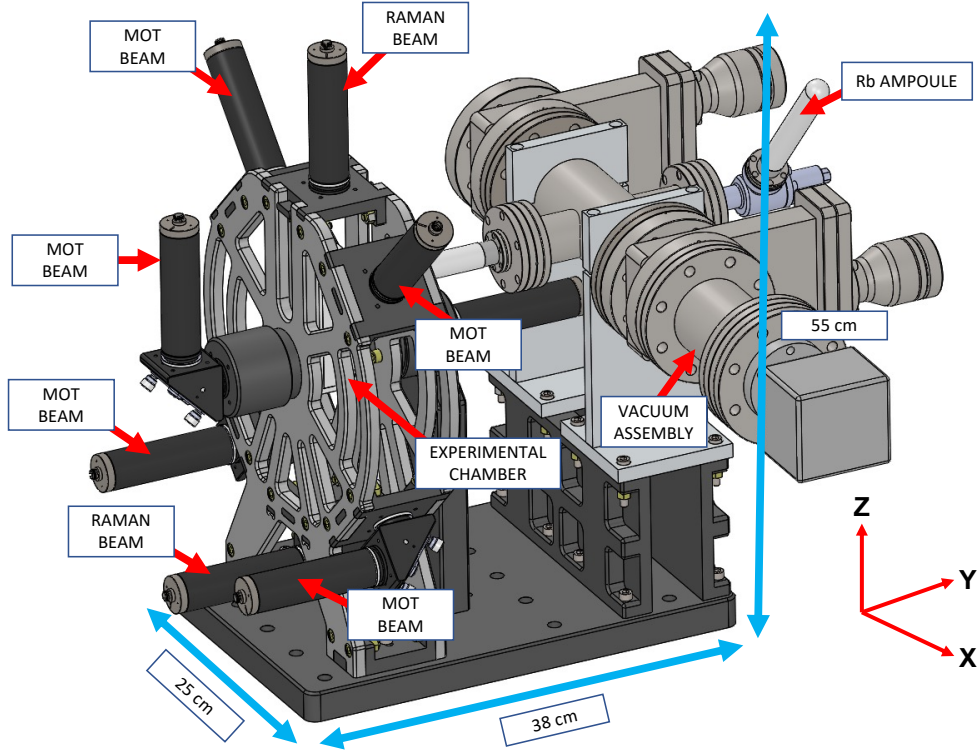


Figure 5.1: Labelled CAD diagram of final assembly with key dimensions.

A few other general design considerations included: ensuring a non-metallic support structure to combat eddy currents to enable rapid magnetic field switching, creating ample space for the delicate science chamber and achieving an optimal coil separation-to-radius for a uniform field gradient with minimal inductance and heating. Thermal effects from the coils (up to  $50^{\circ}\text{C}$ ) were anticipated to cause a deformation of around  $\sim 10\mu\text{m}$  which was acceptable given our alignment tolerance. The structure was made from acrylic as the advantages of materials like PEEK didn't justify the significant cost

increase. Furthermore, hollow carvings in each wedge were made to maximise cell visibility.

### 5.1.1 Coil Design

To provide the magnetic environment for trapping atoms a pair of quadrupole coils and 3 pairs of compensation coils were made. The trapping coils required thought to achieve a compromise between sufficient field gradient, inductance and heating. In this section this optimisation is explored. The inductance of a coil is given by equation 5.1 where  $N$  is the number of turns,  $R$  is the radius,  $a$  is the wire radius and  $\mu$  is the permeability. Therefore, as  $L \propto N^2$  many turns make rapid switching challenging. However, as field gradient is  $\propto NI$  a certain number of turns are needed to reach the target field gradient (16 G/cm). Moreover, a constant field gradient for a decreasing number of turns requires increasing current ( $I$ ), which causes thermal challenges. A further consideration is the maximum ampacity of the wire, for our 1 mm diameter copper wire this is  $\sim 10A$  [108].

$$L = N^2 R \mu \left[ \ln \left( \frac{8R}{a} \right) - 2 \right]. \quad (5.1)$$

Initially some prototype trapping coils were wound onto the external holders but, due to a design oversight this led to sub-optimal field gradient and uniformity. To address this, the field profile of a pair of anti-Helmholtz coils was simulated to try and make improvements. For the magnetic field from a

pair of coils of radius,  $a$  the equations are derived from the Biot-Savart Law. For simplicity the vector magnetic field as generated by a circular loop is naturally expressed in component form in a cylindrical coordinate system as in equations 5.2a and 5.2b.  $K(k_c)$  and  $E(k_c)$  are elliptic integral functions of the first and second kind respectively with parameters defined for a circular current loop of radius  $a$ , with loop axis along the  $z$  axis. By multiplying the equations for single coils by the number of turns ( $N$ ) and reversing the current sign in one coil, equations for coils in the anti-Helmholtz configuration can be obtained. The field contributions from each coil are then summed and the field gradient is computed taking the derivative with respect to position [109].

$$B_{r_c}(r_c, \phi, z) = \frac{\mu_0 I_a}{2\pi} \frac{(z - z_0)}{r_c [(r_c + a)^2 + (z - z_0)^2]^{\frac{3}{2}}} \left[ -K(k_c) - \frac{r_c^2 - a^2 + (z - z_0)^2}{(r_c - a)^2 + (z - z_0)^2} E(k_c) \right]. \quad (5.2a)$$

$$B_z(r_c, \phi, z) = \frac{\mu_0 I_a}{2\pi} \frac{1}{[(r_c + a)^2 + (z - z_0)^2]^{\frac{3}{2}}} \left[ K(k_c) - \frac{r_c^2 - a^2 + (z - z_0)^2}{(r_c - a)^2 + (z - z_0)^2} E(k_c) \right]. \quad (5.2b)$$

$$k_c^2 = \frac{4ar}{(r_c + a)^2 + (z - z_0)^2}. \quad (5.2c)$$

To identify the optimum profile the radius is fixed and the separation varied changing the aspect ratio as explored in figure 5.2. To characterise this we arbitrarily define the parameter uniformity radius to be the radial extent at which the field gradient deviates from its central value by 1%. An aspect ratio of about 1.7 compromises well between peak value and uniformity.

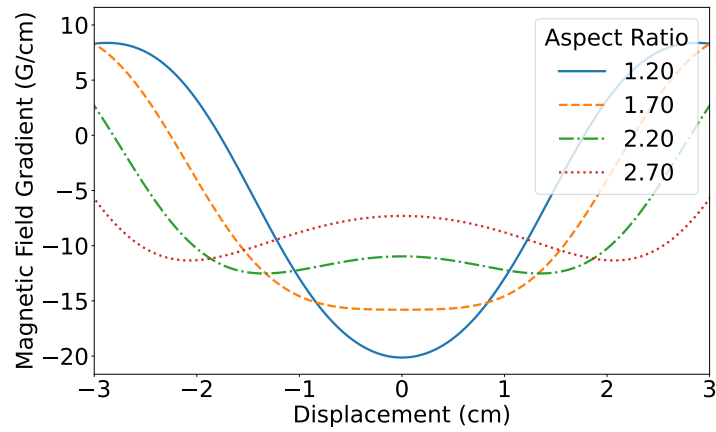


Figure 5.2: Magnetic field gradient profiles for variable coil separation.

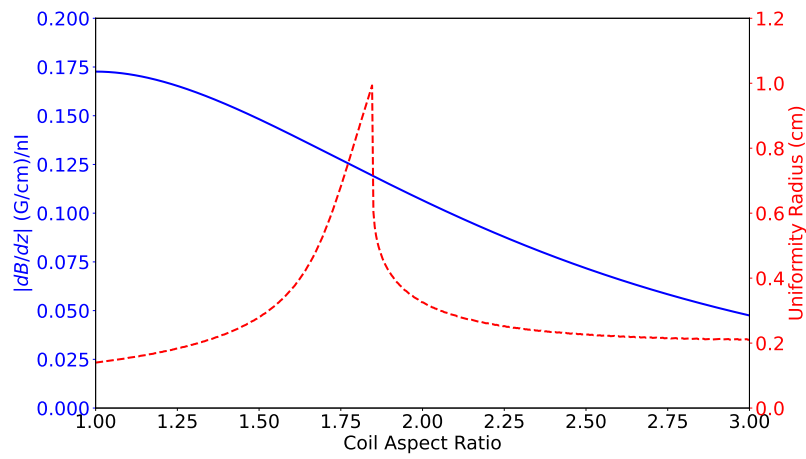


Figure 5.3: Optimising magnetic field gradient uniformity.

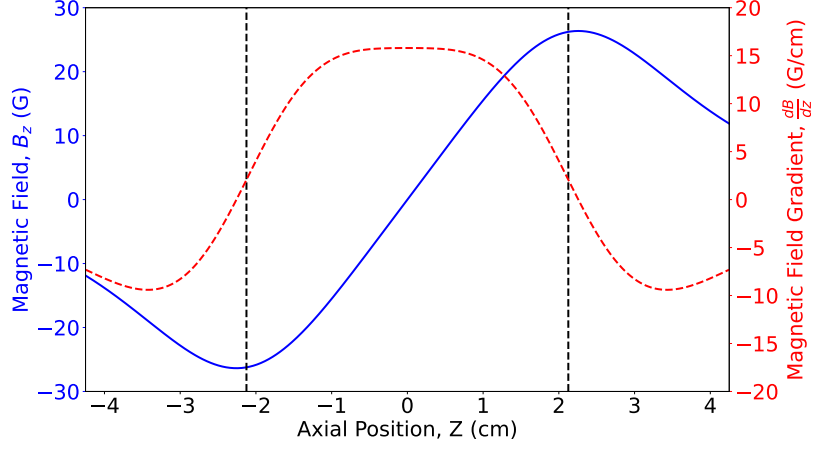


Figure 5.4: Simulated magnetic field (blue) and gradient (red) along the axial direction for the final coil design. Detailed parameters can be found in Table 5.1.

Coil holders were 3D printed and attached inside the pre-existing opto-mechanical structure. Reducing the trapping coil radius lowered the current requirement for achieving the same field gradient and also lowered inductance. However, this also reduced clearance between the glass cell and the coils and was undesirable retrospectively. To refine the simulation the separation and thickness of the coils are accounted for. Figure 5.4 shows the simulated coil profile which was roughly validated with some experimental values. The coil heating was considered but is not concerning due to the low duty cycle of around 0.2, resulting in manageable temperature. To cancel ambient fields, three pairs of compensation coils were created and positioned near the central MOT region and integrated into the optomechanical frame. The decision was made to arrange the compensation coils along the conventional cartesian axes instead

of the diagonal axes defined by the launching beams. This configuration was more optimal considering geometric constraints and avoided significant coupling between axes during optimisation. Adopting compensation coils rather than magnetic shielding also reduces bulkiness and probes potential for a device without such shielding.

Table 5.1: Design specifications for anti-Helmholtz trapping coils.

Parameter	Value	Comments
Number of Turns	30	-
Mean Separation	42 mm	Optimum coil aspect ratio $\sim 1.7$ -
Mean Radius	24 mm	-
Current	3.8 A	-
Axial Field Gradient	16 G/cm	Chosen for efficient trapping of $^{87}\text{Rb}$
Radial Field Gradient	9 G/cm	-
Output Power	3 W	Duty cycle 100%
Inductance	$\sim 100\ \mu\text{H}$	To minimise switching time

### 5.1.2 Control System

The control system uses a PulseBlasterUSB portable, programmable TTL Pulse Generator which sends triggers from up to 24 channels [110]. The PulseBlaster functionality is accessed using Python for integration with other hardware, a channel tester and timing diagram were developed for troubleshooting and accelerated progress and are shown in figures 5.5a and 5.5b.

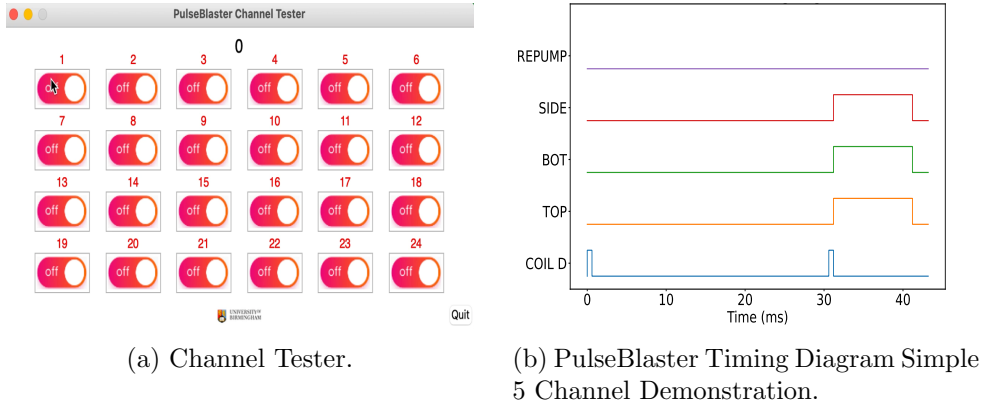


Figure 5.5: PulseBlasterUSB control features.

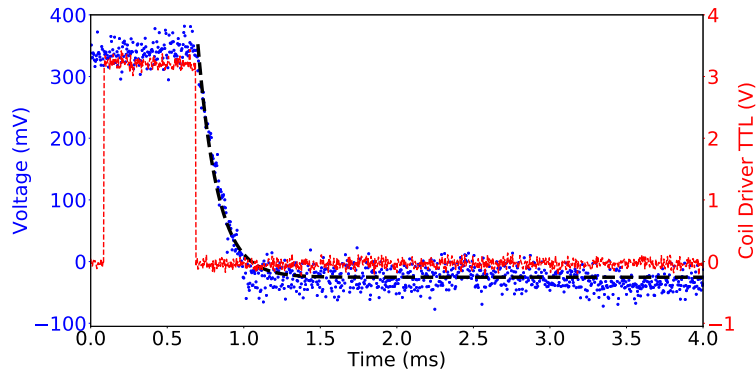


Figure 5.6: Fitting coil driver response with exponential decay model to extract switching time constant,  $\tau = 129 \pm 3 \mu\text{s}$ . Coil driver monitoring voltage (blue scatter points) with fitted portion corresponding to transient response (thick black dashed) and TTL trigger applied to coil driver (red dashed).

Figure 5.6 shows the coil driver responding to the falling TTL edge and demonstrates  $100 \mu\text{s}$  switching. By applying TTL triggers at different times magnetic fields can be generated for performing a MOT, sub-Doppler cooling, atom-interferometry and detection. However, unfortunately the coil driver is programmed with a micro-controller in BASIC which hinders further integration [111]. When the PulseBlaster is reprogrammed this disrupts synchro-

nisation with the coil driver sequence causing a mismatch between optical and magnetic configurations and failure to form a MOT. During the PhD a workaround was implemented by observing the coil driver output and MOT fluorescence, although better control system integration is crucial for future systems. However, for demonstration purposes, correct synchronisation allows measurements to be conducted.

## 5.2 Optics Delivery

To achieve a MOT with moving molasses, the optical system has specific requirements. These include having three beam pairs with independent frequency and power control, ensuring stable power division between the top and bottom beams for launching. The experiment operates on the  $^{87}\text{Rb}$  D<sub>2</sub> transition, generating MOT frequencies exclusively in the free-space setup. The Raman laser, which is discussed in the next chapter, is separate from the cooling laser system. While the long-term goal is to achieve cold-atom generation and interferometry with a single-seed system, the systems were separated for faster development [77]. Figure 5.9 shows the energy level diagram and the relevant transitions for the experiment. The required frequencies are near 780 nm so can be reached with commercial laser diode technology. Two lasers, an Eagleyard EYP-DFB-0780-00080-1500-BFW01-0002 and New Focus, Vortex 6900 act as laser 1 (master) and laser 2 (repumper) in figure 5.8. The master laser is split with a polarisation beam splitter (PBS) into two parts, one



portion (10mW) is injected into the tapered amplifier (TA) and amplified to 1.5 W. The other portion (15 mW) propagates through a double-pass AOM setup, the returned light acts as a reference laser which is injected into Modulation Transfer Spectroscopy apparatus (MTS) locked to the  $F = 2 \rightarrow F = 3'$  transition [112]. The high-power cooling light is split into three paths with PBS cubes and half-wave plates. Each path contains a double-pass AOM setup enabling control of the light frequency over a 25 MHz range without significant changes in output power. Compared to the master laser frequency, the cooling light is shifted by  $2(\omega_1 - \omega_i)$ , with the RF frequencies for driving the AOMs shown inset in figure 5.8. This system enables relatively independent control of cooling light intensity and frequency at the output coupler. To achieve moving molasses, the relative detuning of the top and bottom beams is adjusted by shifting the frequencies of AOM3 and AOM4 in the cooling laser stage. The repumper beam is split into two paths, with one portion input into the fibre splitter for the side beams, and the other mixed with the reference laser and phase-locked to the  $F = 1 \rightarrow F = 2'$  transition. To minimise optical back-reflections, an optical isolator is placed after the tapered amplifier output, providing at least -60 dB suppression to prevent feedback. Polarisation stability is crucial and achieved by using a zero-order  $\lambda/2$  waveplate and a polariser to maximise transmission. Setting the polarisation state correctly before the tapered amplifier is important for optimal power output and stability. After optimising polarisation, the output power of the TA was

measured to assess its performance. A notable correlation was observed between the temperature of the TA housing and the output power. Software limitations prevent adjusting PID loop responses for stability enhancement resulting in  $\sim 1\%$  output fluctuations.

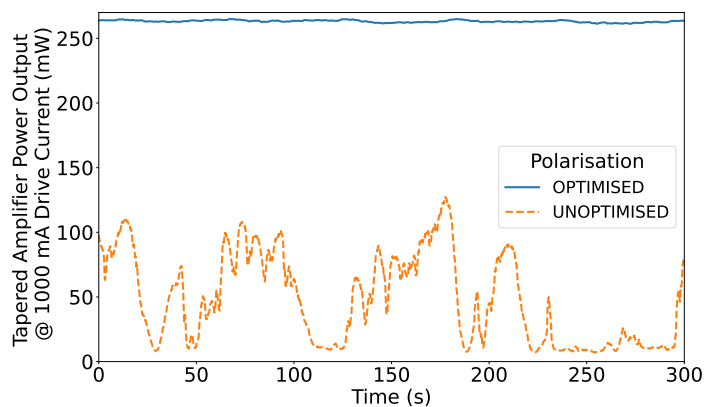


Figure 5.7: TPA780P20 - 780 nm Tapered Amplifier performance with and without polarisation optimisation.

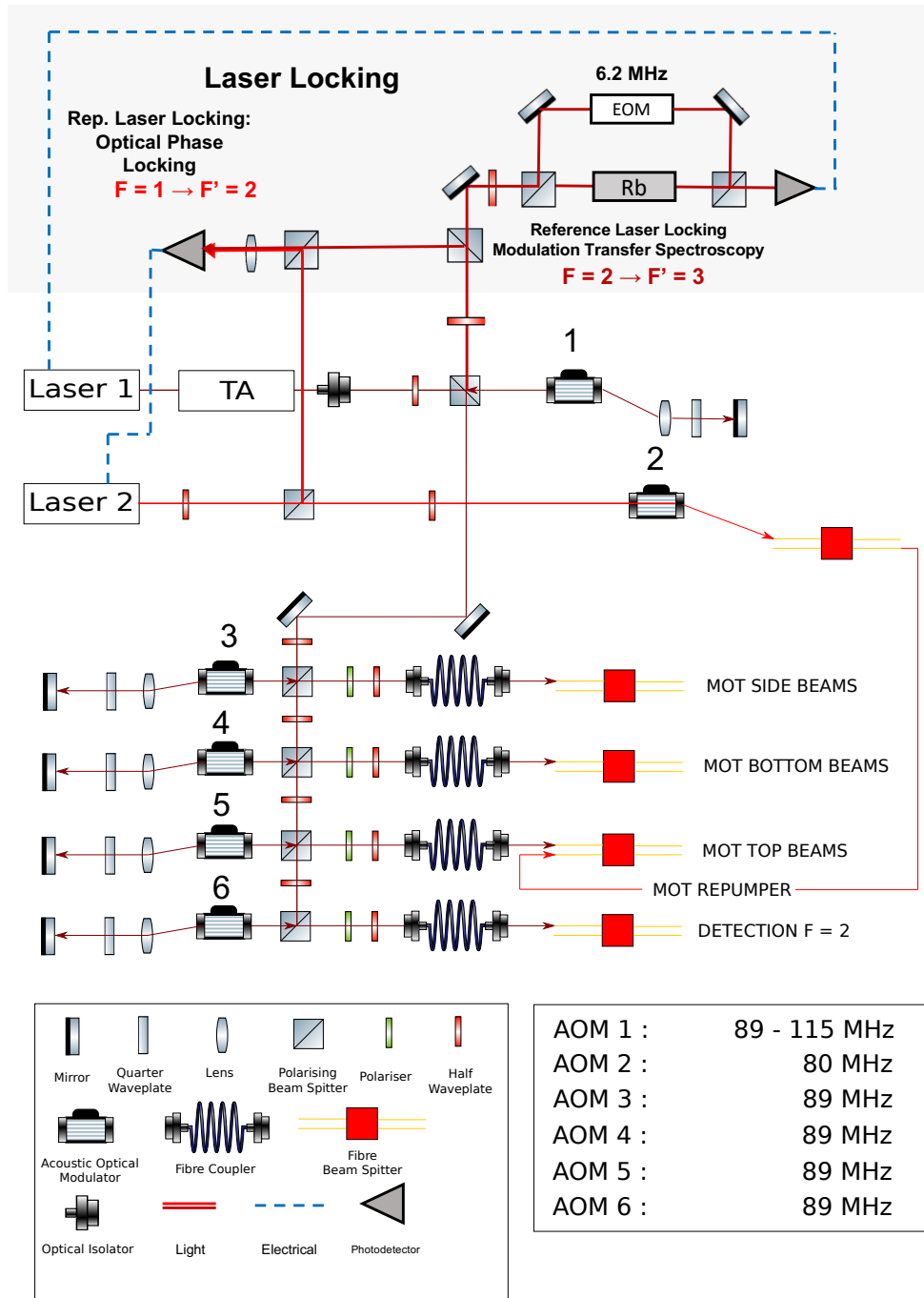


Figure 5.8: Schematic view of the free space optics system. The typical frequencies used for the experiment are shown inset.

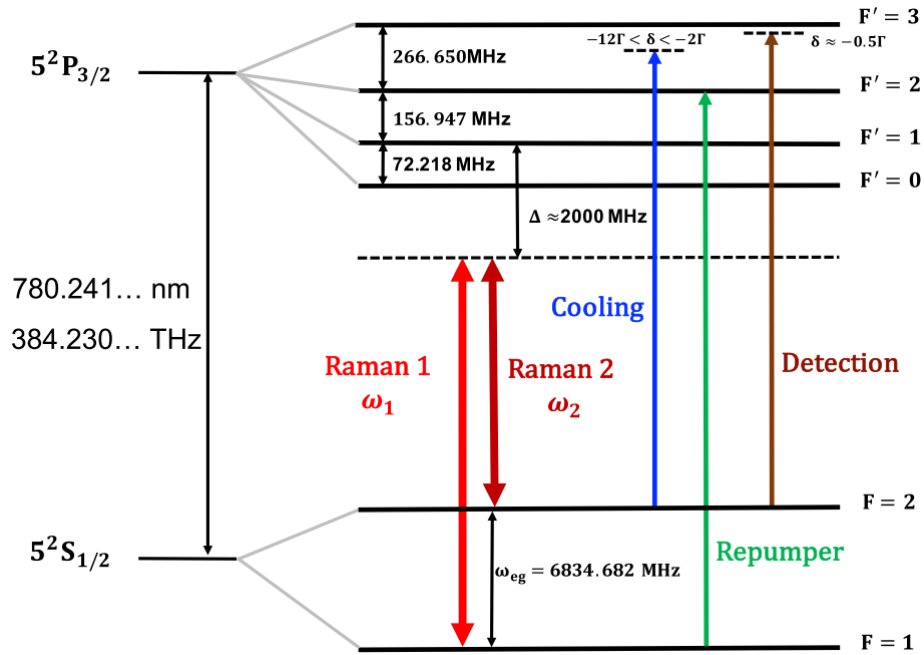


Figure 5.9:  $^{87}\text{Rb}$  D<sub>2</sub> line hyperfine structure with relevant frequencies labelled, modified from [89].

### 5.3 Static Operation

Following polarisation, alignment, and power distribution checks, a MOT was successfully generated. Initial characterisations of the MOT were conducted in static operation with light and trapping coils continuously switched on. Atom number is strongly dependent on laser power. To investigate this, the cooling laser power was adjusted while keeping other parameters constant. A fairly linear growth in atom number was observed, reaching saturation at the highest achievable powers (figure 5.10). Another factor to consider is the repumper laser power required to prevent atoms accumulating in the  $F = 1$  dark state. The power delivered by this repumper laser is independent of the

power delivered to the beat note. This allows for power adjustment without affecting locking. It is observed that the transition is well saturated with the available repumper power of 8 mW.

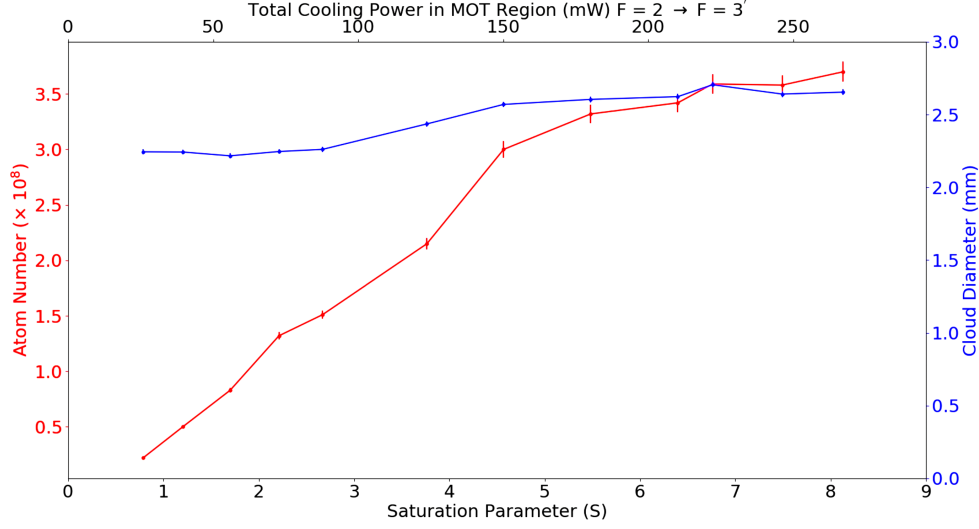


Figure 5.10: Atom number for variable cooling power.

Before exploring any coupling between field gradient and detuning first 1D parameter scans were performed. Scanning the current in the quadrupole field coils between 0 and 5A gives an axial field gradient range of 0 to 21 G/cm in the trap centre. The detuning was fixed at  $\Delta = -3$  and the laser power was set to 30 mW per beam. The influence of magnetic field gradient is shown in figure 5.11.

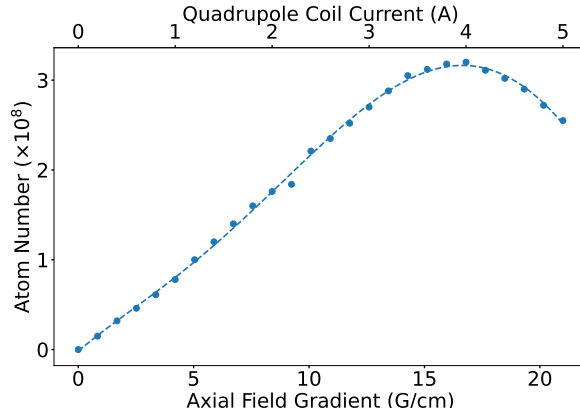


Figure 5.11: Effect of field gradient on atom number for a fixed detuning of  $\Delta = -3$  and 30 mW per beam.

Small field gradients result in a shallow trap depth, capturing only the slowest atoms. Conversely, for larger field gradients the Zeeman shift at the beam's edge is similar in size to the detuning of the cooling beams reducing overall trapping effectiveness. The optimal value of around 16 G/cm aligns with previous studies on  $^{87}\text{Rb}$ . The detuning of the cooling lasers was then adjusted using the AOMs with figure 5.12 showing the investigation results and revealing a prominent peak at  $\Delta = -3$ . To investigate any coupling between the field gradient and detuning a 2D scan was performed. Within the range of  $-3.1 < \Delta < -2.7$  and  $14 < A < 16$  G/cm performance is optimal, achieved with a coil current of around 3.5A. While it is possible to reduce turns to achieve the same field gradient at a higher current, it is not necessary as the switching time is already sufficient.

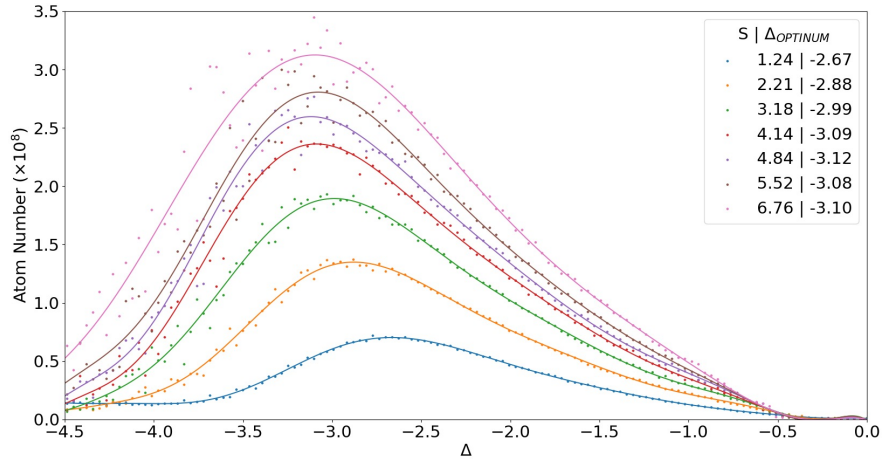


Figure 5.12: Effect of variable detuning and power on atom number for fixed field gradient of  $A = 14.3$  G/cm. The optimum detuning ( $\Delta_{\text{OPTIMUM}}$ ) for a given saturation parameter is shown inset.

The duty cycle is a key parameter in high bandwidth MOT operation. It represents the useful fraction of an individual experimental cycle, specifically the time spent in free-fall. The remaining time is allocated for recapturing and loading atoms back into the trap for the next cycle. To investigate the influence of the duty cycle on atom number, a dynamics simulation in section 3.4 is compared with experimental data.

## 5.4 Dynamic Operation

*The contents of this section form part of a PRA paper submission*

*“Magneto-optical trap performance for high-bandwidth applications”*

The duty cycle describes the useful fraction of an experimental cycle (free-falling time) and is a key experimental parameter. To investigate how duty

cycle influences atom number the dynamics simulation in section 3.4 is compared against experimental data. Atom number decays gradually as drop time increases from 0 to 8 ms due to reduced reloading time. Within this range, the recapture efficiency remains constant, indicating sufficient restoration force for reloading times exceeding 2 ms ( $P_{\text{restored}} = 1$ ). Imperfect recapture efficiency is caused by collisions with the background vapour, with  $P_{\text{no collision}} = 85\%$  at 100 Hz. Atom number declines dramatically for drop times exceeding 8 ms, indicating the failure of the recapture mechanism. Good agreement is observed between the experimental data and the model across bandwidths. This could be related to the Gaussian dependence of the trapping beams which becomes more prominent for increasing freefall. To validate the collision model duty cycle scans with fixed cycle times of 2.5, 5, 10 and 20 ms are performed. By extracting  $P_{\text{no collision}}$  from the data as the drop time approaches 0 ms, it can be plotted against Eq. (3.10) for our operating pressure of  $2.9 \times 10^{-7}$  mbar. Through this analysis, the collision model is validated (see Fig. 5.13).



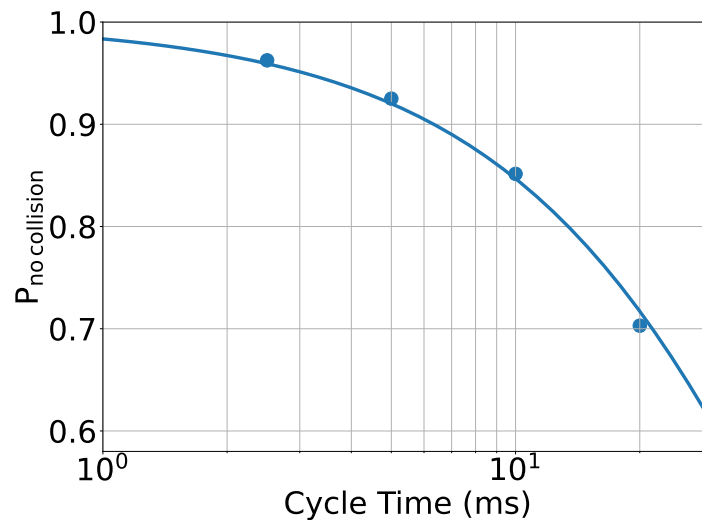
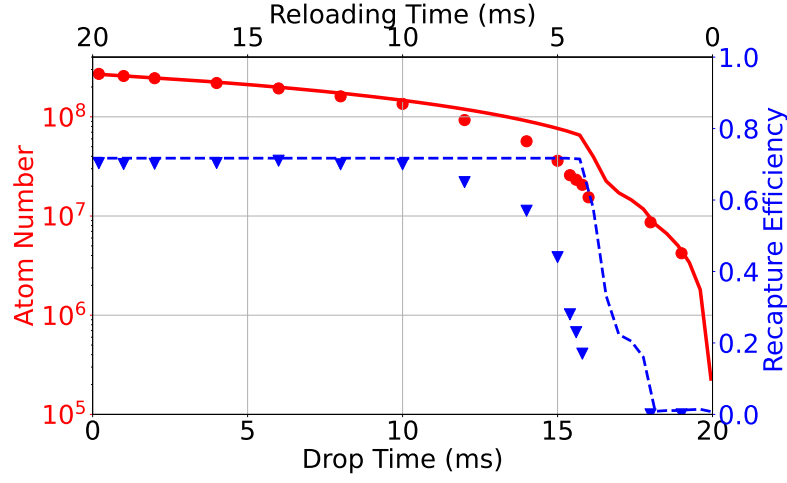
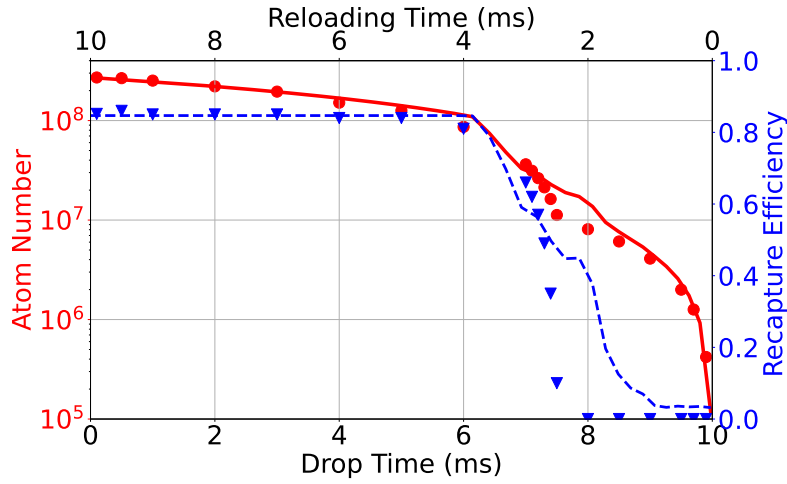


Figure 5.13: Pressure induced collision model, theoretical model (line), experimental data (points).



(a) 50 Hz



(b) 100 Hz

Figure 5.14: Steady state atom number (red solid) and recapture efficiency  $P_{\text{no collision}}P_{\text{restored}}$  (blue dashed) for variable duty cycle. Experimental data points are scattered.

To further highlight the importance of recapture longer drop times are simulated with a short reloading time. To model this, the reloading time is fixed, the drop time is incremented and the steady state atom number is computed.

After falling  $2\sigma_r = 10$  mm, an atom will fall out of the trap centre in  $\sim 45$  ms

as reflected in the decline in Fig. 5.15. For drop times  $\ll 45$  ms, recapture dominates as atoms remain within the trapping region. However, for drop times  $> 45$  ms, the MOT is no longer in the trapping region, making recapture impossible. Consequently, the MOT consists solely of atoms loaded from the background vapour. Longer loading times show a less pronounced drop-off, indicating the need for increased reloading time when leaving the recapture-dominated regime.

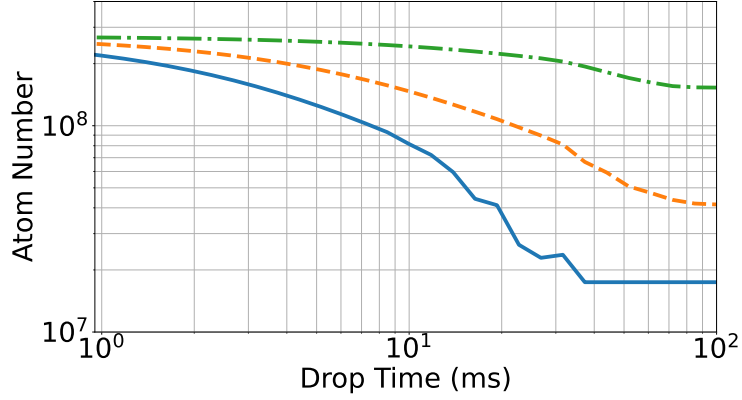


Figure 5.15: Steady state atom number for variable drop time with a fixed loading time: 4.0 ms (blue solid), 10 ms (orange dashed) 50 ms (green dash-dot).

The model is further validated by calculating and measuring the reloading time for a steady state MOT of  $10^8$  atoms. As anticipated, the recapture efficiency experiences a decline to zero at 45 ms of drop time. For small drop times the loading time required tends to the MOT restoration time for a  $^{87}\text{Rb}$  atom ( $\sim 3$  ms) in this regime. When recapture fails, the time required is determined entirely by background loading and is given by  $\frac{1 \times 10^8}{4.5 \times 10^9 \text{ s}^{-1}} \sim$

25 ms. For lower pressures ( $\sim 10^{-8}$  mbar) this time will be significantly longer due to the reduced loading rate. Overall, a good fit is observed between the model and experiment. Practically, experiments should carefully balance loading time to preserve recapture without sacrificing measurement bandwidth. Optimisation can be achieved by analysing the atomic signal decline at increasing duty cycles, identifying the point where the recapture mechanism fails to determine the necessary trap loading time (see Fig. 5.14b).

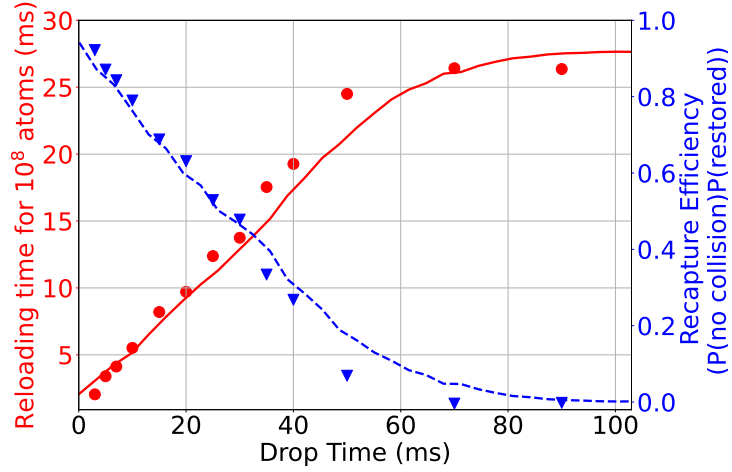


Figure 5.16: Time to load  $10^8$  atoms for variable drop time (red solid), recapture efficiency  $P_{\text{no collision}}P(\text{restored})$  (blue dashed). Experimental data points are scattered.

For optimal sensitivity the duty cycle requires optimisation to balance the recapture and interrogation periods. Assuming a certain bandwidth, duty cycle and shot noise limited detection the only unknown in Eq. (4.12) is atoms participating in the interferometer,  $n$ . To acquire this the recapture simulation is run for the chosen duty cycle and MOT parameters to obtain the recapture efficiency. The atom number is then computed using Eq. (3.14).

A conservative 1% of atoms are assumed to complete the interferometer,  $N_{\text{AI}} = 0.01N_{\text{MOT}}$ . To account for sub-Doppler cooling, state preparation and launching; a 3 ms preparation time is allocated within the cycle time. A cloud temperature of 10  $\mu\text{K}$  is adopted following sub-Doppler cooling. Fig. 5.17 shows the sensitivity simulation at 100 Hz operation for variable duty cycle.

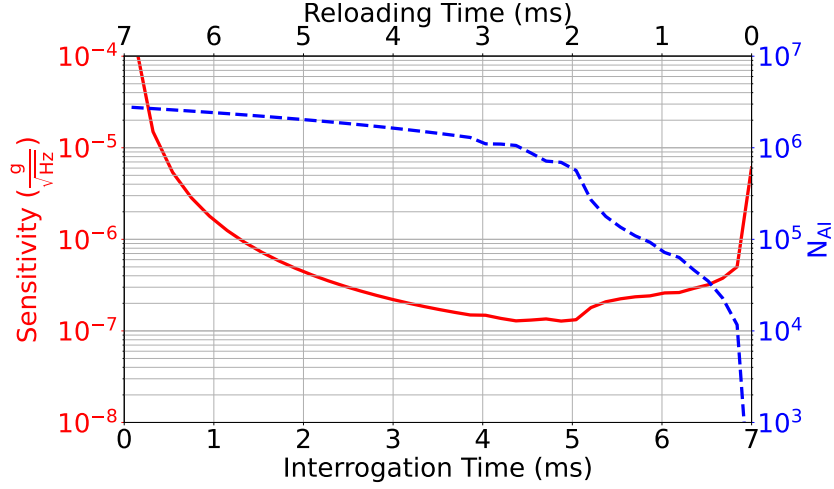


Figure 5.17: Optimising sensitivity by optimising balance between recapture and interrogation time, sensitivity (red solid), participating atoms (blue dashed). The optimised cycle consists of a 5 ms interrogation, 2 ms recapture and a set 3 ms of additional preparation (cooling, state preparation, launching). AI parameters:  $F = 100 \text{ Hz}$ ,  $\eta = 1$ ,  $N_{\text{AI}} = 0.01N_{\text{MOT}}$ .

For lower duty cycles there are more atoms but the sensitivity improvement from increased interrogation time dominates over the reduced atoms. For reloading times  $< 2 \text{ ms}$  the capture processes are inhibited and the atom number falls to zero diminishing sensitivity. Fig. 5.17 suggests a performance limit of  $1 \times 10^{-7} \frac{g}{\sqrt{\text{Hz}}}$  at 100 Hz operation. Given the finite recapture time it is interesting to consider optimal sensitivity for variable bandwidth. To ex-

plore this the simulation in Fig. 5.16 is reprocessed. By adding the drop and reloading time together and including an additional 3 ms of preparation time a certain cycle time and therefore bandwidth is defined. For this bandwidth  $10^8$  atoms are generated and so sensitivity can be computed with Eq. (4.12). For increasing bandwidth the optimal duty cycle decreases gradually as the necessary reloading time represents a larger fraction of the cycle, see Fig. 5.18. At a certain bandwidth the cycle time is insufficient to interrogate, recapture and prepare atoms. For short drop time around 2 ms is required to recapture atoms and so with an additional preparation time of 3 ms the limiting bandwidth is  $\frac{1}{5\text{ms}} \simeq 200$  Hz. Given the performance limits it is worth summarising the advantages, disadvantages and future prospects of the high bandwidth approach for quantum sensing. Quantum sensors offer low bias and high-stability enabling long term inertial navigation measurements not currently feasibly with classical sensors. High bandwidth quantum sensors would therefore be attractive for navigation where measurement rates  $> 100$  Hz are needed for operation on mobile platforms. As highlighted bandwidth and sensitivity present a compromise although the reduced free-falling distance at high bandwidth makes the approach compelling for miniaturisation developing devices more robust to challenging environments [61]. The  $\sim \mu\text{g}/\sqrt{\text{Hz}}$  sensitivity offered at high bandwidth would be useful for inertial navigation with techniques such as large-momentum transfer potentially offering a route to clawing back sacrificed sensitivity [49]. Even presently ship-borne mea-

measurements have demonstrated sensitivities at the  $\sim\mu\text{g}$  level [5]. Moreover, hybrid methods have been implemented to increase bandwidth using a quantum sensor to correct a classical device [113]. Further developments could offer potential for absolute positioning on a metre scale independent of environment without satellite navigation. Moreover, high bandwidth operation would also be desirable for faster civil engineering surveys providing feedback on the condition of water pipes and identifying voids and mine shafts.

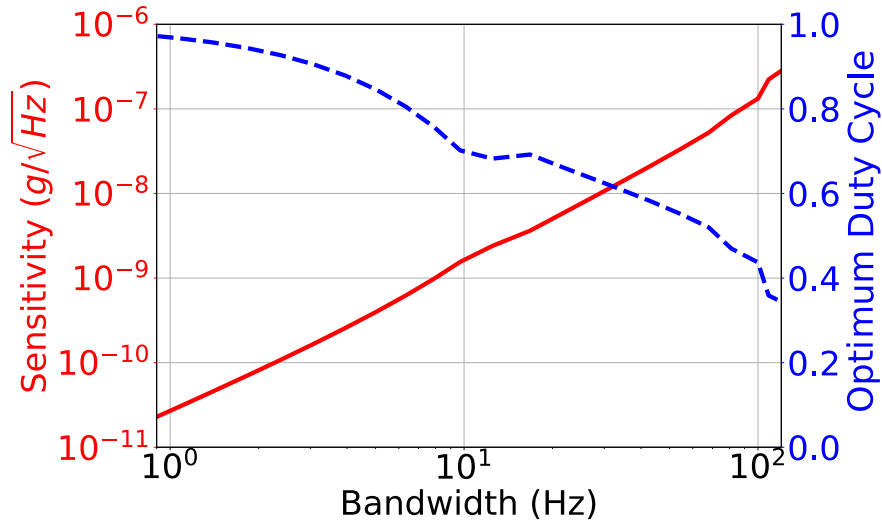


Figure 5.18: Sensitivity projection for variable bandwidth based on simulation in Fig. 5.16. For each bandwidth the cycle consists of an additional 3 ms of preparation.

## 5.5 Launching

As described in section 4.3 the system uses 2D moving molasses to launch atoms and break Raman degeneracy. The launch is characterised by tracing the cloud centre during its time-of-flight. The cloud is imaged with the CMOS

camera at the start of the launch and at some time (15 ms) later. To provide useful statistics the cloud is imaged multiple times at different stages in the launch. The positional variation of the MOT centre after the launch is 0.03 mm and 0.12 mm along the X and Y directions respectively. This compares with 0.015 mm and 0.15 mm for the same conditions but without a launch. To characterise the launch angle 15 launches were performed and the bias and angular deviation were measured to be  $-0.5^\circ$  and  $0.5^\circ$  respectively.

## 5.6 Temperature

Cloud temperature is measured by measuring thermal expansion by imaging the cloud at different times after sub-Doppler cooling. Temperature is determined by fitting cloud size to the model in equation 3.15. The cloud size is determined by fitting to the 2D Gaussian given by equation 5.3.

$$f(x, y) = B \left[ \left( e^{-\left[ \frac{(x-x_0)^2}{2\sigma_x^2} + \frac{(y-y_0)^2}{2\sigma_y^2} \right]} \right) \right] + A. \quad (5.3)$$

The fluorescence signal associated with the atomic cloud is given by the volume under a 2D Gaussian given by equation 5.4.

$$V = \int_{-\infty}^{\infty} \int_{-\infty}^{\infty} f(x, y) dx dy = 2\pi B \sigma_x \sigma_y. \quad (5.4)$$



The parameters of the Gaussian are obtained by fitting data to equation 5.3.

A corresponds to a vertical offset accounting for background light.

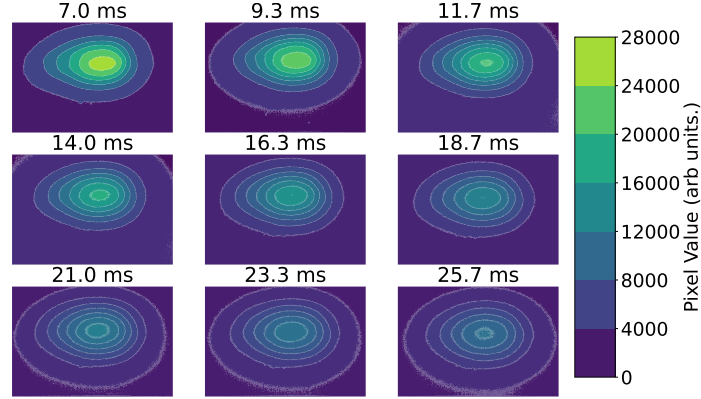


Figure 5.19: Fluorescence imaging of the MOT for variable free expansion time, images captured using the ORCA<sup>®</sup>-Flash 4.0 V2 Digital CMOS camera C11440-22CU.

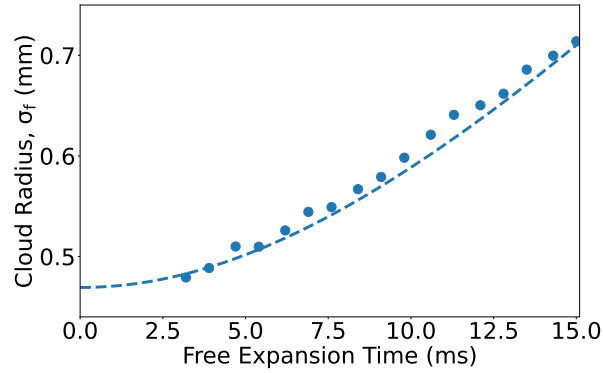


Figure 5.20: Thermal expansion of a cloud with 2 ms of sub-Doppler cooling. A temperature of  $13.4 \pm 0.4$   $\mu$ K is measured.

Low cloud temperatures are essential to sensor performance. Figure 5.20 demonstrates the thermal expansion method used to determine temperature. When using a relatively small 5 mm Raman beam diameter, spatial irregularities become very significant without sub-Doppler cooling, which severely

limits T time. Additionally, higher temperatures decrease the efficiency of Raman pulses, emphasising the crucial role of sub-Doppler cooling. Atoms were cooled whilst performing simultaneous moving molasses to launch them to  $0.25\text{ ms}^{-1}$  which increases cloud temperature to around  $20\text{ }\mu\text{K}$ .

### 5.6.1 Velocimetry

To validate the cloud temperature measurements, the Raman laser can be used to determine temperature eliminating the need for calibration to convert pixels to physical distance. Figure 5.21 shows how sub-Doppler cooling affects the width and peak of the Raman transition. The temperature is determined using the framework in section 4.2 as the width of the Raman transition depends on the pulse length and cloud temperature. With the known Rabi frequency, the temperature is found to be  $22.7 \pm 1.8\text{ }\mu\text{K}$ . Although thermal expansion is generally found to be more accurate and efficient, this method serves as a helpful sanity check.

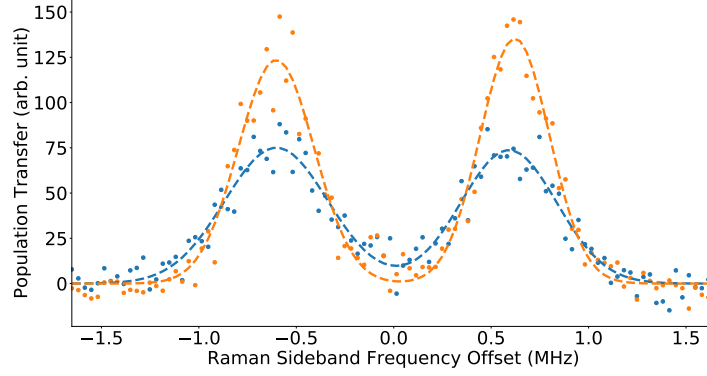


Figure 5.21: Illustration of Raman velocimetry method used to estimate cloud temperature for 2.0 ms of sub-Doppler cooling with  $t_\pi = 3.5 \mu\text{s}$ . Inefficient cooling (blue dashed)  $T = 71.7 \pm 7.3 \mu\text{K}$ , efficient cooling (orange dashed)  $T = 22.7 \pm 1.8 \mu\text{K}$ .

### 5.6.2 Piecewise Ramps

Simultaneous sub-Doppler cooling was performed, followed by the execution of rigorous optimisation of the cooling mechanism without launching. Piecewise ramps were utilised for power and frequency to explore this optimisation process. However, prior to this magnetic field optimisation is necessary as these fields degrade sub-Doppler cooling, limiting temperature. Temperature was measured using the thermal expansion method, revealing sensitivity to  $\sim 10$  mG fields (Fig. 5.22). Optimisation proceeded sequentially along the Y, X and Z axes. During this optimisation, the sub-Doppler cooling ramp was not optimised with frequency ramped from  $-3\Gamma \rightarrow -10\Gamma$  and power from  $30 \rightarrow 0$  mW over 3.0 ms. After identifying the compensation condition, focus shifted to optimising power and frequency ramps.

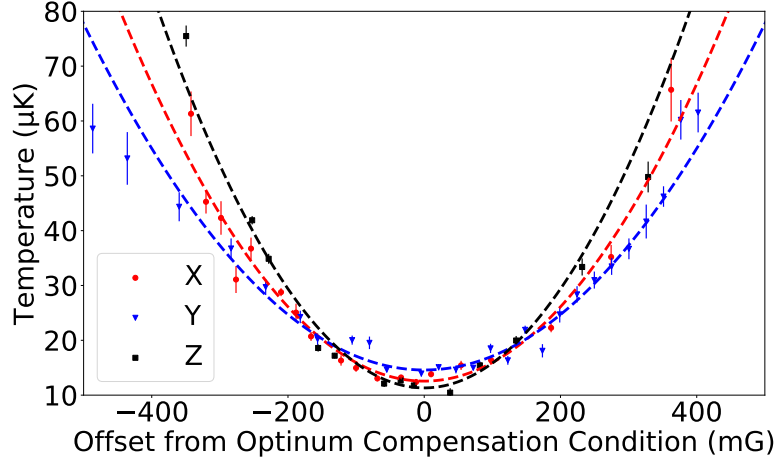
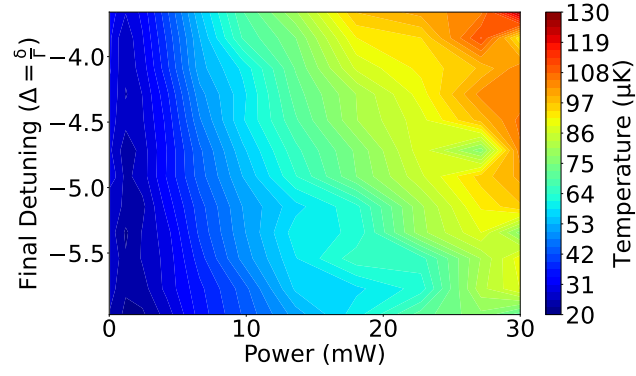
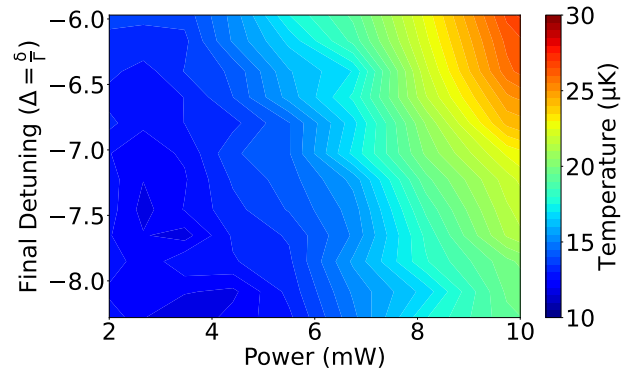


Figure 5.22: Magnetic field optimisation for 3.0 ms of sub-Doppler cooling time. Optimum compensation conditions:  $X = 166 \pm 2$  mG,  $Y = -72 \pm 3$  mG and  $Z = 373 \pm 2$  mG. Axes are as defined in figure 5.1.

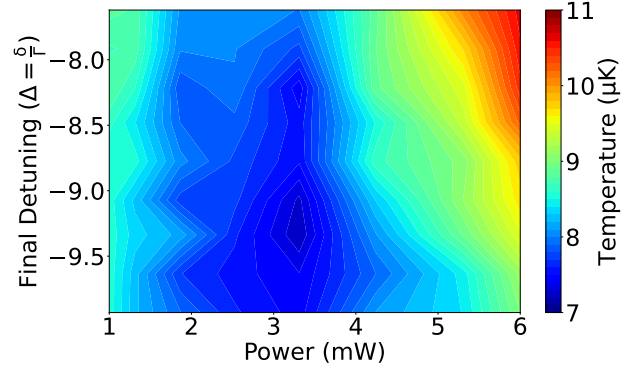
To explore this, the cooling process is divided into stages, scanning the final detuning and power conditions for each stage. This approach relies on independent power and frequency control to examine the response to different ramps. The sub-Doppler process is split into three stages. The optimisation begins with the first 0.5 ms, scanning the final power and detuning while measuring the temperature for each configuration. Following this (Fig. 5.23a) optimum final parameters of 8 mW beam power and a detuning of  $-5\Gamma$  are identified. These become initial conditions for the next optimisation stage. This approach is then applied for the second and third optimisation stages illustrated in Figs. 5.23b and 5.23c respectively. For clarity, each optimisation stage consists of a 2D scan of power and frequency ramp rates, requiring 225 (15x15) temperature measurements. Temperature data is contoured interpolating between points.



(a) First Stage



(b) Second Stage



(c) Third Stage

Figure 5.23: Multi-stage sub-Doppler cooling optimisation

Fig. 5.24 uses the AOM characterisation and DDS limitations to reconstruct power and frequency ramps experienced in multi-stage cooling (Figures 5.26a and 5.26b). Unlike in many systems, it is observed that it is beneficial to not completely ramp down MOT power in the final stage. This observation is slightly surprising and will require further investigation. It could suggest that performance is no longer limited by the ramp slope but rather by magnetic fields or beam power imbalance.

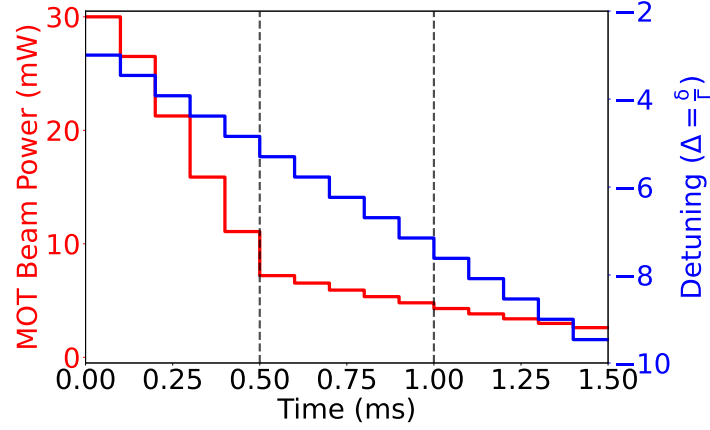


Figure 5.24: Reconstructing power (red solid) and detuning (blue dashed) ramps based on AOM characterisation and 100  $\mu$ s resolution of DDS. Most optimal ramps shown for the three-stage cooling process. Black vertical lines separate different cooling stages.

To demonstrate the value of this procedure, performance is compared with a single-stage process with the same length, start and end conditions (as depicted in figure 5.24). Examining the sub-Doppler cooling process, the temperature evolution is studied by prematurely turning off the cooling and repumping light. The optimal ramp in the multi-stage process allows for rapid cooling on ms timescales, achieving a significant temperature reduction

before using a slower ramp (Fig. 5.25). As the light-on time approaches 0 ms, the temperature approaches the Doppler cooling limit of 140  $\mu\text{K}$ . Increasing the cooling time in the single-stage process reveals that temperatures of 7-8  $\mu\text{K}$  require a cooling time of 5 ms.

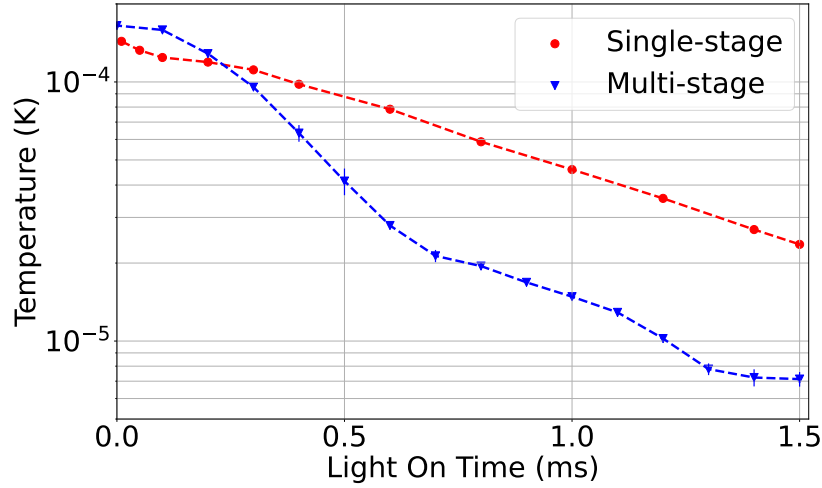
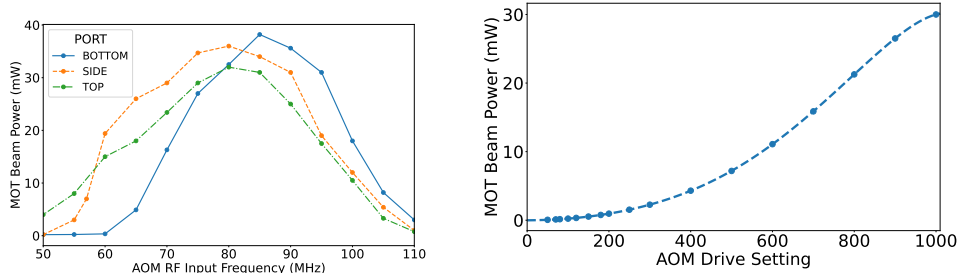


Figure 5.25: Prematurely switching off the light during the cooling sequence allows temperature evolution to be mapped. The multi-stage piecewise sequence achieves a final temperature of  $7.2 \pm 0.5 \mu\text{K}$ , while a single-stage approach with the same cooling time reaches  $23.6 \pm 0.4 \mu\text{K}$ .

### 5.6.3 Outlook

The current laser system for MOT generation has three independent outputs for launching atoms with six-beam moving molasses. Despite efforts to balance beam powers, the light field experienced by atoms is somewhat inhomogeneous, particularly at lower intensities during sub-Doppler cooling. Another limitation is the restricted frequency range and agility of the system, currently limited to  $-10\Gamma$  and  $-4\Gamma/\text{ms}$  beyond which locking fails. Addition-

ally, the resolution of the DDS time steps ( $100\ \mu\text{s}$ ) coupled with short cooling timescales, results in frequency jumps instead of smooth ramps. This prevents further subdivision of the cooling period to explore even shorter timescales. These constraints can be overcome by fully implementing the fibre-Bragg grating laser system described in the next chapter to support both MOT and Raman operation. This will eliminate bandwidth and agility limitations on the system allowing sub-Doppler cooling to be performed without perturbing the lock. This would enable a more comprehensive investigation of sub-Doppler cooling on the shortest timescales. The system currently uses compensation coils without magnetic shields, which may impact performance. However, the objective of compact quantum sensing makes additional weight from magnetic shields undesirable. Spatial inhomogeneities due to finite beam size could also be a potential concern. This could be mitigated by increasing beam size, although this will conflict with SWaP-C criteria for mobile sensors.



(a) Characterising AOM responses in six-beam MOT system. (b) Mean beam power (mW) for variable AOM power settings.

Figure 5.26: AOM Characterisation.

In cold-atom systems, optimising sub-Doppler cooling is time-consuming and



requires expertise. However, a high-bandwidth approach can address these challenges. The optimisation method demonstrated achieves the coldest temperature in the shortest time, as shown in Fig. 5.24. It also reduces the time and skill needed for optimisation, which is important as sensors become more commercialised. To illustrate, consider a MOT operating at 10 Hz bandwidth. For each cooling stage, a 2D scan of power and frequency ramp rates is performed, requiring 225 temperature measurements. Each temperature measurement requires around 10 points, resulting in about 2000 MOT cycles per optimisation stage. With the 3-stage optimisation, the entire process can be completed within a few minutes, which is significantly faster than traditional approaches. Furthermore, additional time savings can be achieved by adjusting the optimisation algorithm. For the initial stage, a coarse scan with less precise temperature measurement can be used, while subsequent stages can have improved grid resolution at the expense of time. In summary, adopting an automated temperature optimisation approach could eliminate challenges related to ramp design in sub-Doppler cooling, reducing development time for cold-atom systems. With a high-bandwidth approach, temperature optimisation can be accomplished within minutes, facilitating efficient re-calibration when transporting devices between survey sites.

## 5.7 Experimental Sequence

To conclude this chapter a typical experimental sequence for measuring gravity is presented highlighting individual steps as part of the broader experimental picture.

1. MOT loading for 20 ms to achieve a healthy  $10^8$  atoms.
2. Downward launch with sub-Doppler at  $0.25 \text{ ms}^{-1}$  for 3 ms. Temperatures of  $20 - 25 \text{ } \mu\text{K}$  are achieved by ramping the cooling beam intensity to zero and sweeping the detuning from  $-3\Gamma \rightarrow -10\Gamma$ .
3. Repumping light switched off towards end of sub-Doppler cooling to prepare atoms in  $F = 1$  state.
4. A large 4G quantisation (bias) field is applied along the vertical direction, the Raman laser is then resonant only with the  $|F = 1, m_F = 0\rangle$  state as atoms in this state are minimally sensitive to magnetic fields.
5. Perform  $\frac{\pi}{2} - \pi - \frac{\pi}{2}$  pulse sequence with chirped Raman laser. Unlike many other cold atom experiments the experiment does not perform velocity selection with blow-away pulses as this will compromise the recapture mechanism.
6. Remove quantisation field, detect  $F = 2$  state with a  $150 \text{ } \mu\text{s}$  pulse resonant with the  $F = 2 \rightarrow F = 3'$  transition.
7. Recapture and load atoms into subsequent MOT.

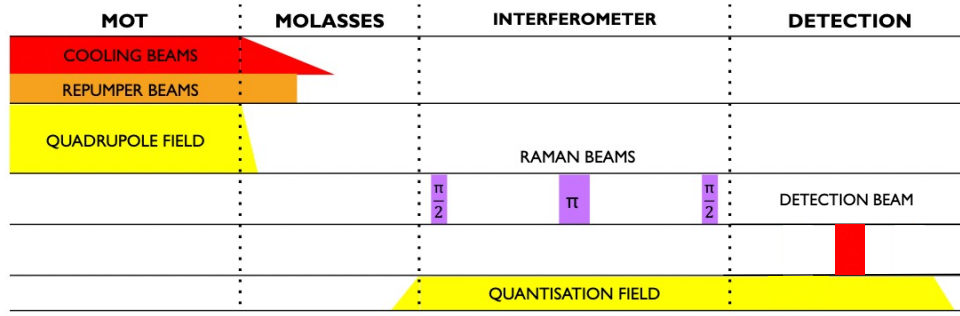


Figure 5.27: Schematic representation of a Mach-Zehnder atom interferometer sequence, showing cooling, atom interferometry, and detection stages. Durations are not drawn to scale.

## Chapter 6

# Raman Laser System

As highlighted in section 5.2 cold atom systems need to generate several optical frequencies with mrad phase coherence. They also require frequency agility for ramping lasers during cooling and to compensate the free-fall induced Doppler-shift during interferometry. Fast frequency switching is also needed to push high-bandwidth operation. A large amplitude extinction ratio is also desirable to avoid coherence loss during measurement with single-seed operation ideal for a simpler compact device [7, 114–117]. This chapter showcases our Raman laser which satisfies these criteria, highlighting its current technical limitations with a pathway to further developments.

## 6.1 Overview

A system overview is provided highlighting key operational concepts, more details can be found in [118]. After modulating the seed laser or carrier frequency the spectrum in figure 6.1 (c) is generated. This spectrum passes through two fibre-Bragg gratings, the reflected output is then taken from each of these [119, 120]. This selects only the narrow-band of frequencies in figure 6.1 (b) containing the desirable frequencies for laser cooling and atom interferometry with  $^{87}\text{Rb}$ . As a result the carrier and undesirable sidebands are suppressed  $> 40$  dB by the Fibre-Bragg gratings to avoid driving potentially unwanted transitions. Each Fibre-Bragg grating provides only 20 dB suppression motivating the need for two to sufficiently suppress the carrier frequency.

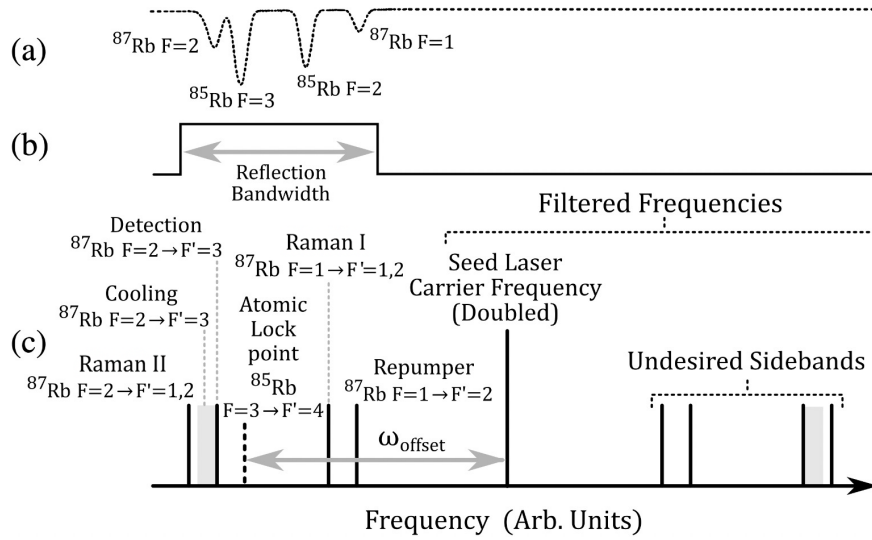


Figure 6.1: The Fibre Bragg grating can be tuned to reflect only the desired frequencies required for laser cooling and AI. (a) Absorption spectrum of  $^{87}\text{Rb}$  D<sub>2</sub> line, (b) Idealised reflection response of the fibre-Bragg grating (c) Required frequencies for laser cooling and AI. Diagram adapted from [118].

The 1560nm seed laser is split along the two branches shown in figure 6.2. The upper branch handles frequency locking and the lower is for amplification and delivery to the system. In the upper branch the light undergoes Second-harmonic generation (SHG) converting it from 1560 nm to 780 nm before entering a homemade modulation transfer spectroscopy (MTS) setup. In the lower branch light is modulated by an EOM with two highly phase coherent, clean RF frequencies, the process of generating these frequencies is described in section 6.2. The light is then reflected from two fibre-Bragg gratings before being amplified to 1W by an EDFA. The light is then frequency doubled before entering a fibre AOM so that the light can be pulsed and delivered to the system.

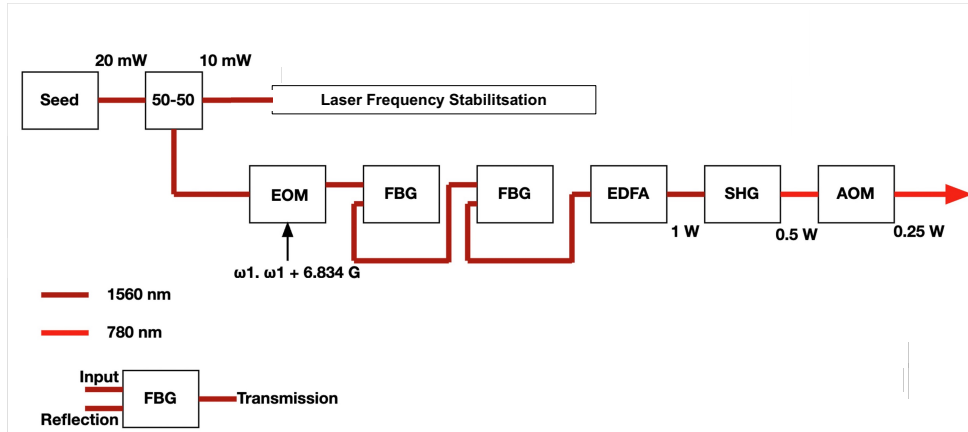


Figure 6.2: Fibre Bragg Grating Laser System Design.

The reflection bandwidth of the fibre-Bragg grating is not as idealised as implied by Figure 6.1. To achieve optimal suppression of the carrier frequency, the grating's passband must be at least 10 GHz away from the carrier. This relies on using relatively high RF modulation frequencies (12 GHz and 18.8 GHz). If the gratings are not tuned appropriately, the carrier will not be suppressed and so will appear prominently in the optical spectrum. Furthermore, the wide bandwidth of the FBG (44 GHz) makes it impossible to filter second harmonics of the drive frequencies. Moreover, sufficient RF power is also required to shift adequate power into the first order sidebands for seeding the EDFA ( $\geq -20$  dBm). Additionally, the higher frequency requirements mean RF components are more costly and less readily available.

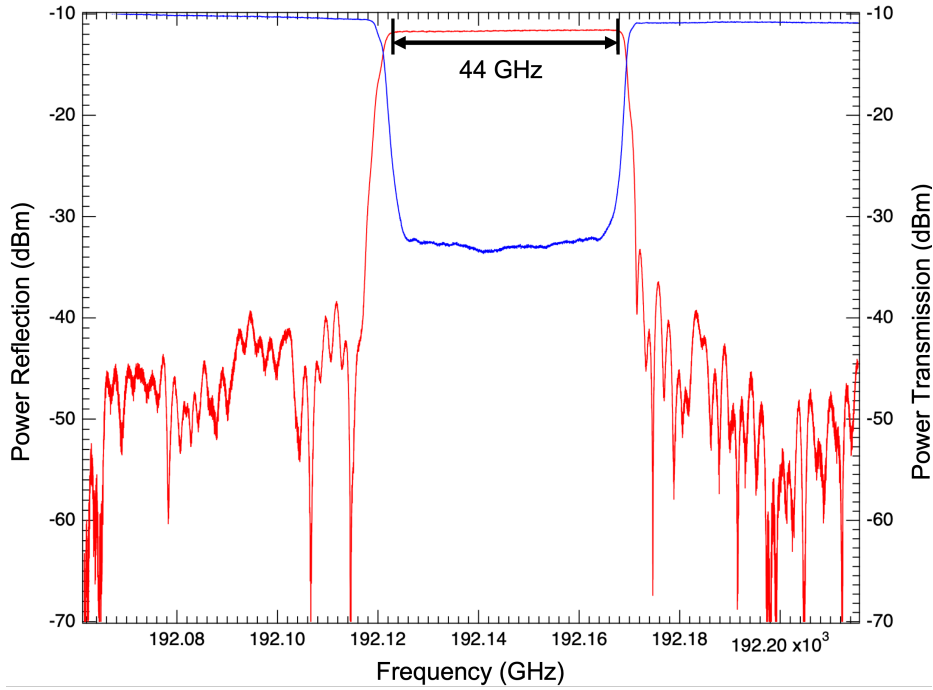


Figure 6.3: Characterisation of TeraXion 1560 nm fibre-Bragg grating. Bandwidth measured to be 44 GHz, Transmission (blue), Reflection (red) [121].

## 6.2 RF Generation

Figure 6.4 presents the RF design for generating two coherent RF frequencies with a separation of 6.834 GHz. These RF frequencies are applied to the EOM producing two optical frequencies with the same separation. This frequency separation enables stimulated Raman transitions to be driven in  $^{87}\text{Rb}$ . The design's agility is achieved by controlling an AD9914 chip with a SPI bus which defines the separation of the optical frequencies. The chip supports different modes, single-profile mode is chosen for fixed frequency measurements while the ramp generator chirps the laser frequency during interferometry.



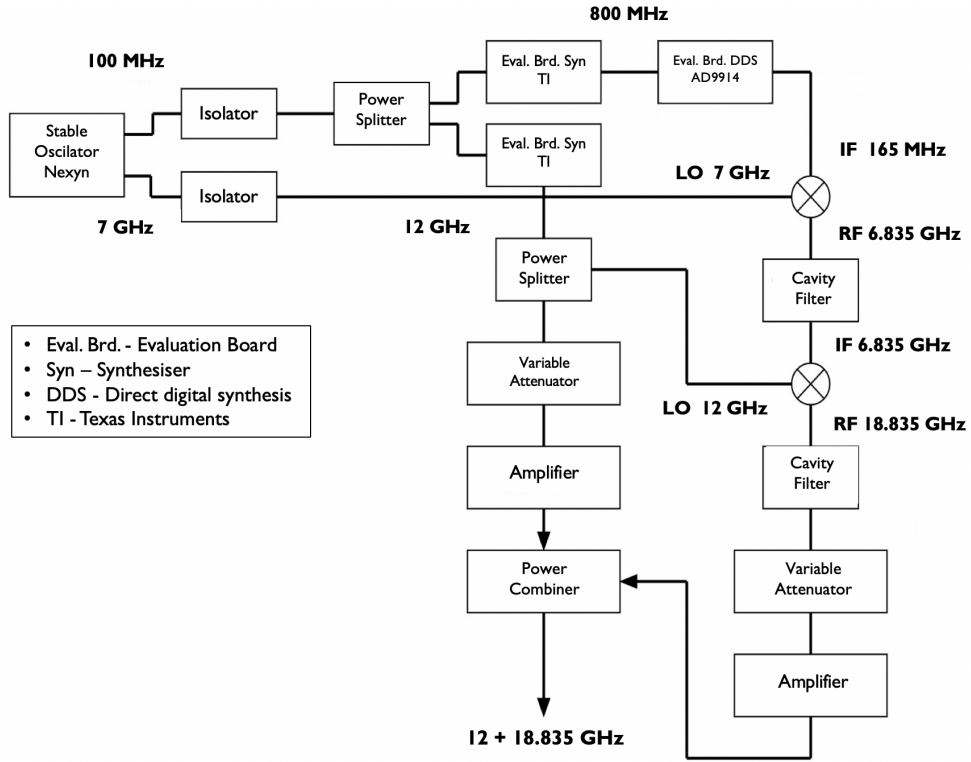


Figure 6.4: Schematic showing RF circuit for driving the EOM.

### 6.3 Spectral Purity

The 12 GHz and 6.8 GHz RF signals are upmixed to generate the desirable 18.8 GHz frequency. However, this process generates many other prominent undesirable frequencies in the optical spectrum (figure 6.5). Efforts were made to reduce these undesirable frequencies by tweaking drive powers into the mixer and subsequent amplifier but were unsuccessful.

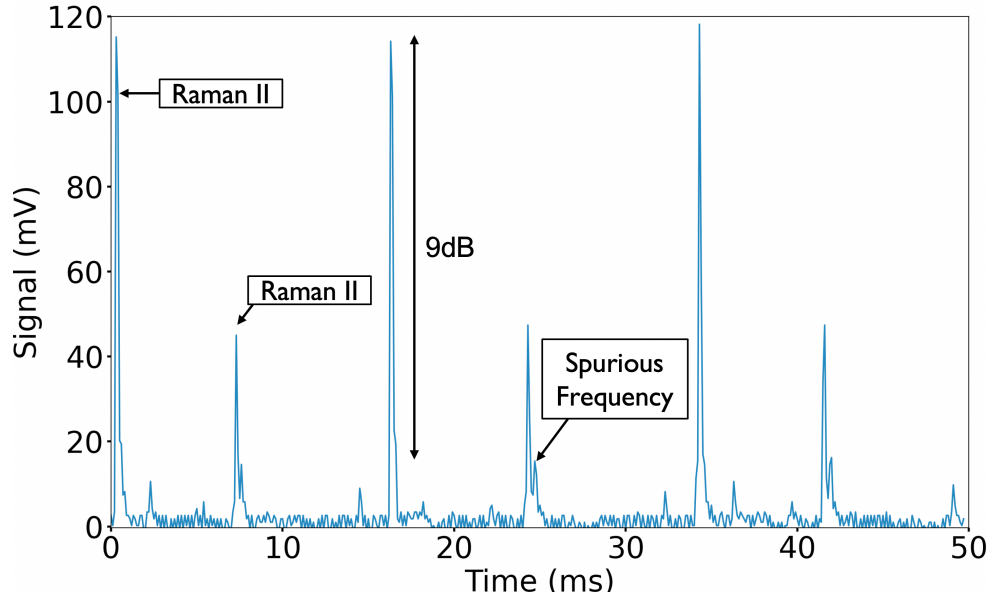


Figure 6.5: Optical spectrum generated without filtering mixer output. The spectrum is shown on a Fabre-Perot interferometer with Free-Spectral Range of 1.5 GHz.

Therefore, a cavity filter is placed after the mixer to pass only the desirable 18.8 GHz frequency, the final output RF spectrum shown in figure 6.6. The 6.834 GHz signal is regenerated after amplification and combining of the 12 GHz and 18.8 GHz signals. However, this is well filtered by the fibre-Bragg gratings in the optical domain.

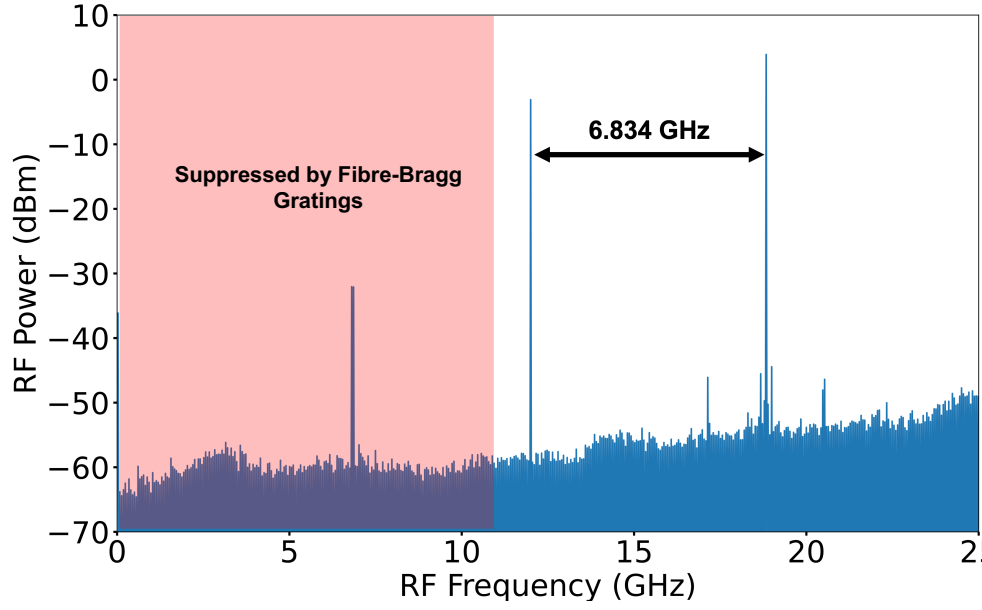
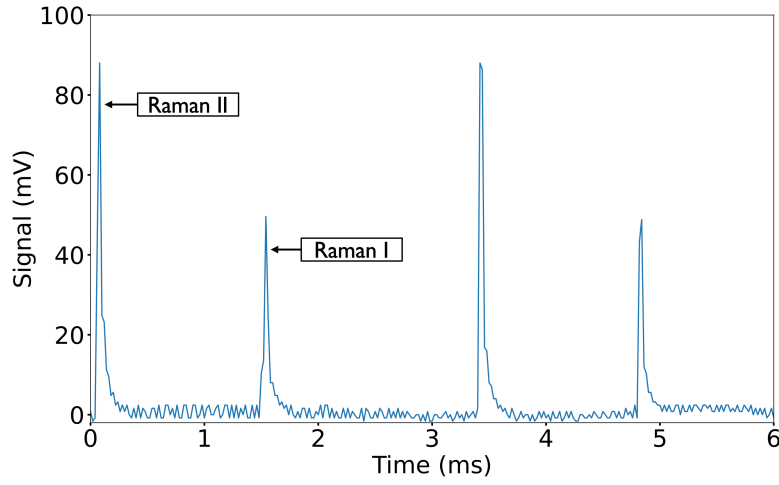
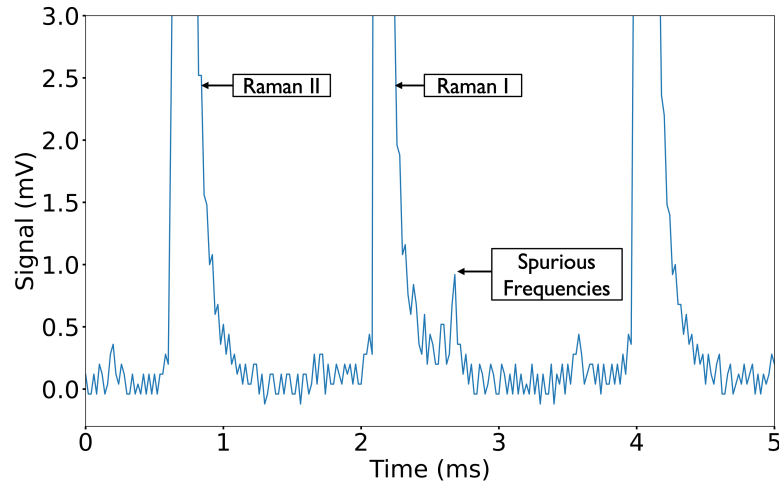


Figure 6.6: The RF spectrum is measured at the final combiner with a cavity filter after the high-frequency mixer. The 6.834 GHz RF frequency is negligible and is further suppressed by FBGs in the optical domain.

Figure 6.7a shows the improved optical spectrum achieved by modulating the EOM with the RF spectrum in figure 6.6. By averaging multiple shots of the Fabre-Perot readout spurious signals emerge indicating a 20 dB suppression of undesirable frequencies.



(a) Full Scale Spectrum



(b) Small Scale, averaged 16 times to distinguish spurious frequencies from noise.

Figure 6.7: Fabre-Perot interferometer spectrums at 780nm (Free Spectral Range 1.5 GHz) characterising spectral purity.

To explore the origins of the spurious frequencies at 780nm the optical spectrum was measured at 1560 nm following the EDFA. For testing purposes, a single frequency was applied to the EOM. Figure 6.8 shows the results of applying a clean 12 GHz modulation frequency to the EOM. The most prominent peak is the desirable frequency, the second most prominent the doubling

of this and the third is the the carrier frequency which is suppressed by the fibre-Bragg gratings.

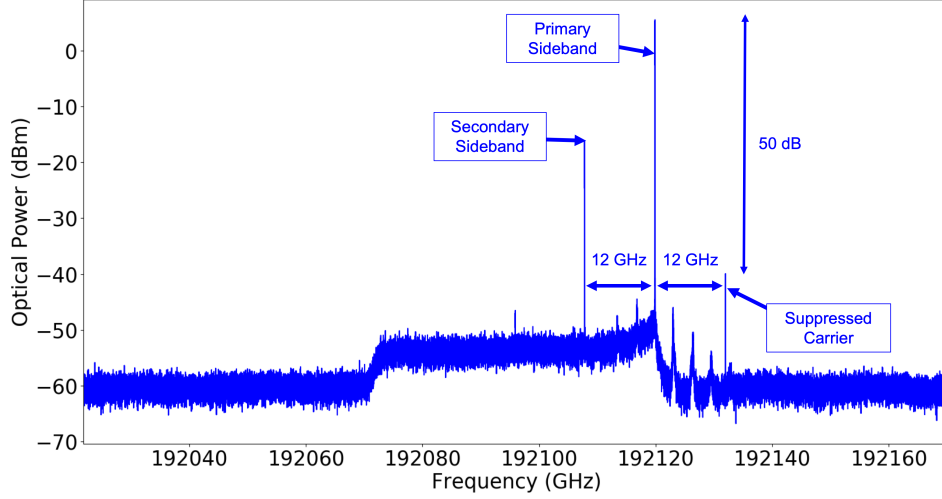


Figure 6.8: 1560 nm Optical Spectrum post-EDFA with single-tone 12 GHz modulation applied to EOM.

After this, two-tone modulation was performed with 12 GHz and frequencies around 18 GHz; the RF sources were very clean to ensure only the effects of two-tone modulation would be observed. Figure 6.9 shows the results of this testing. The origins of the spurious frequencies were identified by changing the secondary frequency to 18, 19 and 20 GHz. These additional frequencies do not limit this demonstrator system but highlight the limitations of the EDFA.

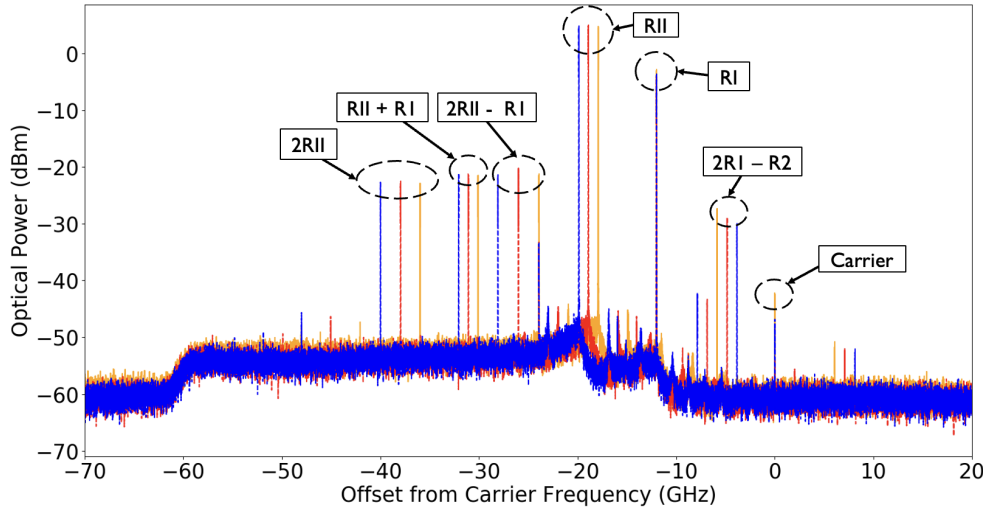


Figure 6.9: Undesirable intermodulation products observed at 1560nm post EDFA with two-tone modulation. A clean 12 GHz signal is combined with a clean 18 (yellow), 19 (red) or 20 (blue) GHz signal and are applied to the EOM before passing through two fibre-Bragg gratings. The optical spectrum is monitored post EDFA. RI and RII correspond to Raman I and Raman II respectively.

## 6.4 Power Performance

For short Raman pulses certain power requirements are necessary. Achieving a high enough output power relies on the performance of the frequency doubler crystal and EDFA. The conversion efficiency of the second harmonic generation process is presented in figure 6.10. At 1W input power, the performance is not fully optimised and after careful temperature optimisation of the crystal a peak efficiency of 43% was achieved. The EDFA can amplify up to 2W, but the system is operated at 1W to ensure longevity of the frequency doubling crystal. In the later stage of the PhD, no power increase was observed at 2W, indicating degradation of the doubler.

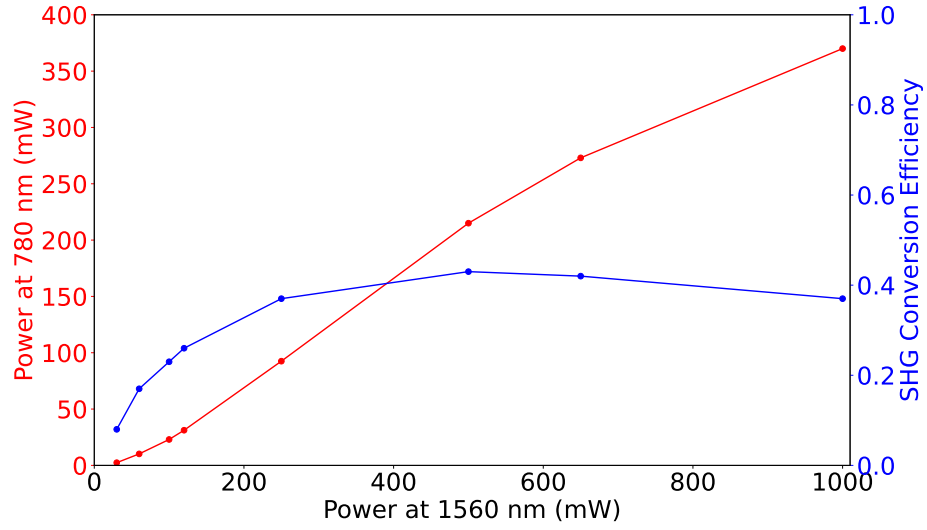


Figure 6.10: Efficiency of second-harmonic generation (SHG) process converting 1560 nm to 780 nm light for variable EDFA input power.

The amplitude extinction ratio of the system was measured by comparing the power measured when the final AOM is shuttered on and off by a TTL signal. At 1W EDFA output power the extinction ratio at 780 nm is measured to be 54 dB although this degrades at lower output powers. The power after the final AOM was monitored for 15 hours to investigate power stability. A mean power of 180 mW was measured with a relatively typical fluctuation of roughly 1% over this period.

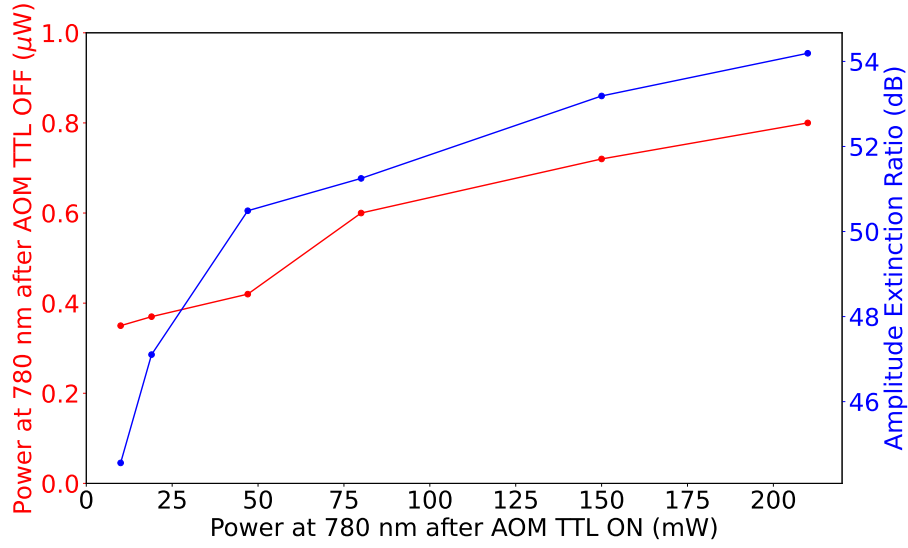


Figure 6.11: System amplitude extinction ratio for variable EDFA output power.

## 6.5 Further Testing

Additional tests explored potential system improvements using a 10 GHz bandwidth fibre-Bragg grating. This grating has a narrower passband and aims to further reduce unwanted frequencies, achieving 25 dB carrier suppression like the previously implemented grating. Figure 6.12 demonstrates the benefits of incorporating this grating. The red spectrum represents the project's predominant configuration with two broadband gratings (44 GHz) in series. Adding the 10 GHz narrowband grating before the EDFA resulted in the blue spectrum. The spectrums shown in figure 6.12 are monitored pre-EDFA.



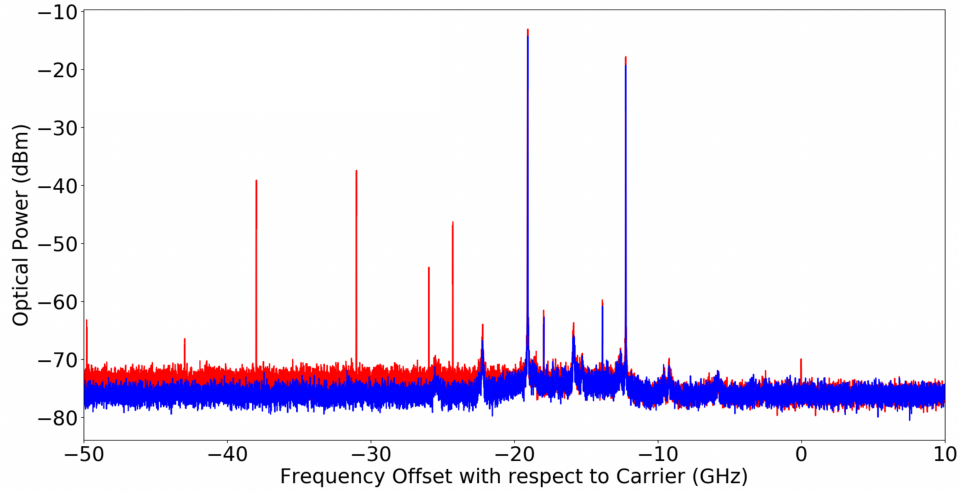


Figure 6.12: Comparison before (red) and after (blue) adding the new narrowband 10 GHz FBG. The additional FBG is added prior to EDFA where the spectrum is measured.

The cleaner spectrum (blue) is then passed through the EDFA with its typical 1W power level. However, the EDFA introduces mixing, generating spurious frequencies with a 6.8 GHz spacing. To suppress these frequencies, the 10 GHz grating is placed after the EDFA. Unfortunately, the grating's damage threshold of 500 mW prevents operating the EDFA at 1W power. Although the spectrum improves (figure 6.13), the final output power is too low due to the quadratic power dependence of the frequency doubler. The optical spectrum is monitored at 780nm with an extinction ratio of 21dB, similar to the previous implementation. The spurious frequencies are believed to result from the frequency summation effect of second harmonic generation (SHG). Further improvement involves exploring optical filtering at 780nm, depending on the availability of suitable gratings.

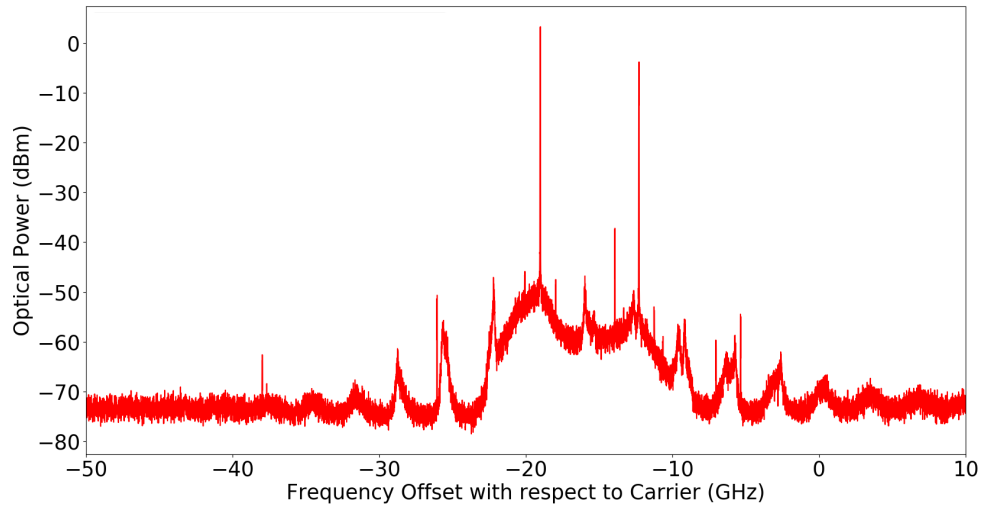


Figure 6.13: 1560nm optical spectrum after EDFA inputting ‘red’ spectrum from figure 6.12 into EDFA. Output spectrum is monitored with 300 mW EDFA output with narrowband fibre-Bragg Grating post EDFA on the 1% port of a 99:1 splitter.

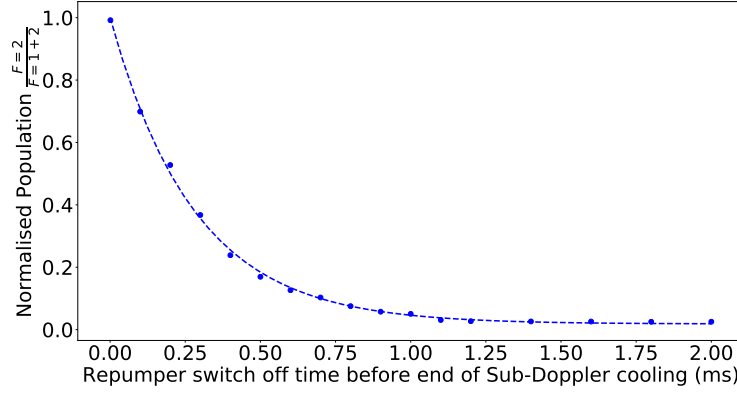
## Chapter 7

# Results

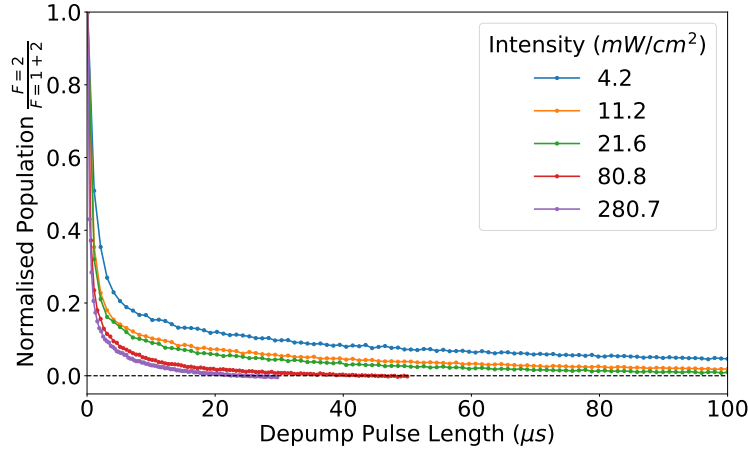
After generating a  $^{87}\text{Rb}$  MOT and developing the necessary tools for high-bandwidth operation, stimulated Raman transitions are performed optimising atom optics for the interferometer sequence.

### 7.1 State Initialisation

Towards the end of the sub-Doppler phase, atoms are allowed to transition into the ground state ( $5^2\text{S}_{1/2}$   $F = 1$ ) by turning off the repumper. The process is characterised in figure 7.1a, where fitting to an exponential decay relation yields a time constant of  $\tau = 0.281 \pm 0.005$  ms. This motivates switching the repumper off 1.2 ms before the end of sub-Doppler cooling. This results in a residual population of roughly 1-2% in  $F = 2$ . Throughout the PhD, this method was employed to prepare atoms in the  $F = 1$  state.



(a) Switching off repumper near the end of the 3 ms sub-Doppler cooling period.



(b) Performance of depump pulse for variable power.

Figure 7.1: Depopulation of  $F = 2$  state. a.) Switching off repumper near end of sub-Doppler cooling b.) Depump pulse resonant with  $F = 2 \rightarrow F = 2'$  transition.

A more optimal preparation method involves driving the  $F = 2 \rightarrow F = 2'$  transition. However, due to bandwidth limitations of the AOM, it is not possible to achieve the required 266 MHz shift. To overcome this, an external signal generator and RF switch were used to drive this transition with the vertical beam. By driving this transition without the repumper, atoms are directed into the  $F = 1$  state. This “depumping” mechanism takes around 50

$\mu\text{s}$  and offers a cleaner state preparation compared to turning off the repumper before the end of sub-Doppler cooling. Another advantage is the decoupling of state preparation from the sub-Doppler cooling period, allowing independent optimisation of each process.

## 7.2 Co-Propagating Configuration

Time was dedicated to probing the co-propagating transition to gain familiarity with Raman transitions. This transition is Doppler insensitive with a width inversely proportional to the pulse duration. By operating at low power and increasing the pulse duration to  $20\ \mu\text{s}$ , the pulse becomes very selective with a width of  $\sim 40\ \text{kHz}$ . This allows easy resolution of the peaks corresponding to different transitions. Adjusting the compensation coils suppressed additional peaks by aligning the bias field with the Raman beam. Before continuing, an important distinction should be made:

- *Normalised population transfer* compares the atom number in  $F = 2$  to the total atom number in  $F = 1 + 2$
- *Relative population transfer* takes into account the distribution of atoms across the  $3m_f$  states, with our laser addressing only  $m_f = 0$ .

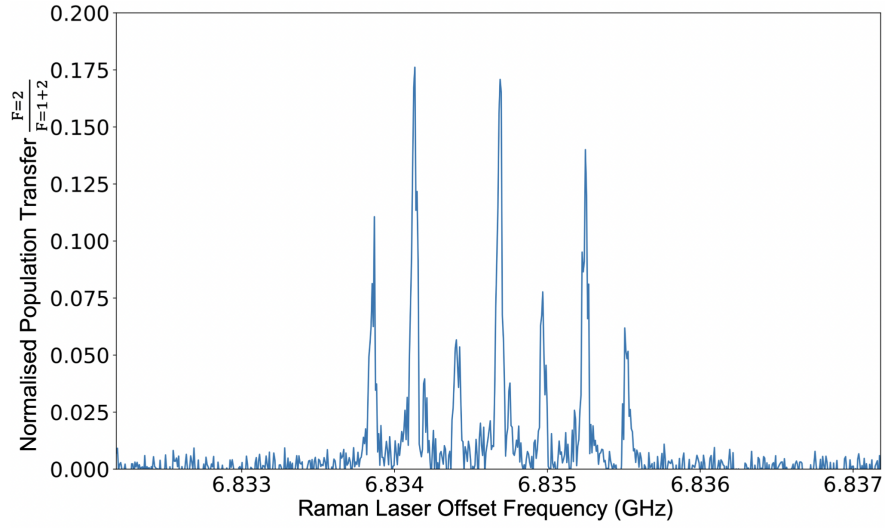


Figure 7.2: Co-Propagating Raman Spectroscopy with poorly compensated ambient fields,  $\tau_\pi = 20 \mu\text{s}$ .

After improving the compensation condition, the Raman laser was operated at high power with a  $3 \mu\text{s}$  pulse. Due to the absence of optical pumping a large 4.7G bias field was employed to ensure complete separation of the  $3m_f$  states. The specific value of the bias field was determined by analysing the peak positions in Figure 7.3 and fitting the data using three sinc-squared functions with independent amplitude, width, and offset parameters.

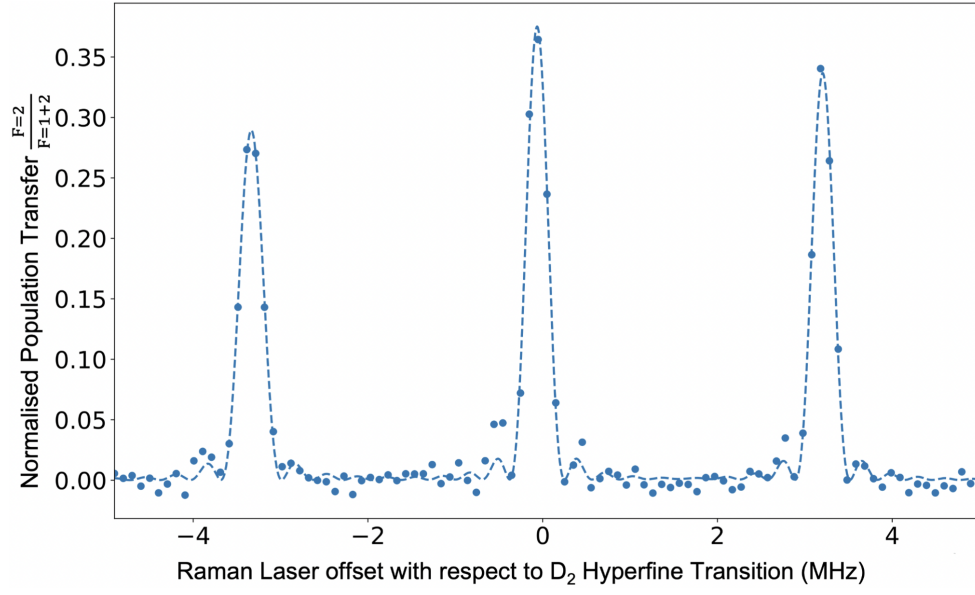


Figure 7.3: Co-propagating Raman spectroscopy with a  $3\mu\text{s}$  pulse. A 4.7G bias field ensures  $m_f$  states are well separated.

To demonstrate coherence of the system co-propagating Rabi oscillations are performed. Figure 7.4 shows the results of this for variable compensation condition. The poor compensation condition corresponds to a spectroscopy scan similar to that in figure 7.2. As one can see, improving compensation increases both peak transfer efficiency and coherence.

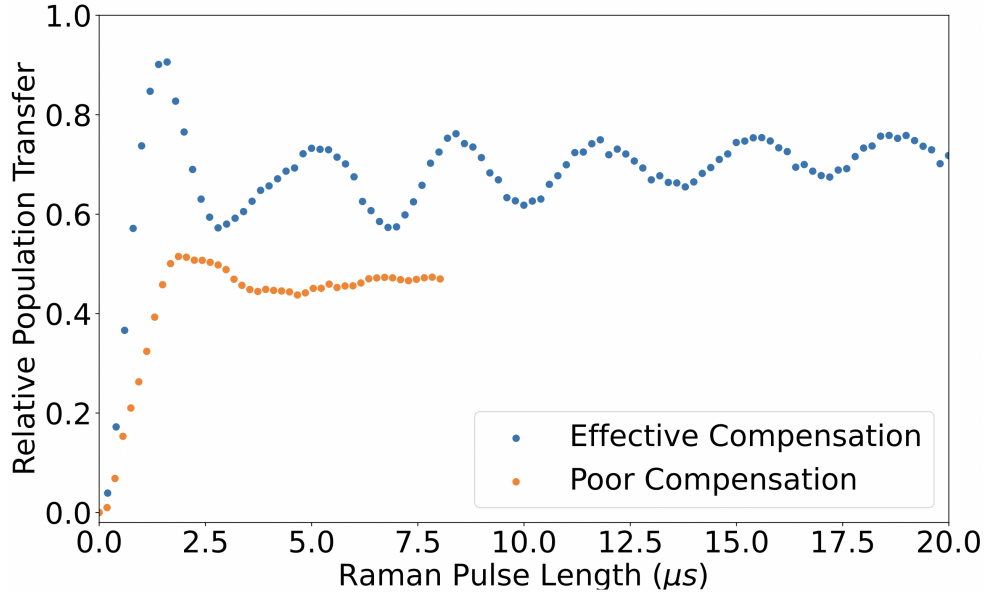


Figure 7.4: Effect of bias field alignment on Co-Propagating Rabi Oscillation.

### 7.3 Counter-Propagating Configuration

After probing the co-propagating transition, the system was reconfigured driving the counter-propagating transition. Raman spectroscopy was then performed to determine suitable parameters for an initial interferometry demonstration. To break the Raman degeneracy condition a launch velocity of  $0.25 \text{ ms}^{-1}$  is required. The presence of two peaks is a consequence of the opposite effective wavevectors,  $\pm k_{\text{eff}}$ , which both satisfy the Doppler-sensitive resonance condition of the stimulated Raman transition. Occasionally, a reduced co-propagating peak appears between the counter-propagating peaks, which may be due to polarisation impurity or overdriving the Raman transition. Figure 7.5 shows a scan over a relatively wide frequency range, showing



all three  $m_f$  states.

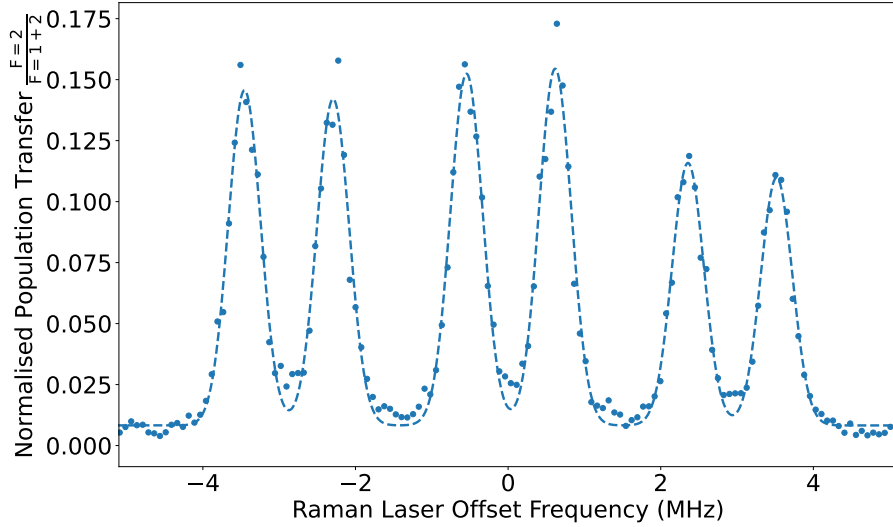


Figure 7.5: Counter-propagating Raman spectroscopy scan over all three  $m_f$  states. Atoms are launched at a velocity of  $0.25 \text{ ms}^{-1}$  with a bias field of 4.2 G and a pulse length of  $2.5 \mu\text{s}$ .

The population transfer to  $F = 2$  is normalised based on the total number of atoms in the  $F = 1$  and  $F = 2$  states. It is observed that 37% of the atoms occupy the central  $m_f = 0$  state. To prevent overlapping states, a bias field of approximately 4.2 G is utilised. However, when using pulses shorter than  $2.5 \mu\text{s}$ , the Raman degeneracy is not sufficiently broken, as depicted in Figure 7.6. This broadening of the pulse is caused by reduced selectivity in the Raman transition. As the pulse length increases, the width is limited by the Doppler effect. This indicates a cloud temperature of around  $25 \mu\text{K}$ , which aligns with thermal expansion measurements. Consequently, a pulse length of  $2.5 \mu\text{s}$  provides a good compromise between population transfer and

state separation. It should be noted that the undershooting observed in the fit in Figure 7.5 is a result of under-sampling the peaks. This becomes evident when comparing with Figure 7.6, where the fit quality is superior.

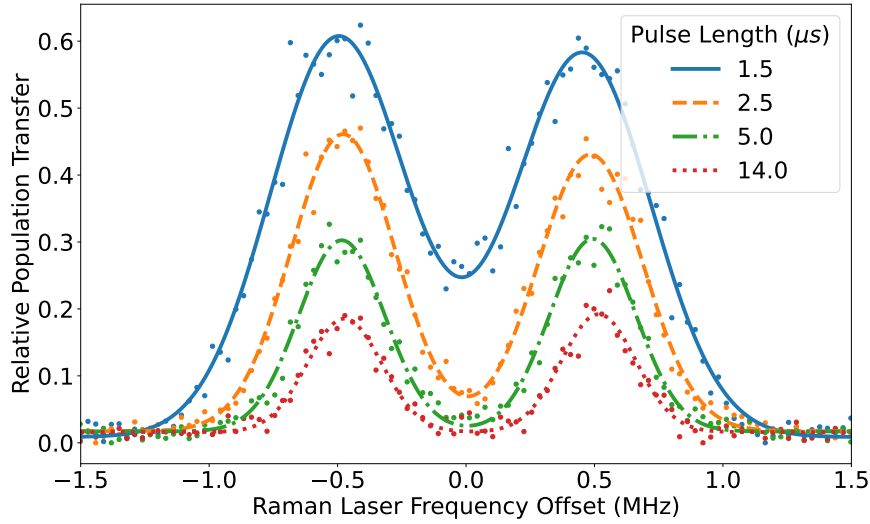


Figure 7.6: Raman spectroscopy sideband scan over  $m_f = 0$  state in the counter-propagating Raman configuration for variable pulse length.

### 7.3.1 Breaking Raman Degeneracy

To break Raman degeneracy, atoms require an initial velocity. By varying the launch speed of the moving molasses, a Raman sideband spectroscopy scan is performed to determine the necessary velocity kick. Figure 7.7 displays sample scans for different launch velocities, with a velocity of  $0.2 \text{ ms}^{-1}$  needed for peak separation. Figure 7.8 provides useful information on spectrum appearance at different launch velocities needed for identifying the required Raman frequency offset for the first interferometer pulse.

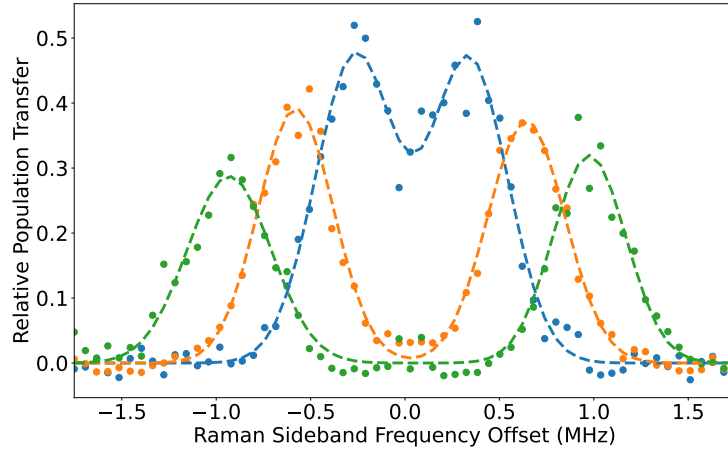


Figure 7.7: Raman spectroscopy sideband scans for variable launch velocities. Mean velocity ( $\text{ms}^{-1}$ ) at time of  $3 \mu\text{s}$  Raman pulse: 0.15 (blue), 0.24 (orange), 0.38 (green).

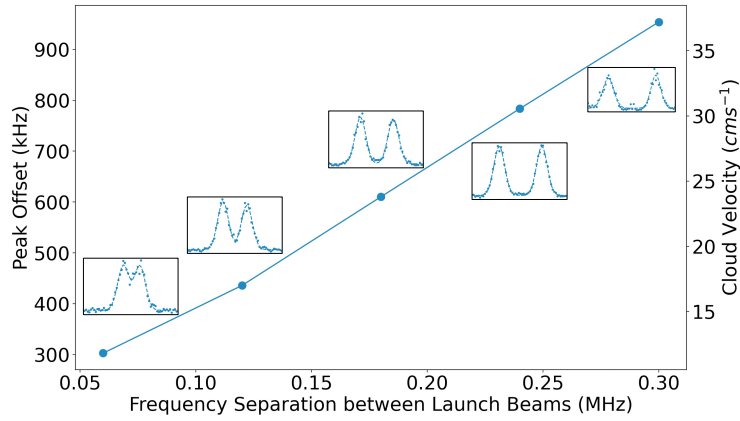


Figure 7.8: Raman resonance offset with respect to  $\text{D}_2$  hyperfine splitting for variable launch speed. Visual representation of spectroscopy scans is shown inset.

### 7.3.2 Rabi Oscillations

By varying the duration of the Raman pulse, counter-propagating Rabi oscillations can be observed. The system is configured with the Raman sideband frequency fixed to the  $-\mathbf{k}_{\text{eff}}$  resonance with the Raman pulse applied 1.5 ms

after completing sub-Doppler cooling. The initial part of oscillation is fitted using a damped cosine function (equation 7.1) allowing for extraction of the peak population transfer and its corresponding pulse length.

$$N_{a,\text{Rabi}} = \frac{1}{2}(1 - e^{-\gamma_R^2 \tau^2} \cos(\Omega_R \tau)) \quad (7.1)$$

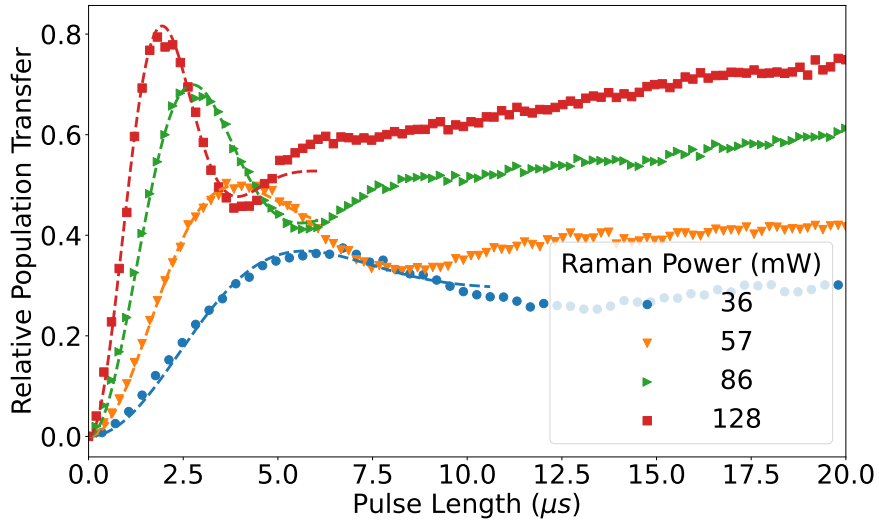


Figure 7.9: Counter-propagating Rabi oscillations for variable total Raman power.

Rabi oscillations were performed at various total Raman powers, and the corresponding peak transfers and Rabi frequencies were determined. Using known experimental parameters, a prediction for the Rabi frequency can be made based on equation 4.9, assuming a 1:2 power ratio between Raman I and II frequencies. The experimental Rabi frequencies were extracted from the Rabi oscillation data shown in figure 7.9. Figure 7.10 illustrates the relation-

ship between total Raman power and Rabi frequency, demonstrating a strong linear connection. The similarity between the experimental data and the model indicates good knowledge of the Raman beam size ( $2\sigma_{\text{RAMAN}} = 4 \text{ mm}$ ) and suggests that the combined effects of velocity and spatial inhomogeneities have not significantly influenced the  $\pi$  condition.

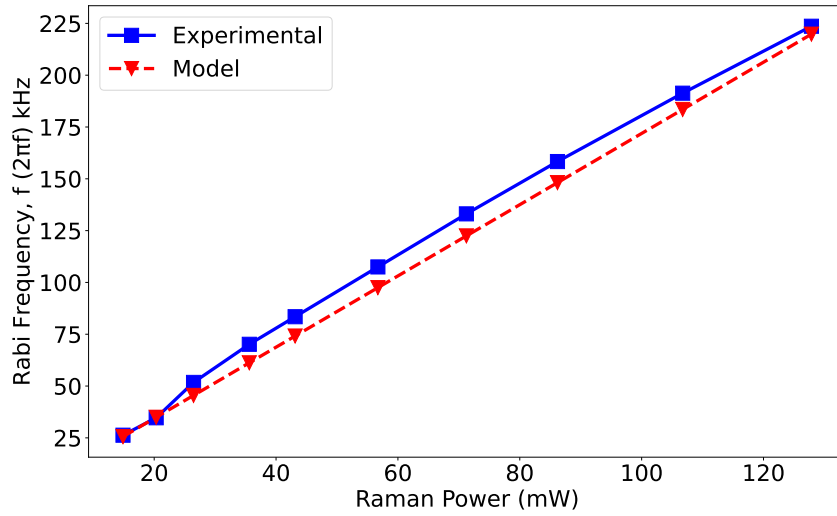


Figure 7.10: Experimental Rabi frequencies extracted from the Rabi oscillations in Figure 7.9 are compared to theoretical values. The power scaling of Rabi Frequency is evaluated and a prediction for the Rabi frequency is derived using equation 4.9 and known experimental parameters.

The peak population transfer is plotted against the predicted Rabi frequency and compared to the theoretical model described in section 2.5. The population transfer is modelled based on a cloud radius of 0.5 mm at a temperature of 25  $\mu\text{K}$ , with a Raman beam radius of 2 mm. The model is simulated for temperatures of 10  $\mu\text{K}$  and 50  $\mu\text{K}$  to assess its sensitivity and validate the temperature determination using thermal expansion. Figure 7.11 displays

the results, confirming the validity of the model and the small beam size chosen. The model shows strong agreement, although values at higher Rabi frequencies ( $f > 200$  kHz) are slightly overestimated by approximately 1 – 2% due to slight peak overlap caused by the Raman degeneracy issue.

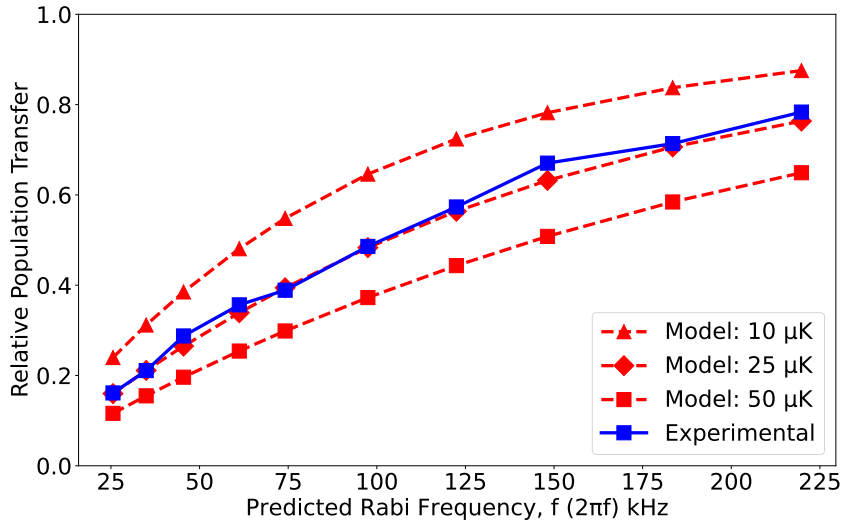


Figure 7.11: Relative population transfer modelled for different cloud temperatures with comparison to experimental data.

## 7.4 Interferometry

After constructing the necessary foundation a Mach-Zehnder like pulse sequence is performed. Initially atoms are prepared in the MOT by switching on the quadrupole field, cooling and repumper beams. Then simultaneous launching and sub-Doppler cooling commence, towards the end of this period the repumper beam is switched off. Following this the DDS chirps the laser frequency and a Mach-Zehnder  $\frac{\pi}{2} - \pi - \frac{\pi}{2}$  pulse scheme is performed.

Finally a detection pulse reads the  $|F = 2\rangle$  state. Figure 7.12 illustrates performance for variable  $T$ . When  $k_{\text{eff}}g = 2\pi\alpha$ , the phase shift is cancelled for all  $T$ . Local gravity is then determined by identifying the stationary point where fringes of variable  $T$  have the same local minima which occurs around  $\alpha = 25.1 \text{ MHz s}^{-1}$ . Furthermore, it is important to consider the relationship between the drop time and the scanned phase within the system. As the drop time increases, a larger phase is scanned, making the system more sensitive to smaller changes in the chirp rate of the laser frequency. This heightened sensitivity manifests as significant population transfer for slight variation in chirp rate.

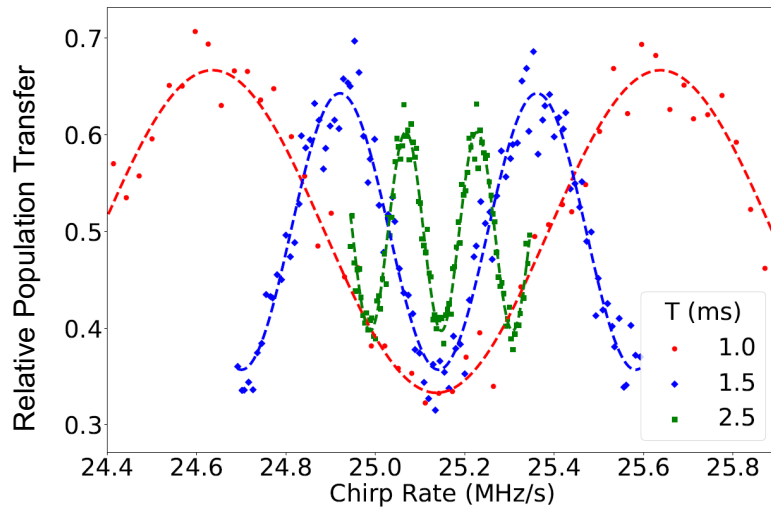


Figure 7.12: Interference fringes in the output state population ratio of Mach-Zehnder sequences with different free-evolution time  $T$  between Raman pulses. Scanning the chirp rate of the Raman beam creates a periodic change in the state population ratio which is fitted with a cosine function.

Tests were conducted to examine the impact of vibrations on the instrument.

The results, as outlined in 2.9.2, indicate that the instrument exhibits suppressed sensitivity to seismic noise which is attributed the short  $T$  time used at high-bandwidth. A comparison of sensitivity to vibrations is shown in Figures 7.13a and 7.13b for  $T$  times of 2.5 ms and 5 ms, respectively. These figures clearly demonstrate that longer  $T$  times lead to a less distinct interference fringe unless vibration isolation measures are implemented. However, it is worth noting that there are no significant differences observed between the results with and without vibration isolation for  $T$  times below 3.5 ms. For clarity the vibration isolation significantly suppresses frequencies typically between 1-100 Hz which will, as demonstrated, significantly degrade the performance of a long  $T$  time instrument.

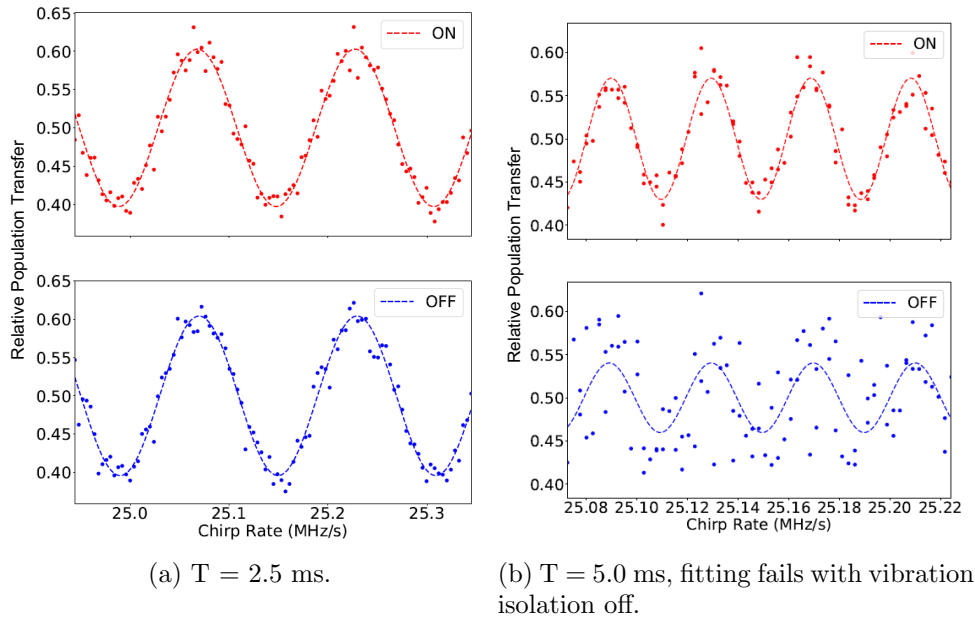


Figure 7.13: Effect of vibration isolation on fringe visibility for variable  $T$  time.



Experimental tests were conducted to investigate enhancement in sensitivity achieved through averaging multiple measurements. The results, depicted in Figures 7.14 and 7.15, highlight the improvement in sensitivity achieved by performing multiple scans. Specifically, the sensitivity is enhanced to  $\mu\text{g}$  levels, as highlighted in Figure 7.15, which follows the expected scaling behaviour characterised by  $t^{-\frac{1}{2}}$ .

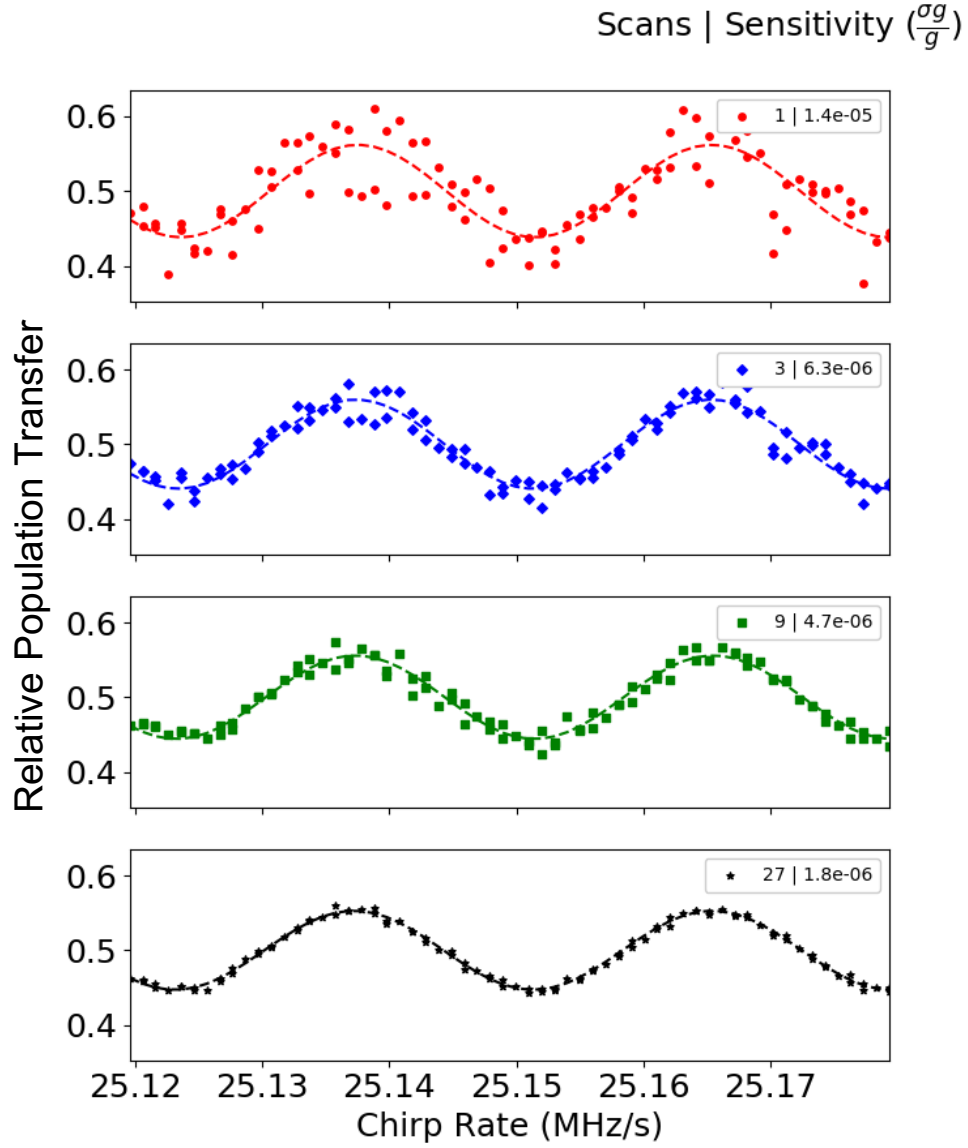


Figure 7.14: Multiple fringes were averaged to highlight the reduction in noise and improvement in accuracy, note measurement is performed with  $T = 6$  ms.

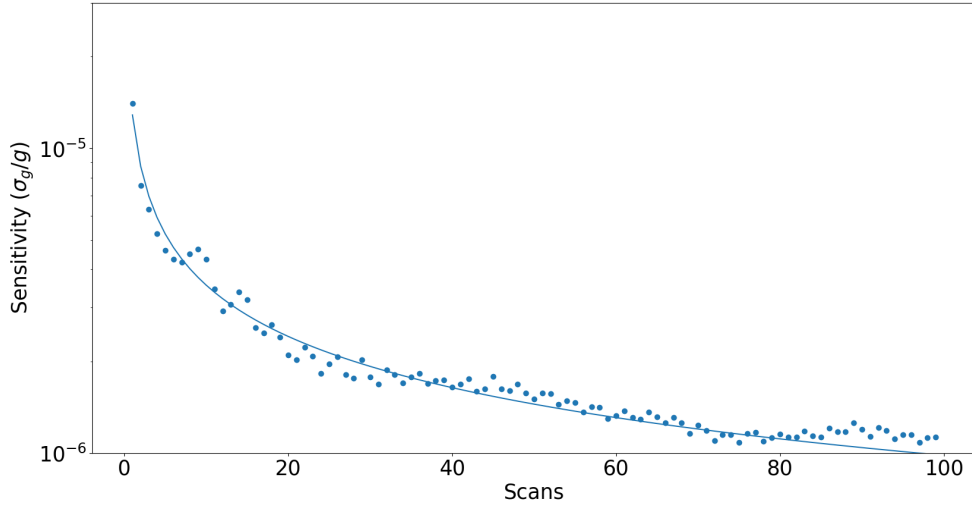


Figure 7.15: Averaging down sensitivity for multiple fringes as highlighted in figure 7.14. Data is fitted to expected  $t^{-\frac{1}{2}}$  scaling.

Although the system primarily focuses on short interrogation times due to the high-bandwidth emphasis, there is still interest in increasing the interrogation time. A decrease in contrast is observed for increasing interrogation time as shown in Figure 7.16. This contrast loss is believed to be caused by several factors: the small Raman beam, high cloud temperature coupled with cloud expansion and pressure-induced collisional losses during the interferometer. Concerns are also raised regarding the potential overlap of  $m_f$  states for increasing free-falling time. These areas will require further theoretical and experimental investigations to make further improvements to system performance. While this work focuses very much on high-bandwidth operation it is desirable to also push to lower-bandwidth as the device would gain real application flexibility with dynamic bandwidth.

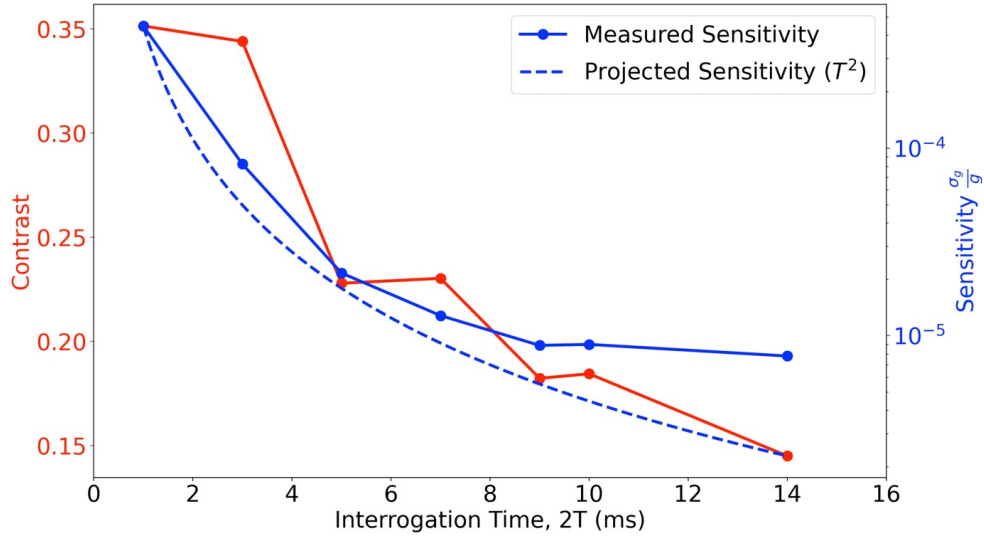


Figure 7.16: The interferometer contrast decreases with longer interrogation time (red). The measured sensitivity (blue points) and projected sensitivity (blue dashed) are also plotted.

## 7.5 Noise

This section addresses sensitivity limitations and suggests potential avenues for improvement using the framework outlined in [122]. It begins by examining key sources of phase noise and proceeds to estimate systematic errors in gravity measurement. Noise in atom interferometers can be broadly classified into two categories: those inherently quantum in nature and those arising from practical and environmental constraints. In atom interferometers with uncorrelated atoms, the fundamental noise limit is dictated by quantum projection noise (QPN) or atom shot noise. However, sensitivity is often constrained by other more dominant sources of noise, such as detection noise, seismic vibrations and Raman intensity among others.

### 7.5.1 Atom Shot Noise

At the interferometer output atoms exist in a superposition of two hyperfine states namely  $|F = 1, m_F = 0\rangle$  and  $|F = 2, m_F = 0\rangle$ . For non-squeezed states measuring the atomic populations is subject to quantum projection noise (QPN) limiting the instrumental sensitivity. This atom shot noise leads to a standard deviation uncertainty in the measured phase difference of  $\sigma_{\Delta\Phi} = \frac{1}{\sqrt{N}}$ . Substituting the relation for phase ( $\Delta\Phi = k_{\text{eff}}gT^2$ ) the uncertainty can be re-expressed as in equation 7.2.  $T$  is the time interval between Raman pulses and  $k_{\text{eff}}$  is effective wave vector of the Raman laser. In our experiment about  $5 \times 10^6$  atoms complete the interferometer with  $T = 2.5$  ms giving an ultimate sensitivity of  $\sigma_g \approx 0.45 \mu\text{g}$ .

$$\frac{\sigma_{\Delta\Phi}}{\Delta\Phi} = \frac{\sigma_g}{g} = \frac{1}{k_{\text{eff}}gT^2\sqrt{N}}. \quad (7.2)$$

### 7.5.2 Photon Shot Noise

The discrete nature of photon counting during atomic state readout manifests as shot noise. Reaching the quantum projection noise limit requires at least one photon to be detected per atom.  $n_{\text{photon}} = \frac{R_{\text{scatt}}\tau A}{4\pi}$  denotes the number of photons hitting the detector per second per atom where  $R_{\text{scatt}}$  is the photon scattering rate,  $\tau$  is the detection pulse length and  $A$  is solid angle of the detection window. Even for a fairly low fractional solid angle of 1% ( $A = 0.13$ ) 30 photons per atom are detected with a 150  $\mu\text{s}$  pulse,  $I = 5I_{\text{sat}}$  and on-

resonance detection. This means that the photon shot noise can be neglected as its contribution is less dominant than atom shot noise.

### 7.5.3 MOT Fluctuations

In the system, atoms in the  $|F = 2, m_F = 0\rangle$  state undergo single state detection. Traditionally, a two-state normalisation is performed by measuring the total number of atoms. However, due to the limited readout speed of the camera, this approach is not tractable. Consequently, phase noise will occur due to fluctuations in MOT atom number. Given  $\frac{S}{N} = \frac{AC}{\sigma_x}$  where AC is the fringe amplitude and  $\sigma_x$  is the variation in population transfer. Assuming  $\sigma_x = 2AC \cdot u$  where  $2AC$  is the peak to peak amplitude and  $u$  is the fractional uncertainty on MOT atom number,  $\frac{S}{N} = \frac{1}{2u}$ .

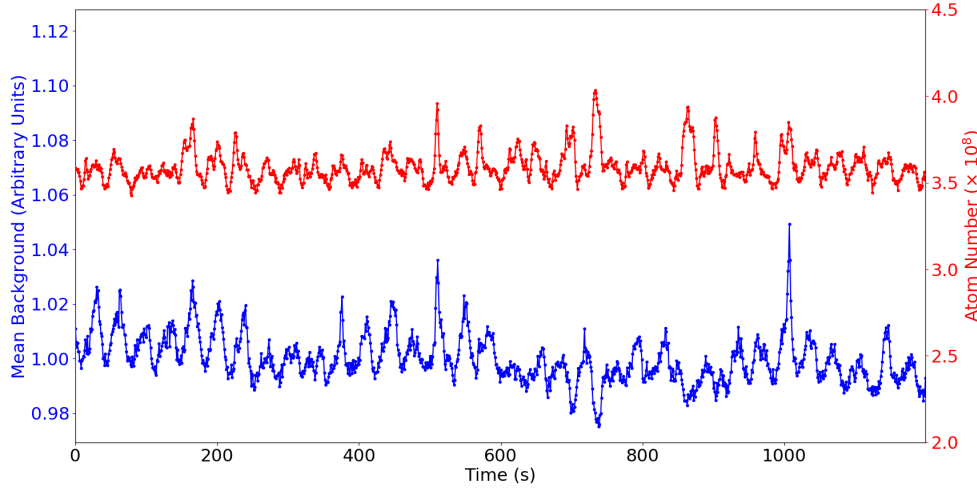


Figure 7.17: MOT fluctuations (red) and background light level (blue).

Figure 7.17 shows the MOT fluctuations over a period of roughly 20 mins.

Due to computational delay in data acquisition fringe scans will usually take a few minutes meaning a rough fluctuation in MOT atom number of  $u = 0.04$ . This results in  $(\frac{S}{N})^{-1} = \sigma_{\Delta\phi} = 80 \text{ mrad}$  and ultimately a noise of  $80 \text{ }\mu\text{g}$ . The correlation between atom number fluctuations and background light level is indicative of laser power fluctuations being responsible for MOT variations coupling into the measurement.

#### 7.5.4 Raman Laser Intensity Noise

Raman laser intensity stabilisation is not present in our experiment which means fluctuations in intensity change the Rabi frequency and result in phase noise. After the first  $\pi$  pulse the variance of the atomic inversion  $W$  is

$$\sigma_W = \sigma_\Omega \tau = \frac{\pi \sigma_\Omega}{2\Omega} = \frac{\pi \sigma_I}{2I} \quad (7.3)$$

For a complete interferometer sequence the intensity fluctuation for each pulse is independent giving a standard deviation given by equation 7.4.

$$\sigma_W = \frac{\sqrt{3}\pi\sigma_I}{2I} \quad (7.4)$$

Using the relation  $(S/N)^{-1} = \sigma_W = \sigma_{\Delta\phi}$  and assuming the fluctuation of the Raman laser intensity is up to 1%, the corresponding interferometer phase noise is calculated to be  $27 \text{ }\mu\text{g}$ .

### 7.5.5 Raman Laser Polarisation

The Raman transition amplitude is dependent on the polarisation configuration of the Raman laser. The polarisation-maintaining fibres direct linear polarised light into the vacuum chamber, a  $\lambda/4$  waveplate before the retro-reflecting mirror at the bottom converts the linear polarisation to the orthogonal polarisation. Unfortunately, coupling imperfections and temperature fluctuations mean the polarisation of the incident laser will shift momentarily. Assuming a polarisation shift of the incident laser of  $\theta$ , then the angle between the incident and retro-reflected beam is shifted by  $2\theta$ . This causes the Rabi frequency to change by  $\sigma_\Omega = 2\theta\Omega$ . Given the transition probability,  $P = A(1 + C\cos(\Omega\tau))$  the fluctuation of the transition probability at the midfringe is given by

$$\sigma_P = -AC\sin(\Omega\tau)\tau\sigma_\Omega. \quad (7.5)$$

The polarisation extinction ratio of the Raman laser is 30 dB causing the transition probability to fluctuate by 0.0016. This amounts to a phase shift of 3.1 mrad and a noise of 3.2  $\mu\text{g}$  when  $T = 2.5$  ms.

### 7.5.6 Vibration

As discussed in section 2.9.2, vibrations on the retro-reflecting mirror can limit sensitivity. In the laboratory environment, without vibration isolation,



the maximum  $T$  time of the interferometer is below 3.5 ms. Beyond this, the interference pattern is washed out, as observed in the comparison between figures 7.13a and 7.13b. With the addition of vibration isolation, the  $T$  time can be further extended, as shown in figure 7.16. The error in gravity measurement is related to vibrational noise using equation 7.6.  $S_a(\omega)$  represents the power spectral density of vibrational acceleration and acts as the transfer function. Assuming a white noise spectrum with  $\sqrt{S_a} = 1 \times 10^{-6} \text{ ms}^{-2}$ , for  $T = 2.5 \text{ ms}$  and  $\tau = 3 \mu\text{s}$ ,  $\sigma_\phi$  is found to be 2.9 mrad, corresponding to  $\frac{\sigma_g}{g} = 2.9 \mu\text{g}$ . Using a low  $T$  time greatly reduces sensitivity to vibrational noise compared to traditional long baseline experiments. In this project, which prioritises high-bandwidth and short  $T$  time, vibrations are less of a concern compared to other factors. However, in contrast, at  $T = 100 \text{ ms}$  and in the same vibrational environment  $\sigma_\phi = 620 \text{ mrad}$ , resulting in  $\frac{\sigma_g}{g} = 0.3 \mu\text{g}$  which is far more concerning for this parameter space.

$$\sigma_g = \frac{\sigma_\phi}{k_{\text{eff}} T^2} = \sqrt{\int_0^\infty |H_\phi|^2 \frac{1}{T^4 \omega^4} S_a(\omega) d\omega}. \quad (7.6)$$

## 7.6 Systematic Issues

In this section potential systematic measurement errors are analysed. These effects bias the measurement by altering the Raman resonance condition (quadratic Zeeman effect and the AC Stark effect) and altering the value of  $k_{\text{eff}}$ .

### 7.6.1 Magnetic Field

Atoms in our experiment are prepared in the magnetically insensitive  $m_F = 0$  state but are still subject to the quadratic Zeeman effect. This energy level shift is expressed by the Breit-Rabi formula where  $\kappa = 575.15 \text{ Hz/G}^2$ .

$$E_{\text{Breit Rabi}} \approx \frac{\mu_B^2 g_J^2}{2\hbar\omega_0} B^2 = \kappa B^2. \quad (7.7)$$

$\omega_0$  is the angular frequency of the unperturbed hyperfine splitting of the ground state and  $g_J \approx 2$  is the Landé g-factor of the total electron angular momentum. The symmetry of the sensitivity function  $g(t)$  means a uniform magnetic field does not contribute to the interferometer phase. However, the magnetic environment is inhomogeneous generating systematic errors. The magnetic field gradient causes a parasitic acceleration bias on atoms in the  $m_F = 0$  ground states.

$$\mathbf{a}_{\text{Breit Rabi}} = \frac{\mu_B^2 g_J^2}{m\hbar\omega_0} \mathbf{B} \cdot \nabla \mathbf{B}. \quad (7.8)$$

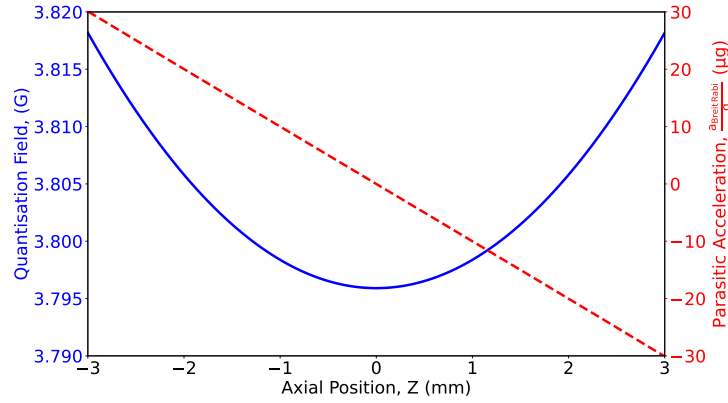


Figure 7.18: Simulating spatial dependence of magnetic field and parasitic acceleration for vertical quantisation field during interferometer. Magnetic field profile of vertical quantisation coils (blue solid) and parasitic acceleration (red dashed).

The simulation of the quantisation coil's field profile and gradient allows for the calculation of acceleration, as illustrated in Figure 7.18. With a launch velocity of  $0.25 \text{ ms}^{-1}$  and  $T = 2.5 \text{ ms}$ , the cloud falls about 2 mm. Due to the sub-optimal aspect ratio of the coils and high bias field, the average acceleration amounts to about  $10 \mu\text{g}$ . This significant systematic shift could be notably reduced by successfully implementing optical pumping enabling the bias field to be reduced from 4G to 1G. Moreover, an improved compensation coil design with a better aspect ratio would improve homogeneity and minimise  $\nabla B$ .

### 7.6.2 Two-photon Light Shift

The retro-reflection configuration utilising the Raman beams consists of two pairs of counter-propagating Raman lasers with opposite wavevectors, driving

the two-photon Raman transition. When the frequency difference of one pair is resonant with the hyperfine states, the Raman transition is induced. However, the other pair, which is off-resonant, induces a two-photon light shift (TPLS). The phase shift caused by this effect is described by equation 7.9, where  $v_0$  and  $v_2$  represent the cloud velocity at the first and last pulses, respectively.

$$\delta\Phi_{\text{TPLS}} = \frac{\Omega_{\text{eff}}}{4k_{\text{eff}}} \left( \frac{1}{v_2} - \frac{1}{v_0} \right). \quad (7.9)$$

The substitution of the effective Rabi frequency  $\frac{\Omega_{\text{eff}}}{2\pi} = 150 \text{ kHz}$ ,  $v_0 = -0.20 \text{ ms}^{-1}$ , and  $v_2 = -0.25 \text{ ms}^{-1}$  yields an interferometer phase shift of  $\delta\Phi_{\text{TPLS}} = 14.6 \text{ mrad}$ . The gravity measurement is biased by approximately  $14.8 \text{ } \mu\text{g}$  due to this shift [123].

### 7.6.3 Laser Alignment

When the Raman beams are tilted with respect to the direction of local gravity a measurement bias is introduced. The error induced by a tilt  $\theta$  can be approximated by  $\Delta g = g(\cos(\theta) - 1) \approx -g|\theta|^2$  where  $\theta$  denotes the angle between the local vector of the gravitational acceleration and the Raman beam axis. For a tilt of  $0.1 \text{ mrad}$  the measured gravitational acceleration is decreased by  $5 \text{ ng}$ . For our high-data rate experiment aiming for  $1 \text{ } \mu\text{g}$  sensitivity a tilt of  $14 \text{ mrad}$  would be compromising suggesting at least of order of magnitude less sensitivity to tilt than long T time experiments. This

effect is not specific to atom interferometers but to any gravimeter measuring gravity only along a specific axis. One method for precision alignment of the Raman beams is using a reference surface in the form of a liquid surface. For portable applications an electronic tilt-meter to monitor verticality is more tractable. Alternatively, as measurement bias is always negative tilt could be adjusted until the largest gravitational acceleration is measured.

#### 7.6.4 Coriolis Effect

As inertial measurements are performed in the rotating frame of the Earth the Coriolis force should be considered. This fictitious force manifests in the measured acceleration and is given by equation 7.10. [124] [77].

$$\mathbf{a}_{\text{Coriolis}} = 2\boldsymbol{\Omega}_{\text{Earth}} \times \mathbf{v}. \quad (7.10)$$

Using parameters for the rotation of the Earth  $\Omega_{\text{Earth}} = 72.7 \mu\text{rad/s}$  and  $\mathbf{v}$  which is the atom velocity, the Coriolis force can be computed. The orientation of the inertial measurement is dictated by the Raman laser wavevector  $\mathbf{k}_{\text{eff}}$ . Atoms with a horizontal velocity in the east-west direction  $\mathbf{v}_{\text{w-e}}$  induce a Coriolis force with a non-zero projection along  $\mathbf{k}_{\text{eff}}$ . This causes decaying fringe contrast and also a systematic error in the gravity measurement. Replacing  $g$  with  $\mathbf{a}_{\text{coriolis}}$  in the phase equation gives a phase shift given by equation 7.11.

$$\delta\Phi_{\text{Coriolis}} = 2\Omega_{\text{Earth}} \cdot (\mathbf{v}_{\text{w-e}} \times \mathbf{k}_{\text{eff}})T^2. \quad (7.11)$$

In the experiment, an atom’s horizontal velocity is determined by observing the cloud centre shift after launch, yielding  $v_{\text{H}} = 13 \text{ mms}^{-1}$ . Assuming  $v_{\text{w-e}} = v_{\text{H}}$ , a systematic error of  $0.190 \mu\text{g}$  is introduced.

## 7.7 Environmental Effects

Gravity measurements are affected by location-specific factors, including sub-surface mass of the Earth, latitude variations, elevation differences, and terrain characteristics. These factors manifest as observable effects on local gravity, as shown in Table 7.1. Typically, environmental uncertainties are not considered when determining uncertainties of absolute gravimeters. However, understanding these effects are important to make meaningful comparisons across different times and locations. Moreover, gravitational variations arising from environmental influences can mask instrument related limitations.

Source	Magnitude/ $\mu\text{Gal}$	Uncertainty/ $\mu\text{Gal}$	Timescale
Solid Earth Tides	300	0.2 to 0.5	Diurnal
Ocean Loading	20	0.2	Diurnal
Air Pressure	8	1 to 5	Hours-diurnal
Water Table	Site-dependent	Site-dependent	Seasonal
Polar Motion	10	$< 0.01$	12, 14 months

Table 7.1: Environmental Effects. Data from [122].

Variations in atmospheric pressure change local gravity, for example at higher

air pressure the mass of gas exerts an upward gravitational force reducing the measured  $g$  value. The amplitude of the gravity variation is approximately  $\Delta g = -0.36 \mu\text{Gal mbar}^{-1}$ . The typical daily pressure fluctuation in the UK is around 10 mbar leading to variations of a few  $\mu\text{Gal}$ . This makes detailed pressure records essential so appropriate corrections can be applied. The absolute gravity measured can be corrected by the equations below where  $P$  is the measured pressure and  $P_n$  is the nominal pressure.

$$\delta g_{\text{air}} = \kappa_{\text{air}}(P - P_n). \quad (7.12a)$$

$$P_n = 1013.25 \left(1 - \frac{0.0065h}{288.15m}\right)^{5.2559} \quad (7.12b)$$

Frequent rainfall in the British Isles leads to varying levels of lakes, rivers, and groundwater, affecting local gravity. This effect is known as the Bouguer effect and considers the gravitational attraction of a horizontal slab with thickness equal to the elevation difference. Equation 7.13 describes the change in gravity per meter of elevation difference, where  $d$  is the mean density of the slab. For a density of  $1 \text{ g/cm}^3$ , a 10 cm downpour could increase local gravity by  $\sim 4 \mu\text{Gal}$ .

$$\delta g_p = +0.04192 d \text{ mGal}. \quad (7.13)$$

The surface vertical gravity gradient is approximately  $-300 \mu\text{Gal/m}$ . Its con-

tribution to systematic errors can be estimated using Equation 7.14 with relevant parameters. For our setup ( $\gamma = -300 \text{ } \mu\text{Gal/m}$ ,  $v = 0.3 \text{ ms}^{-1}$ , and  $T = 2.5 \text{ ms}$ ), the estimated systematic error due to gravity gradient is  $-2 \text{ } \mu\text{rad}$  or  $-0.2 \text{ } \mu\text{Gal}$ . However, this error is several orders of magnitude below our target sensitivity, allowing us to neglect gravity gradients.

$$\delta\Phi_{\text{gradient}} = \gamma k_{\text{eff}} T^3 \left( \frac{7}{12} g T - v \right). \quad (7.14)$$

## 7.8 Summary

In this chapter, the sensitivity limitation was explored and the accuracy of gravity measurements from the current experiment was estimated. The systematic noise budget is listed in table 7.2. The primary limitation of the sensitivity is attributed to the use of single-state detection, which generates a phase noise of  $80 \text{ mrad}$ , corresponding to a sensitivity of  $80 \text{ } \mu\text{g}$  in a single measurement. To eliminate this limitation, it is recommended that two-state detection be performed using a photodiode or a faster camera. The second biggest term is contributed by the intensity noise of the Raman laser, which will require some form of intensity stabilisation. Table 7.3 shows the systematic error budget with the biggest contributions made by the magnetic field gradient and the two-photon light shift. In order to suppress the magnetic effect a more homogeneous bias coil design would be needed with optical pumping to reduce the required bias field. To address the two-photon light



shift, techniques for removing the secondary peak would be beneficial to ensure it does not pose an issue. Given explicit knowledge of the systematic bias, post correction can be employed on the final gravity measurement.

Source	Phase Noise/(mrad)	Sensitivity/ $\mu\text{g}$	
MOT Fluctuations	80	80	
Quantum Projection Noise	0.45	0.45	
Photon Shot Noise	-	-	Neglected
Vibration Noise	2.9	2.9	
Raman Intensity Noise	27.2	27.5	
Raman Polarisation Noise	3.1	3.2	
<b>Total</b>		<b>85</b>	

Table 7.2: Systematic Noise Budget.

Source	Phase Shift/(mrad)	Bias/ $\mu\text{g}$
Magnetic Field Gradient	10.0	10.1
Raman Laser Alignment	1.0	1.0
Two Photon Light Shift	14.6	14.8
Coriolis Force	0.2	0.2
<b>Total</b>		<b>26.1</b>

Table 7.3: Systematic Error Budget.

## Chapter 8

# Conclusion

This work details the construction of a high-data rate absolute quantum gravimeter using Raman atom optics with laser-cooled  $^{87}\text{Rb}$ . It outlines a practical and theoretical framework for atom interferometry with a path toward mobile dynamic quantum sensors. The system launches around  $1 \times 10^8$  atoms downward at  $0.25 \text{ ms}^{-1}$  achieving a temperature of  $25 \text{ } \mu\text{K}$  in  $3 \text{ ms}$ . A free-space laser system was built to generate cold atoms with a separate fibre system developed for atom interferometry. The setup achieves a short-term sensitivity of  $10 \text{ } \mu\text{g}/\sqrt{\text{Hz}}$  with single state detection averaging down to  $1 \text{ } \mu\text{g}$  after  $100 \text{ s}$ . Systematic errors are analysed with the preliminary accuracy limited by MOT fluctuations coupling into detection. A key highlight is demonstrating the fibre-Bragg grating laser system which is promising for transportable sensors and therefore mobile applications. Another highlight is using simple MOT physics to validate recapture at high-bandwidth opera-

---

tion by comparing with experimental data. Efficient recapture is essential for achieving a large MOT population at high-bandwidth. Through optimising duty cycle a theoretical performance limit of  $\sim 1 \times 10^{-7} \text{ g}/\sqrt{\text{Hz}}$  is obtained at 100 Hz; roughly 2 orders better than current performance [57]. Overall, devoting cycle time to interrogation rather than loading atoms is beneficial provided recapture is not significantly compromised. For a next generation mobile system a comparison campaign with a classical gravimeter is intended. Due to the time constraints of this PhD project, several potential improvements for the system remain as prospects.

- Improvements in the detection scheme are needed to approach the shot noise detection limit. Based on the noise analysis, simultaneous detection of the two ground states would be the first stage before exploring intensity stabilisation of the Raman laser.
- Currently, atoms are launched to break Raman degeneracy. This causes them to move rapidly away from the trap centre, negatively impacting recapture, temperature and the potential for longer interrogation times. Therefore, techniques for breaking degeneracy without using launching should be explored [125]. Figure 8.1 highlights how launching negatively influences recapture for increasing interrogation time. For a 20 ms freefall time with a typical launch velocity of  $v_0 = -0.30 \text{ ms}^{-1}$  an atom will have almost left the trapping region. In contrast, without a

launch the atom remains almost at the trap centre. Figures 8.2a and 8.2b examine this using the recapture model to highlight how for lower bandwidth the launch velocity becomes increasingly compromising.

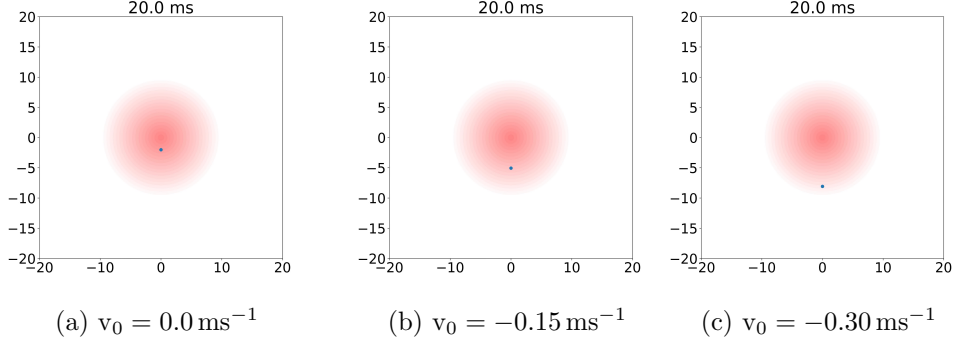


Figure 8.1: Location of single atom with variable initial velocity  $v_0$  after 20 ms of freefall. XY plane is measured in mm. Red circle illustrates trapping region, with reduced colour saturation reflecting reduced trap light intensity.

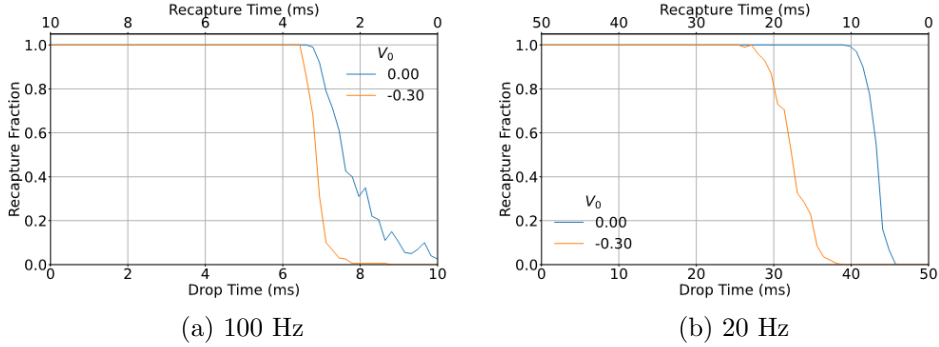


Figure 8.2: Simulating restored atom fraction for a cloud of  $^{87}\text{Rb}$  atoms, a.) 100 Hz MOT b.) 20 Hz MOT for variable duty cycle and initial velocity.

- The large bias field is undesirable. Currently it is required for separating the  $m_f$  states but this presents challenges due to systematic bias from the second-order Zeeman shift and the high current needed from the coil driver. Optical pumping initialising all atoms in the  $m_f = 0$  state would

---

address this and also increase atoms participation in the interferometer.

- Designing a portable version of the fibre-Bragg grating laser system.

Since all components are fibre devices, it has the potential to be compact, cost-effective, and robust. To enable this the subsystems will require further development. Namely, this includes developing the laser, RF, vacuum and optomechanical structure.

- A detailed study of systemic errors beyond leading-order effects would also be desirable.
- Further investigation and development would be interesting to establish a stronger connection between experimental observations and theoretical understanding of sub-Doppler cooling. Although this cooling mechanism is widely used there is a gap in understanding particularly at short timescales. Closing this knowledge gap would have broader implications beyond purely high-bandwidth applications.

These suggested improvements could hold potential for enhancing performance and expanding future system capability.

# Appendix A

## Rubidium-87 Data

The relevant properties of the  $^{87}\text{Rb}$  isotope and its D<sub>2</sub>-line transition are shown in table A.1. The D<sub>2</sub>-line allows several possible two-photon transitions to be driven between  $|F = 1\rangle$  and  $|F = 2\rangle$  ground states in  $^{87}\text{Rb}$  via the  $5^2\text{P}_{3/2}$  excited state.

Table A.1: Properties of  $^{87}\text{Rb}$  isotope and its D<sub>2</sub>-line transition, values from [89].

Parameter	Sym- bol	Value
Mass	m	$1.443\,16 \times 10^{-25}\text{kg}$
Wavelength (Vacuum)	$\lambda$	780.24 nm
$ F = 2\rangle \leftrightarrow  F = 3'\rangle$	$\nu_{2\leftrightarrow 3}$	384.228 115 20 THz
$ F = 1\rangle \leftrightarrow  F = 2'\rangle$	$\nu_{1\leftrightarrow 2}$	384.234 683 23 THz
$5^2S_{1/2}$	$f_{\text{HFS}}$	6.834 682 610 9 GHz
Excited state lifetime	$\tau_0$	26.235 ns
Natural linewidth	$\Gamma$	$2\pi \times 6.067\text{ MHz}$
Recoil Velocity	$v_{\text{recoil}}$	$5.8845\text{ mms}^{-1}$
Doppler temperature	$T_{\text{D}}$	145.6 $\mu\text{K}$
Recoil temperature	$T_{\text{recoil}}$	362 nK
Transition Dipole Matrix Element	D	$3.5842 \times 10^{-29}\text{ C m}$
$ F = 2\rangle \leftrightarrow  F = 3'\rangle$ transition (isotropic polarisation)	$I_{\text{sat}}$	$3.5771\text{ mWcm}^{-2}$

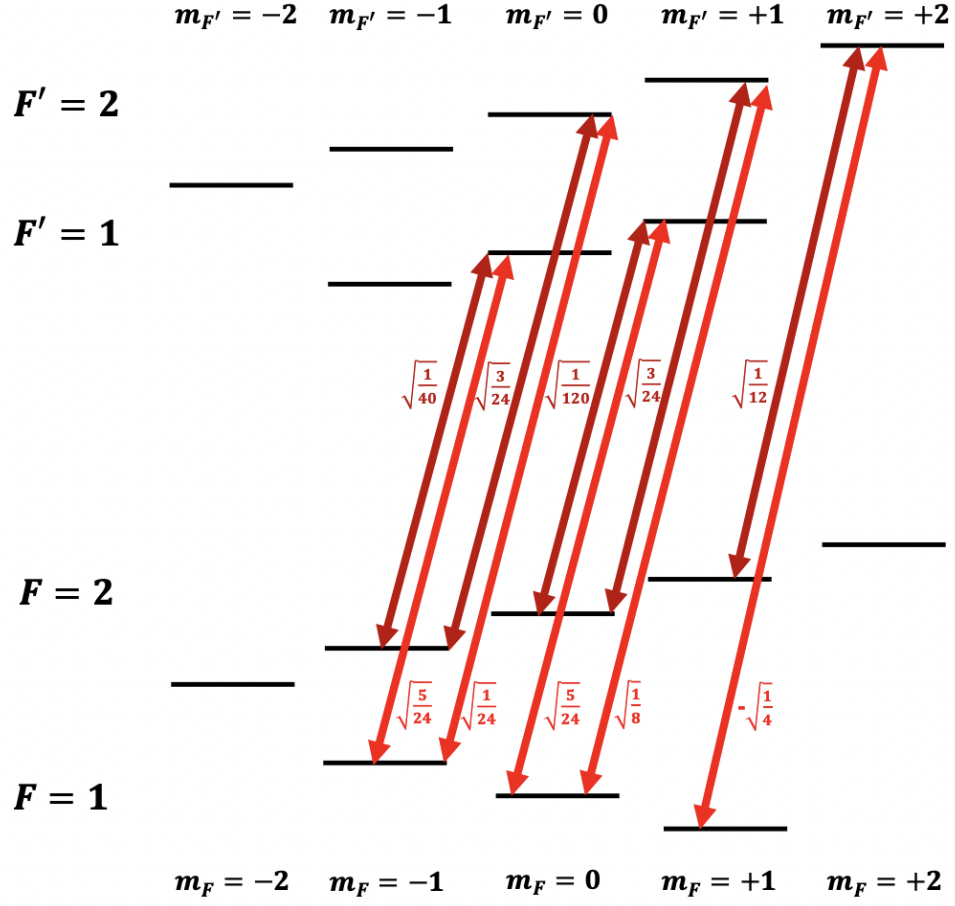


Figure A.1: Two-photon  $\sigma^+ - \sigma^+$  transition between magnetic sublevels of  $F = 1$  and  $F = 2$  in  $^{87}\text{Rb}$   $D_2$  transition. Multiples of dipole matrix elements  $\langle J = 1/2 || e || J' = 3/2 \rangle$  are indicated. Modified from [81].

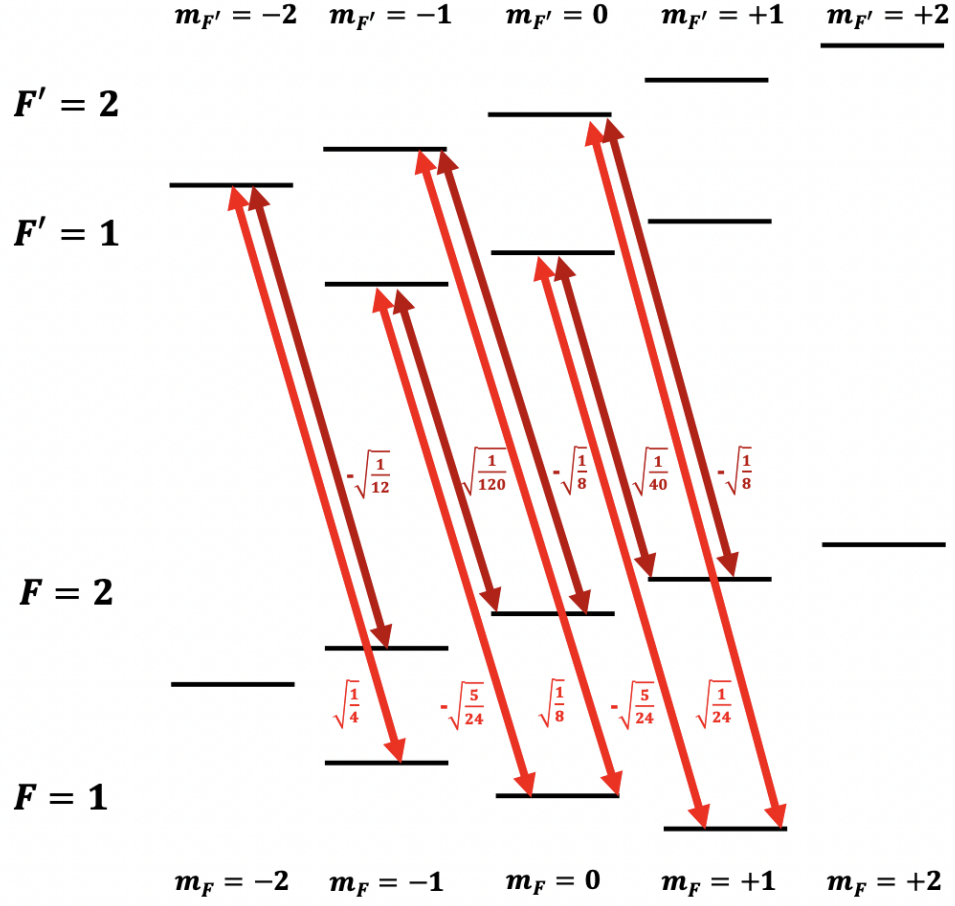


Figure A.2: Two-photon  $\sigma^- - \sigma^-$  transition between magnetic sublevels of  $F = 1$  and  $F = 2$  in  $^{87}\text{Rb}$   $D_2$  transition. Multiples of dipole matrix elements  $\langle J = 1/2 || e || J' = 3/2 \rangle$  are indicated. Modified from [81].



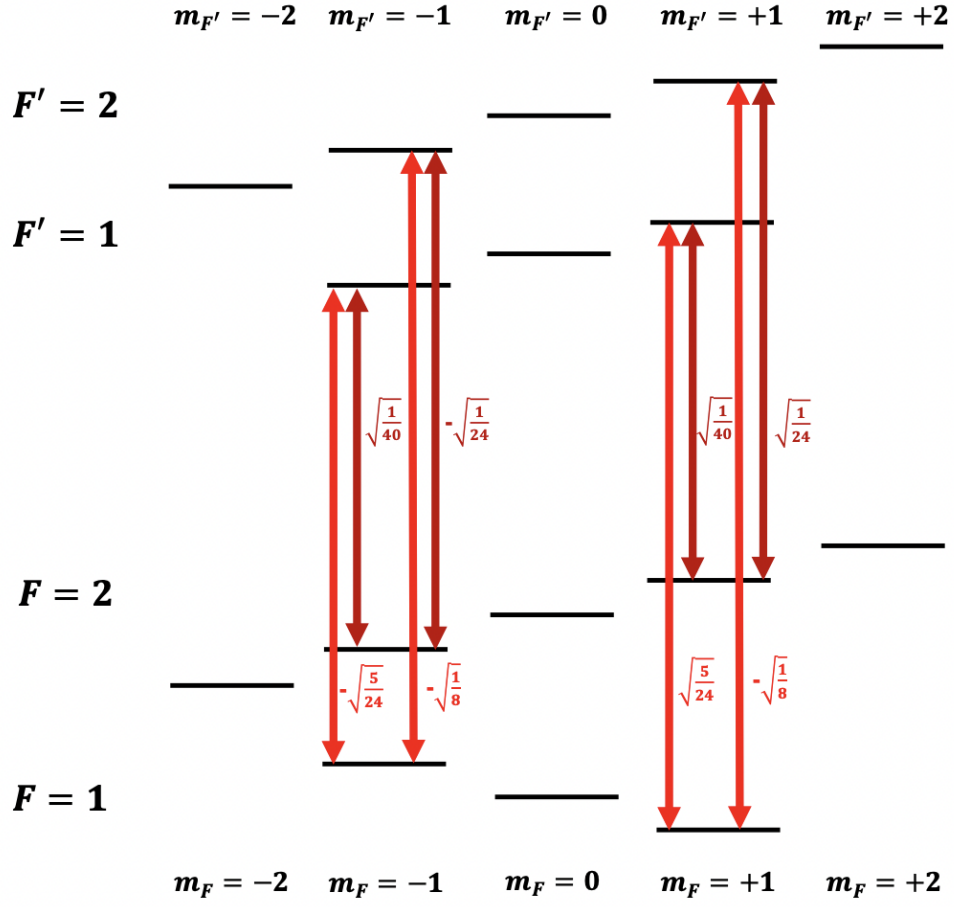


Figure A.3: Two-photon  $\pi - \pi$  transition between magnetic sublevels of  $F = 1$  and  $F = 2$  in  $^{87}\text{Rb}$   $D_2$  transition. Multiples of dipole matrix elements  $\langle J = 1/2 || e || J' = 3/2 \rangle$  are indicated. Modified from [81].

# Bibliography

- [1] K. Bongs, M. Holynski, J. Vovrosh, P. Bouyer, G. Condon, E. Rasel, C. Schubert, W. P. Schleich, and A. Roura. *Taking atom interferometric quantum sensors from the laboratory to real-world applications*. Nat. Rev. Phys., **1**(12):731–739, 2019.
- [2] K. Bongs, M. Holynski, and Y. Singh.  *$\psi$  in the sky*. Nat. Phys., **11**(8):615–617, 2015.
- [3] J. Rushton, M. Aldous, and M. Himsworth. *Contributed review: The feasibility of a fully miniaturized magneto-optical trap for portable ultracold quantum technology*. Rev. Sci. Instrum., **85**(12):121501, 2014.
- [4] B. Fang, I. Dutta, P. Gillot, D. Savoie, J. Lautier, Bing C., CL Garrido Alzar, R. Geiger, S. Merlet, F Pereira Dos Santos, et al. *Metrology with atom interferometry: inertial sensors from laboratory to field applications*. J. Phys. Conf. Ser., **723**(1):012049, 2016.
- [5] Y. Bidel, N. Zahzam, C. Blanchard, A. Bonnin, M. Cadoret, A. Bresson, D. Rouxel, and M. F. Lequentrec-Lalancette. *Absolute marine gravimetry with matter-wave interferometry*. Nat. Commun., **9**(1):1–9, 2018.
- [6] M. Walport and P. Knight. *The quantum age: Technological opportunities*. Blackett Review, 2016.
- [7] B. Battelier, B. Barrett, L. Fouché, L. Chichet, L. Antoni-Micollier, H. Porte, F. Napolitano, J. Lautier, A. Landragin, and P. Bouyer. *Development of compact cold-atom sensors for inertial navigation*. Quantum Optics, **9900**:21–37, 2016.
- [8] V. Ménoret, P. Vermeulen, N. Le Moigne, S. Bonvalot, P. Bouyer, A. Landragin, and B. Desruelle. *Gravity measurements below  $10^{-9} g$  with a transportable absolute quantum gravimeter*. Sci. Rep., **8**(1):1–11, 2018.

- 
- [9] X. Wu, Z. Pagel, B. Malek, T. Nguyen, F. Zi, D. Scheirer, and H. Müller. *Gravity surveys using a mobile atom interferometer*. Sci. Adv., **5**(9):eaax0800, 2019.
  - [10] M. De Angelis, A. Bertoldi, L. Cacciapuoti, A. Giorgini, G. Lamporesi, M. Prevedelli, G. Saccorotti, F. Sorrentino, and G. Tino. *Precision gravimetry with atomic sensors*. Measurement Science and Technology, **20**(2):022001, 2008.
  - [11] H. D. Young, R. A. Freedman, T. R. Sandin, and A. L. Ford. *University Physics*, volume 9. Addison-Wesley Reading, MA, 1996.
  - [12] M. Caputo and L. Pieri. *The normal gravity formula and the polar flattening according to geodetic reference system 1967*. Ann. Geophys., **21**(1):123–149, 1968.
  - [13] R. Rummel. *Geoid and gravity in Earth sciences—an overview*. Future Satellite Gravimetry and Earth Dynamics, pages 3–11, 2005.
  - [14] W. Torge. *Gravimetry*. De Gruyter, 1989.
  - [15] *CG-6 Brochure*. [https://6c3ae8.a2cdn1.secureserver.net/wp-content/uploads/2019/01/CG-6-Brochure\\_R5.pdf](https://6c3ae8.a2cdn1.secureserver.net/wp-content/uploads/2019/01/CG-6-Brochure_R5.pdf). Accessed: 2023-03-15.
  - [16] U. Riccardi, S. Rosat, and J. Hinderer. *On the accuracy of the calibration of superconducting gravimeters using absolute and spring sensors: a critical comparison*. Pure Appl. Geophys., **169**:1343–1356, 2012.
  - [17] A. Krasnov, A. Sokolov, and L. Elinson. *A new air-sea shelf gravimeter of the Chekan series*. Gyroscopy Navig., **5**(3):131–137, 2014.
  - [18] L. Zheleznyak, V. Koneshov, A. Krasnov, A. Sokolov, and L. Elinson. *The results of testing the Chekan gravimeter at the Leningrad gravimetric testing area*. Izv. Phys. Solid Earth, **51**(2):315, 2015.
  - [19] *iGrav Brochure*. <https://www.gwrinstruments.com/pdf/igrav-brochure.pdf>. Accessed: 2023-03-15.
  - [20] R. Warburton, H. Pillai, and R. Reineman. *Initial results with the new GWR iGrav superconducting gravity meter*. In *Extended Abstract Presented at 2nd Asia Workshop on Superconducting Gravimetry Taipei, Taiwan*, 2010.
  - [21] R. Middlemiss, A. Samarelli, D. Paul, J. Hough, S. Rowan, and G. Hammond. *Measurement of the Earth tides with a MEMS gravimeter*. Nature, **531**(7596):614–617, 2016.

- 
- [22] O. Carnal and J. Mlynek. *Young's double-slit experiment with atoms: A simple atom interferometer*. Phys. Rev. Lett., **66**(21):2689, 1991.
  - [23] L. De Broglie. *Waves and quanta*. Nature, **112**(2815):540–540, 1923.
  - [24] L. De Broglie. *The wave nature of the electron*. Nobel lecture, **12**:244–256, 1929.
  - [25] K. Zetie, S. Adams, and R. Tocknell. *How does a Mach-Zehnder interferometer work?* Physics Education, **35**(1):46, 2000.
  - [26] C. Freier, M. Hauth, V. Schkolnik, B. Leykauf, M. Schilling, H. Wziontek, H. Scherneck, J. Müller, and A. Peters. *Mobile quantum gravity sensor with unprecedented stability*. In *Journal of physics: conference series*, volume 723, page 012050. IOP Publishing, 2016.
  - [27] M. Schmidt, A. Senger, M. Hauth, C. Freier, V. Schkolnik, and A. Peters. *A mobile high-precision absolute gravimeter based on atom interferometry*. Gyroscopy and Navigation, **2**(3):170, 2011.
  - [28] M. Hauth, C. Freier, V. Schkolnik, A. Peters, H. Wziontek, and M. Schilling. *Atom interferometry for absolute measurements of local gravity*. In *Proceedings of the International School of Physics" Enrico Fermi*, volume 188, pages 557–586, 2014.
  - [29]  $\mu$ QUANS, *Absolute Quantum Gravimeter*. <https://www.muquans.com/product/absolute-quantum-gravimeter/>. Accessed: 2023-03-15.
  - [30] Z. Fu, B. Wu, B. Cheng, Y. Zhou, K. Weng, D. Zhu, Z. Wang, and Q. Lin. *A new type of compact gravimeter for long-term absolute gravity monitoring*. Metrologia, **56**(2):025001, 2019.
  - [31] Y. Bidel, N. Zahzam, A. Bresson, C. Blanchard, M. Cadoret, A. Olesen, and R. Forsberg. *Absolute airborne gravimetry with a cold atom sensor*. J Geod, **94**:1–9, 2020.
  - [32] O. Carraz, F. Lienhart, R. Charrière, M. Cadoret, N. Zahzam, Y. Bidel, and A. Bresson. *Compact and robust laser system for onboard atom interferometry*. Appl. Phys. B., **97**:405–411, 2009.
  - [33] P. Gillot, O. Francis, A. Landragin, F. Dos Santos, and S. Merlet. *Stability comparison of two absolute gravimeters: optical versus atomic interferometers*. Metrologia, **51**(5):L15, 2014.
  - [34] Micro-g LaCoste, *FG5-X Absolute Gravity Meters*. <https://microglacoste.com/product/fg5-x-absolute-gravimeter/>. Accessed: 2023-03-15.

- 
- [35] B. Canuel, S. Pelisson, L. Amand, A. Bertoldi, E. Cormier, B. Fang, S. Gaffet, R. Geiger, J. Harms, D. Holleville, et al. *MIGA: combining laser and matter wave interferometry for mass distribution monitoring and advanced geodesy*. In *Quantum Optics*, volume 9900, pages 54–65. SPIE, 2016.
  - [36] R. Geiger, A. Landragin, S. Merlet, and F. Pereira Dos Santos. *High-accuracy inertial measurements with cold-atom sensors*. AVS Quantum Science, **2**(2):024702, 2020.
  - [37] B. Adams, C. Macrae, M. Entezami, K. Ridley, A. Kubba, Y. Lien, S. Kinge, and K. Bongs. *The development of a High data rate atom interferometric gravimeter (HIDRAG) for gravity map matching navigation*. IEEE (INERTIAL), pages 1–4, 2021.
  - [38] G. Rosi, F. Sorrentino, L. Cacciapuoti, M. Prevedelli, and G. Tino. *Precision measurement of the Newtonian gravitational constant using cold atoms*. Nature, **510**(7506):518–521, 2014.
  - [39] A. Wicht, J. Hensley, E. Sarajlic, and S. Chu. *A preliminary measurement of the fine structure constant based on atom interferometry*. Phys. Scr., **2002**(T102):82, 2002.
  - [40] P. Cheinet, F. Dos Santos, T. Petelski, A. Clairon, N. Dimarcq, D. Holleville, and A. Landragin. *Cold atom absolute gravimeter for the watt balance*. In *2004 Conference on Precision Electromagnetic Measurements*, pages 60–61. IEEE, 2004.
  - [41] L. Zhou, S. Long, B. Tang, X. Chen, F. Gao, W. Peng, W. Duan, J. Zhong, Z. Xiong, J. Wang, et al. *Test of equivalence principle at  $10^{-8}$  level by a dual-species double-diffraction Raman atom interferometer*. Phys. Rev. Lett., **115**(1):013004, 2015.
  - [42] F. Sorrentino, K. Bongs, P. Bouyer, L. Cacciapuoti, M. De Angelis, H. Dittus, W. Ertmer, A. Giorgini, J. Hartwig, M. Hauth, et al. *A compact atom interferometer for future space missions*. Microgravity Sci. Technol., **22**(4):551–561, 2010.
  - [43] J. Hogan, D. Johnson, S. Dickerson, T. Kovachy, A. Sugarbaker, S. Chiow, P. Graham, M. Kasevich, B. Saif, S. Rajendran, et al. *An atomic gravitational wave interferometric sensor in low earth orbit (AGIS-LEO)*. Gen. Relativ. Gravit., **43**:1953–2009, 2011.
  - [44] P. Hamilton, M. Jaffe, P. Haslinger, Q. Simmons, H. Müller, and J. Khoury. *Atom-interferometry constraints on dark energy*. Science, **349**(6250):849–851, 2015.

- 
- [45] S. Dimopoulos, P. Graham, J. Hogan, and M. Kasevich. *Testing general relativity with atom interferometry*. Phys. Rev. Lett., **98**(11):111102, 2007.
  - [46] J. Hartwig, S. Abend, C. Schubert, D. Schlippert, H. Ahlers, K. Posso-Trujillo, N. Gaaloul, W. Ertmer, and E. Rasel. *Testing the universality of free fall with rubidium and ytterbium in a very large baseline atom interferometer*. New J. Phys., **17**(3):035011, 2015.
  - [47] M. Kasevich. *Atom interferometry in an atomic fountain*. PhD thesis, Stanford University, 1992.
  - [48] J. Rudolph, T. Wilkason, M. Nantel, H. Swan, C. Holland, Y. Jiang, B. Garber, S. Carman, J. Hogan, et al. *Large momentum transfer clock atom interferometry on the 689 nm intercombination line of strontium*. Phys. Rev. Lett., **124**(8):083604, 2020.
  - [49] T. Wilkason, M. Nantel, J. Rudolph, Y. Jiang, B. Garber, H. Swan, S. Carman, M. Abe, J. Hogan, et al. *Atom interferometry with Floquet atom optics*. Phys. Rev. Lett., **129**(18):183202, 2022.
  - [50] A. Sugarbaker, S. M. Dickerson, J. M. Hogan, D. MS Johnson, and M. Kasevich. *Enhanced atom interferometer readout through the application of phase shear*. Phys. Rev. Lett., **111**(11):113002, 2013.
  - [51] K. Bongs, J. Malcolm, C. Rammello, L. Zhu, V. Boyer, T. Valenzuela, J. Maclean, A. Piccardo-Selg, C. Mellor, T. Fernholz, et al. *iSense: A technology platform for cold atom based quantum technologies*. In *Research in Optical Sciences, OSA Technical Digest, QTu3B-1*. Optica Publishing Group, 2014.
  - [52] N. Heine, J. Matthias, M. Sahelgozin, W. Herr, S. Abend, L. Timmen, J. Müller, and E. Rasel. *A transportable quantum gravimeter employing delta-kick collimated Bose-Einstein condensates*. Eur. Phys. J. D, **74**:1–8, 2020.
  - [53] B. Stray, A. Lamb, A. Kaushik, J. Vovrosh, A. Rodgers, J. Winch, F. Hayati, D. Boddice, A. Stabrawa, A. Niggebaum, et al. *Quantum sensing for gravity cartography*. Nature, **602**(7898):590–594, 2022.
  - [54] *Q-CTRL*. <https://q-ctrl.com>. Accessed: 2023-03-01.
  - [55]  *$\mu$ QUANS*. <https://www.muquans.com/>. Accessed: 2023-03-01.
  - [56] *AOSense*. <https://aosense.com>. Accessed: 2023-03-01.
  - [57] A. Rakholia, H. McGuinness, and G. Biedermann. *“Dual-axis high-data-rate atom interferometer via cold ensemble exchange”*. Phys. Rev. Appl., **2**(5):054012, 2014.

- [58] *National Quantum Strategy 2023*. Accessed: 2023-03-16.
- [59] M. Wright, L. Anastassiou, C. Mishra, J. Davies, A. Phillips, S. Maskell, and J. Ralph. *Cold atom inertial sensors for navigation applications*. Front. Phys., **10**:994459, 2022.
- [60] H. McGuinness, A. Rakholia, and G. Biedermann. *High data-rate atom interferometer for measuring acceleration*. Appl. Phys. Lett., **100**(1):011106, 2012.
- [61] J. Lee, R. Ding, J. Christensen, R. R. Rosenthal, A. Ison, D. P. Gillund, D. Bossert, K. H. Fuerschbach, W. Kindel, P. S. Finnegan, et al. *A compact cold-atom interferometer with a high data-rate grating magneto-optical trap and a photonic-integrated-circuit-compatible laser system*. Nat. Commun., **13**(1):5131, 2022.
- [62] C. Jekeli. *Navigation error analysis of atom interferometer inertial sensor*. Navigation, **52**(1):1–14, 2005.
- [63] A. Phillips, M. Wright, I. Riou, S. Maddox, S. Maskell, and J. Ralph. *Position fixing with cold atom gravity gradiometers*. AVS Quantum Sci., **4**(2):024404, 2022.
- [64] D. Schmidt, K. Radke, S. Camtepe, E. Foo, and M. Ren. *A survey and analysis of the GNSS spoofing threat and countermeasures*. ACM Computing Surveys (CSUR), **48**(4):1–31, 2016.
- [65] M. Psiaki and T. Humphreys. *GNSS spoofing and detection*. Proceedings of the IEEE, **104**(6):1258–1270, 2016.
- [66] C. Hirt, M. Yang, M. Kuhn, B. Bucha, A. Kurzmann, and R. Pail. *SRTM2gravity: an ultrahigh resolution global model of gravimetric terrain corrections*. Geophys. Res. Lett., **46**(9):4618–4627, 2019.
- [67] N. Pavlis, S. Holmes, S. Kenyon, and J. Factor. *The development and evaluation of the Earth Gravitational Model 2008 (EGM2008)*. J. Geophys. Res. Solid Earth, **117**(B4), 2012.
- [68] S. Merlet, Q. Bodart, N. Malossi, A. Landragin, F. Dos Santos, O. Gitlein, and L. Timmen. *Comparison between two mobile absolute gravimeters: optical versus atomic interferometers*. Metrologia, **47**(4):L9, 2010.
- [69] T. Niebauer, G. Sasagawa, J. Faller, R. Hilt, and F. Klopping. *A new generation of absolute gravimeters*. Metrologia, **32**(3):159, 1995.
- [70] K. Moler, D. Weiss, M. Kasevich, and S. Chu. *Theoretical analysis of velocity-selective Raman transitions*. Phys. Rev. A., **45**(1):342, 1992.

- [71] M. Kasevich and S. Chu. *Atomic interferometry using stimulated Raman transitions*. Phys. Rev. Lett., **67**(2):181, 1991.
- [72] P. R. Berman. *Atom Interferometry*. Academic Press, 1997.
- [73] C. Rammeloo. *Optimisation of a compact cold-atoms interferometer for gravimetry*. PhD thesis, University of Birmingham, 2018.
- [74] B. Stray. *A portable cold atom gravity gradiometer with field application performance*. PhD thesis, University of Birmingham, 2021.
- [75] M. Schmidt. *A mobile high-precision gravimeter based on atom interferometry*. PhD thesis, Humboldt-Universität zu Berlin, 2011.
- [76] A. Rakholia. *High data-rate atom interferometry for measuring dynamic inertial conditions*. PhD thesis, The University of New Mexico, 2015.
- [77] L. Zhu. *A cold atoms gravimeter for use in absolute gravity comparisons*. PhD thesis, University of Birmingham, 2018.
- [78] P. Storey and C. Cohen-Tannoudji. *The Feynman path integral approach to atomic interferometry. A tutorial*. J. phys., IV, **4**(11):1999–2027, 1994.
- [79] B. Barrett, P. Gominet, E. Cantin, L. Antoni-Micollier, A. Bertoldi, B. Battelier, P. Bouyer, J. Lautier, and A. Landragin. *Mobile and remote inertial sensing with atom interferometers*. In *International School of Physics "Enrico Fermi" on Atom Interferometry*, 2013.
- [80] P. Cheinet, B. Canuel, F. Pereira Dos Santos, A. Gauguier, F. Yver-Leduc, and A. Landragin. *Measurement of the Sensitivity Function in a Time-Domain Atomic Interferometer*. IEEE Trans. Instrum. Meas., **57**(6):1141–1148, 2008.
- [81] T. Petelski. *Atom interferometers for precision gravity measurements*. PhD thesis, Paris 6, 2005.
- [82] P. Cheinet. *Conception et réalisation d'un gravimètre à atomes froids*. PhD thesis, Université Pierre et Marie Curie-Paris VI, 2006.
- [83] T. Hänsch and A. Schawlow. *Cooling of gases by laser radiation*. Opt. Commun., **13**(1):68–69, 1975.
- [84] D. Wineland and W. Itano. *Laser cooling of atoms*. Phys. Rev. A., **20**(4):1521, 1979.
- [85] H. Metcalf and P. Van der Straten. *Laser cooling and trapping of neutral atoms*. The Optics Encyclopedia: Basic Foundations and Practical Applications, 2007.



- 
- [86] S. Chu, L. Hollberg, J. Bjorkholm, A. Cable, and A. Ashkin. *Three-dimensional viscous confinement and cooling of atoms by resonance radiation pressure*. Phys. Rev. Lett., **55**(1):48, 1985.
- [87] C. Monroe, W. Swann, H. Robinson, and C. Wieman. *Very cold trapped atoms in a vapor cell*. Phys. Rev. Lett., **65**(13):1571, 1990.
- [88] W. D. Phillips. *Nobel Lecture: Laser cooling and trapping of neutral atoms*. Rev. Mod., **70**(3):721, 1998.
- [89] D. Steck. *Alkali D line data*. 2012.
- [90] J. Dalibard and C. Cohen-Tannoudji. *Laser cooling below the Doppler limit by polarization gradients: simple theoretical models*. J. Opt. Soc. Am. B, **6**(11):2023–2045, 1989.
- [91] C. Salomon, J. Dalibard, W. Phillips, A. Clairon, and S. Guellati. *Laser cooling of cesium atoms below 3  $\mu$ K*. EPL, **12**(8):683, 1990.
- [92] Q. Bodart, S. Merlet, N. Malossi, F. Dos Santos, P. Bouyer, and A. Landragin. *A cold atom pyramidal gravimeter with a single laser beam*. Appl. Phys. Lett., **96**(13):134101, 2010.
- [93] V. Bagnato, L. Marcassa, S. Miranda, S. Muniz, and A. de Oliveira. “*Measuring the capture velocity of atoms in a magneto-optical trap as a function of laser intensity*”. Phys. Rev. A., **62**(1):013404, 2000.
- [94] M. Anwar, D. Magalhães, S. Müller, M. Faisal, M. Nawaz, and M. Ahmed. “*Revisiting the capture velocity of a cesium magneto-optical trap: model, simulation and experiment*”. Laser Phys., **24**(12):125502, 2014.
- [95] P. Molenaar. *Photoassociative reactions of laser-cooled sodium*. PhD thesis, Universiteit Utrecht, 1996.
- [96] A. Camara, R. Kaiser, and G. Labeyrie. *Scaling behavior of a very large magneto-optical trap*. Phys. Rev. A., **90**(6):063404, 2014.
- [97] K. Gibble, S. Kasapi, and S. Chu. *Improved magneto-optic trapping in a vapor cell*. Opt. Lett., **17**(7):526–528, 1992.
- [98] G. Hoth, E. Donley, and J. Kitching. *Atom number in magneto-optic traps with millimeter scale laser beams*. Opt. Lett., **38**(5):661–663, 2013.
- [99] U. Rapol, A. Wasan, and V. Natarajan. *Loading of a Rb magneto-optic trap from a getter source*. Phys. Rev. A, **64**(2):023402, 2001.

- [100] Magnus Haw, Nathan Evetts, Will Gunton, Janelle Van Dongen, James L. Booth, and Kirk W. Madison. *Magneto-optical trap loading rate dependence on trap depth and vapor density*. Journal of the Optical Society of America B, **29**(3):475, 2012.
- [101] S. Gensemer, V. Sanchez-Villicana, K. Tan, T. Grove, and P. Gould. *Trap-loss collisions of  $^{85}\text{Rb}$  and  $^{87}\text{Rb}$ : Dependence on trap parameters*. Phys. Rev. A., **56**(5):4055, 1997.
- [102] G. Hoth, B. Pelle, S. Riedl, J. Kitching, and E. Donley. *Point source atom interferometry with a cloud of finite size*. Appl. Phys. Lett., **109**(7):071113, 2016.
- [103] S. Ohshima, T. Kurosu, T. Ikegami, and Y. Nakadan. *Cesium atomic fountain with two-dimensional moving molasses*. Jpn. J. Appl. Phys., **34**(9A):L1170, 1995.
- [104] P. Berthoud, E. Fretel, and P. Thomann. *Bright, slow, and continuous beam of laser-cooled cesium atoms*. Phys. Rev. A., **60**(6):R4241, 1999.
- [105] P. Ungar, D. Weiss, E. Riis, and S. Chu. *Optical molasses and multilevel atoms: theory*. J. Opt. Soc. Am. B, **6**(11):2058–2071, 1989.
- [106] M. Kasevich and S. Chu. *Laser cooling below a photon recoil with three-level atoms*. Phys. Rev. Lett., **69**(12):1741, 1992.
- [107] C. Cohen-Tannoudji and W. Phillips. *New mechanisms for laser cooling*. Phys. Today, **43**(10):33–40, 1990.
- [108] T. Meyrath. *Electromagnet design basics for cold atom experiments*. Technical report, University of Texas, Austin, 2004.
- [109] D. Montgomery and J. Terrell. *Some useful information for the design of aircore solenoids*. Technical report, MIT, 1961.
- [110] *PulseBlasterUSB Portable*. <https://www.spincore.com/products/PulseBlasterUSB>. Accessed: 2023-02-28.
- [111] *PICAXE Microcontrollers*. <https://picaxe.com/>. Accessed: 2023-03-02.
- [112] D. McCarron, S. King, and S. Cornish. *Modulation transfer spectroscopy in atomic rubidium*. Meas. Sci. Technol., **19**(10):105601, 2008.
- [113] P. Cheiney, L. Fouché, S. Templier, F. Napolitano, B. Battelier, P. Bouyer, and B. Barrett. *Navigation-compatible hybrid quantum accelerometer using a Kalman filter*. Phys. Rev. Appl., **10**(3):034030, 2018.

- 
- [114] L. Zhu, Y. Lien, A. Hinton, A. Niggebaum, C. Rammeloo, K. Bongs, and M. Holynski. *Application of optical single-sideband laser in Raman atom interferometry*. Opt. Express., **26**(6):6542–6553, 2018.
  - [115] C. Rammeloo, L. Zhu, Y. Lien, K. Bongs, and M. Holynski. *Performance of an optical single-sideband laser system for atom interferometry*. J. Opt. Soc. Am. B, **37**(5):1485–1493, 2020.
  - [116] G. Wang, Y. Wang, K. Ying, H. Zhang, X. Zhang, Q. Li, X. Li, E. Wang, X. Yu, A. Jia, et al. *Robust single-sideband-modulated Raman light generation for atom interferometry by FBG-based optical rectangular filtration*. Opt. Express, **30**(16):28658–28667, 2022.
  - [117] F. Theron, O. Carraz, G. Renon, N. Zahzam, Y. Bidel, M. Cadoret, and A. Bresson. *Narrow linewidth single laser source system for onboard atom interferometry*. Appl. Phys. B, **118**:1–5, 2015.
  - [118] C. Macrae, K. Bongs, and M. Holynski. *Optical frequency generation using fiber Bragg grating filters for applications in portable quantum sensing*. Opt. Lett., **46**(6):1257–1260, 2021.
  - [119] A. Othonos, K. Kalli, D. Pureur, and A. Mugnier. *Fibre Bragg Gratings*. Springer, 2006.
  - [120] A. Othonos. *Fiber Bragg Gratings*. Rev. Sci. Instrum., **68**(12):4309–4341, 1997.
  - [121] *TeraXion Fiber Bragg Gratings*. <https://www.teraxion.com/en/company/fiberbragggrating/>. Accessed: 2023-03-01.
  - [122] A. Peters, K. Chung, and S. Chu. *High-precision gravity measurements using atom interferometry*. Metrologia, **38**(1):25, 2001.
  - [123] A. Gauguier, T. Mehlstäubler, T. Lévêque, J. Le Gouët, W. Chaibi, B. Canuel, A. Clairon, F. Dos Santos, and A. Landragin. *Off-resonant Raman transition impact in an atom interferometer*. Phys. Rev. A, **78**(4):043615, 2008.
  - [124] Shau-Yu Lan, Pei-Chen Kuan, Brian Estey, Philipp Haslinger, and Holger Müller. *Influence of the Coriolis force in atom interferometry*. Physical Review Letters, **108**(9):090402, 2012.
  - [125] I. Perrin, J. Bernard, Y. Bidel, A. Bonnin, N. Zahzam, C. Blanchard, A. Bresson, and M. Cadoret. *Zero-velocity atom interferometry using a retroreflected frequency-chirped laser*. Phys. Rev. A, **100**(5):053618, 2019.